Characteristic information required for human motor control: Computational aspects and neural mechanisms

A DISSERTATION
SUBMITTED TO THE FACULTY OF THE GRADUATE SCHOOL
OF THE UNIVERSITY OF MINNESOTA
BY

Vassilios N. Christopoulos

IN PARTIAL FULFILLMENT OF THE REQUIREMENTS
FOR THE DEGREE OF
DOCTOR OF PHILOSOPHY

Paul R. Schrater & Apostolos P. Georgopoulos, Co-advisors

July, 2010

Acknowledgements

It is a pleasure to thank those who made this thesis possible. First, I would like to express my deep and sincere gratitude to my advisors Professor Paul R. Schrater and Prof. Apostolos P. Georgopoulos for their mentorship, support, encouragement and invaluable guidance throughout the course of this work. I would like also to thank Prof. Bagrat Amirikian for his helpful suggestions and the many insightful discussions. My thanks also to Prof. Matt Chafee, Prof. Victoria Interrante and Prof. Maria Gini for their willingness to serve on my thesis committee. Also, I am grateful to Prof. Art Leuthold for the inexhaustible assistance with the MEG study and Joshua Lynch for his valuable support in programming and processing of the neural recordings. I would especially like to thank David Rubins for his valuable suggestions of the manuscript.

My sincere appreciation to my officemates Aurelio Alonso, Roger Dumas, Nima Khoshnoodi, Elissaios Karageorgiou and Heng-Ru May Tan for all the cooperation. I owe a lot to my friends, Alexis, Andreas, Artemis, Christos, Dimitris, George, Giannis ($\times 2$), Ioanna, Kostas, Nikos, Tasos, Thanasis, Thimios, Vassilis ($\times 4$) (and others, who I am surely forgetting here) who were very supportive through the often insane times of my PhD.

I am immensely grateful to Sofia for her continued encouragement and patience during the period that I was writing this thesis. She helped me maintain my sanity with the ups and downs on my life as a graduate student.

Finally, I must acknowledge my parents, my sister, my brother-in-law and my nephews for supporting me all these years in countless ways, even though they live so far away.

Abstract

Motor behavior involves creating and executing appropriate action plans based on goals and relevant information. This information characterizes the state of environment, the task and the state of actions performed. The perceptual system gathers this information from different sources: touch, vision, audition, scent and taste. Despite the richness of environment and the sophistication of our sensory system, it is not possible to extract a complete and accurate representation of the required states for motor behavior because of noise and ambiguity. Consequently, people effectively have "limited information" and therefore may not be certain about the outcomes of specific actions. For motor behavior to be robust to uncertainty, the brain needs to represent both relevant states and their uncertainties, and it needs to build compensation for uncertainty into its motor strategy. Generating motor behavior requires the brain to convert goals and information into action sequences, and the flexibility of human motor behavior suggests that brain implements a complex control model. The primary goal of this work is to improve the characterization of this control model by studying motor compensation for uncertainty and determining the neural mechanisms underlying information processing and the control model.

Part of this thesis focuses on studying human compensation strategies in natural tasks like grasping. We experimentally tested the hypothesis that people compensate for object position uncertainty by adopting strategies that minimize the impact of uncertainty in grasp success. As we hypothesized, we found that people compensate for object position uncertainty by approaching the object along the direction of maximal position uncertainty. Additionally, we modeled the grasping task within the optimal control framework and found that human strategies share many characteristics with optimal strategies for grasping objects with position uncertainty.

We are also interested to understand how the brain encodes and processes information relevant to movements. To accomplish this, we studied the spatial and temporal interactions of cortical regions underlying continuous and sequential movements using magnetoencephalography (MEG). Particularly, we took data from a previous study, in which subjects continuously copied a pentagon shape for 45 s using an XY joystick. Using Box-Jenkins time series analysis techniques, we found that neural interactions and variability of movement direction are integrated in a feedforward-feedback scheme. MEG sensors related to feedforward scheme were distributed around the left motor cortex and the cerebellum, whereas sensors related to feedback scheme had a strong focus around the parietal and the temporal cortices.

Contents

List of Tables

List of Figures

Chapter 1

Introduction

1.1 Acting in dynamic environments

We coordinate our bodies with the external environment in robust and highly adaptive ways to solve complex problems everyday. While driving we follow traffic lines, maintain a safe distance from the car in front of us, avoid potential obstacles, accelerate to pass other cars, decelerate to exit highways, signal to change traffic lines and obey the traffic laws. In sports games, like basketball, skilled players are able to dribble without watching the ball, while also localizing the positions of other players and looking for opportunities to score. In tennis, professional players are able to estimate the height and the trajectory of a ball traveling at speeds around 100 mph. These impressive capabilities suggest that people are quite adept at extracting information from the environment, allowing them to adapt their behavior in real-time and to rapidly learn to perform new tasks based on previous knowledge and current information.

If we were able to track a series of N shots in a tennis game, we would notice that none of them are exactly the same, due to the variability of the characteristics of ball trajectories (i.e., speed, height, spin) [131]. However, skilled players use motor skills developed through experience and make motor decisions based on the current ball trajectory [159]. Given that no two consecutive shots are the same, tennis players cannot perform the same movement that they executed earlier. Instead, they must use previous knowledge and current information to make a decision about how

to hit the ball. To accomplish this, the sensory system should actively seek information to estimate the ball trajectory. However, despite the sophistication of our sensory system, it is not possible to extract complete and accurate information from the environment because of noise and ambiguity. Additionally, in tasks like sports game and driving, people have limited time to collect information. Consequently, they effectively have "limited information" and hence may not be certain about the outcomes of their actions. To deal with limited information, the sensorimotor system should incorporate uncertainty into motor decisions to improve task performance.

1.2 Optimal control framework for modeling human behavior in complex visuomotor tasks

How people plan, execute and correct actions in stochastic and dynamic environments has been extensively studied over the last 50 years within the optimal control framework [44, 45, 142]. Optimal control theory was developed in 1950's by the Russian mathematician Lev Semenovich Pontryagin (Pontryagin's minimum principle) and the American mathematician Richard Bellman and his colleagues (Hamilton-Jacobi-Bellman equation, HJB). The Pontryagin's minimum principle, which is consider a necessary condition for the solution of an optimal control problem, is used to find the best actions for taking a system from one state to another, subject to constraints of the states and the actions [40]. On the other hand, the solution of HJB equation, which is consider the sufficient condition for the solution of an optimal control problem, provides the optimal cost-to-go for a system in a current state with a given cost function [125, 142].

The ultimate goal of the optimal control theory is to identify policies for selecting a sequence of actions that best achieve cumulative reward in an uncertain and partially observed environment. In an optimal control model, an agent (e.g., a human or robot) interacts with its environment by gathering information and performing actions. These actions change the state of the world in some manner. Additionally, the agent receives a reward after performing an action in a given state. Let's consider the complex task of navigating a helicopter to a target location, while avoiding obstacles in a dynamic and partially observed environment, Fig. 1.1. If the pilot flies the helicopter too fast,

the chance of colliding with an obstacle is high. On the other hand, if he flies the helicopter too slowly, he may never reach the target location. Therefore, the optimal policy should maximize the chances of completing the mission and provide robustness against failure. Action goals are modeled using a reward function $g(x, \alpha, x', \theta)$ that quantifies the expected reward when state x' is reached after taking an action α at state x. The actions available to the agent are the set of legal moves (e.g., turn left, turn right, up, down). Actions stochastically affect the intrinsic world dynamics though a transition function $T = Pr(x', \theta'|x, \theta, \alpha)$, which defines the conditional probability of going to state x' by taking action α at state x. The helicopter is equipped with sensors (e.g., camera, IMU) to collect information from the environment. However, this information is delayed in time and corrupted by noise. Noisy and ambiguous observations are model by $O = Pr(o|x', \theta', \alpha)$. This conditional probability defines the probability of making an observation o when states x' and θ' are reached after performing an action α. Because the environment is partially observed and uncertain, the pilot does not know the exact state of the environment. Therefore, the pilot must maintain a probability distribution on state x and θ - known as belief state - given the observations at hand. For example, after an observation o, the belief $b_t = Pr(x, \theta|\{o_1, o_2, \times, o_n\})$ at a time t is updated using Bayes's rule, using the previous beliefs, the transition function and the observations. Based on the updated beliefs, the ultimate goal of the pilot is to learn a policy π that maximizes the cumulative discount reward for all belief states. The policy π is a function that encodes what (possibly stochastic) action to take in each belief state (i.e., $\pi(b) = \alpha$) and the optimal policy can be computed using the Bellman optimality equation Eq. (1.1).

$$V_x^*(b) = \arg\max_{\alpha} \sum_{x'} Pr(x'|x, b, a) \left(g\left(x, \alpha, x'\right) + \gamma V_x^*(b'_\alpha) \right) \tag{1.1}$$

where b is the current belief state in θ and b' is the predicted belief state that is expected to occur from receiving future observations while following the optimal policy. The optimal policy can be written in information state formulation - in essence the observation to belief mapping and belief to action mapping are nested to form one observation to action mapping. This form of policy can be written as feedforward-feedback control scheme, where feedforward generates future beliefs and

feedback incorporates new observations into action selection.

The solution to many optimal control problems cannot be found analytically. Over the years, many techniques, such as dynamic programming, reinforcement learning, partially-observable Markov decision process (POMDP), Bayesian decision theory and stochastic optimal feedback control have been proposed to solve optimal control problems.

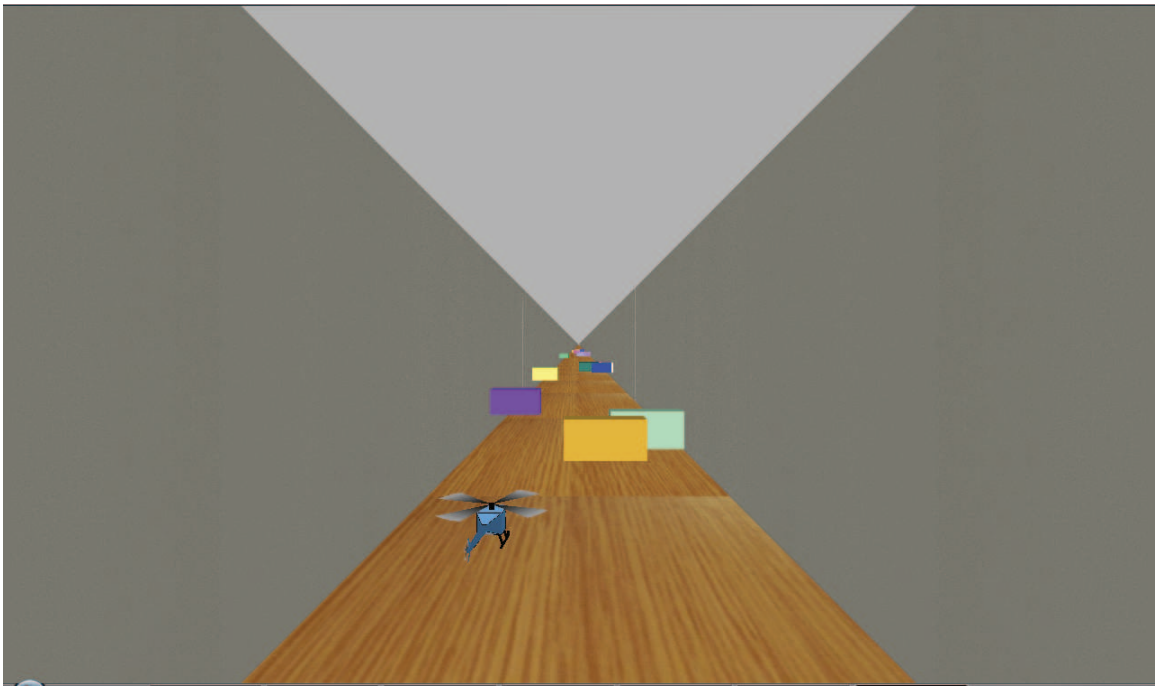

Figure 1.1: Illustration of the visuomotor task of learning to navigate a helicopter through obstacles in an uncertain and partially observed environment. This flight simulator was developed by Prof. B. Mettler at the University of Minnesota, to study human pilot control behavior in goal-directed flight tasks.

Optimal feedback control theory has been successfully applied to model a wide range of visuomotor tasks, such as reaching movements, [34, 50, 152], throwing balls to targets [51], grasping objects [63] and snowboarding/surfing [72] (for review see [49]). It consists mainly of two parts: a) an optimal estimator that predicts the current state using the available information from different sources, previous actions and knowledge about the system/sensory-motor delays/noise and others; b) an optimal controller that produces the actions that optimize some performance criteria given the current estimate of the state [48]. Let's consider again the helicopter navigation task. To find the best policy, the optimal control system requires an estimate of the belief state. Since the sensory

information from the environment is delayed in time and corrupted by noise, the optimal control system uses an internal model (i.e., estimator) to predict the next state. This prediction is integrated with the incoming sensory information to update the belief state. The best actions (i.e., motor commands) are then determined based on a control policy, which indicates what the controller should do given a certain goal and state estimate [51, 74, 132]. The architecture of the optimal feedback control framework for navigating a helicopter is presented in Fig. 1.2.

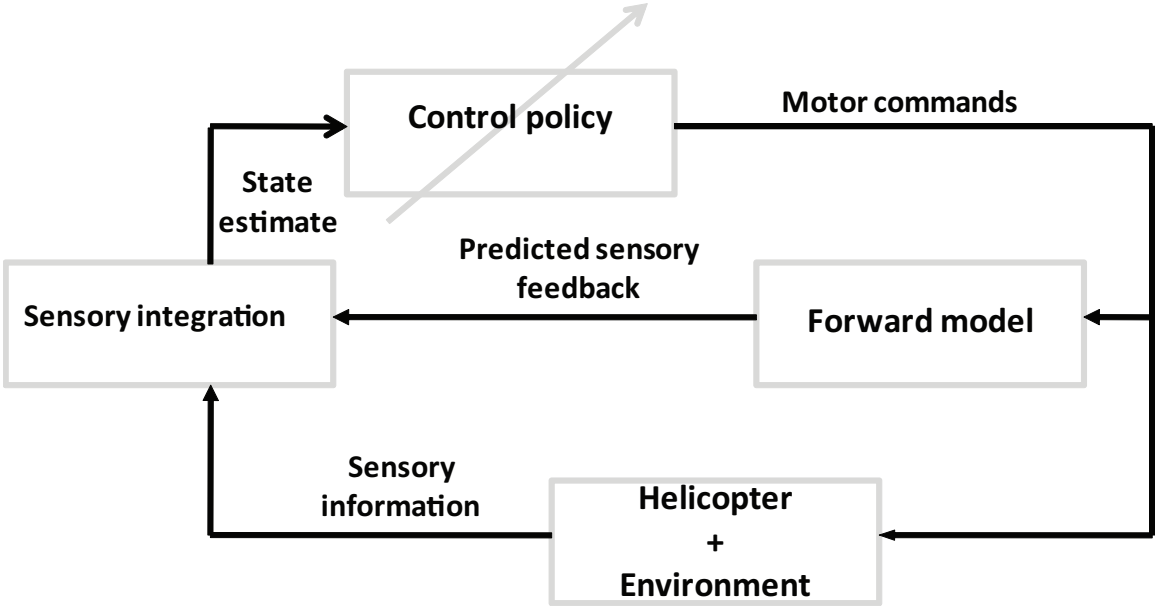

Figure 1.2: Architecture of the optimal feedback control framework for navigating a helicopter.

1.3 Feedforward and feedback motor control processes

People show a remarkable ability to perform on-line error corrections. To accomplish this, the brain may use sensory feedback (e.g., visual, proprioceptive) to modulate ongoing motor commands to compensate for deviations from the goal. The main argument against this theory is that brain is not able to process information quickly enough to make use of the sensory feedback information in real-time [107]. This hypothesis is supported also by behavioral studies, which showed that the minimum time delay needed for visual or proprioceptive sensory information to influence an ongoing movement is 80-100 ms [89, 107, 166]. Therefore, the processing of sensory information

is slower than hand motion in fast reaching movements and as a results the hand position will have changed by the time the sensory feedback is ready to influence it [89, 166].

According to these studies, sensory feedback information cannot be used to control hand trajectories. However, there is evidence to suggest that the brain uses internal models - known as feedforward (forward) models - to predict the consequences of ongoing actions. Particularly, forward models generate predictions of the next state based on the current state and ongoing actions. The main drawback of these models is that the predictions can be inaccurate due to lack of feedback. Therefore, a better solution is for a forward model to use a copy of motor commands to estimate the changes on the state that is expected to occur. The feedback information comes from the sensory system and provides a measure of these changes. Then, the prediction from the forward model is integrated with the sensory information from the feedback model to update our estimate about the next state. Therefore, our belief about the influence of actions on the state is a combination of what we "predict" and what we "observe" [97,133]. The sensorimotor system uses the updated prediction to compensate for potential deviations from the goal by modulating the motor commands.

There is a great deal of evidence that sensorimotor system implements this feedforward-feedback control scheme in a variety of visuomotor tasks, such as reaching and pointing to single targets [31, 43, 85, 107, 111, 112]. However, there are some movements that are so fast that there is no time for the sensory information to influence the ongoing actions [133]. A prominent example is the saccade eye movements - rapid intermittent eye movements - in which the eyes shift fixation from one point to another within 50-80 ms [90]. Due to the small time window, the visual feedback cannot influence the trajectory of the eye movement. In fact, this explains the "saccadic suppression" phenomenon [90], in which the visual system essentially shuts down for the duration of the saccade movement. Hence, the brain must guide the saccade movements in the absence of visual feedback. To accomplish this, a plausible explanation is that brain uses forward models to predict the next state of the eyes based on the current state and the ongoing current actions [38].

1.4 Feedforward-feedback control scheme and the brain

Another important role of the feedforward-feedback control is that it provides a computational framework for interpreting the functional role of different brain regions, Fig. 1.3. Particularly, studies in motor control suggest that the cerebellum is involved in predicting sensory outcomes of actions and correcting actions through internal feedback. The parietal cortex is associated with state estimation, in which the predicted sensory outcomes are integrated with the actual sensory information to update the belief on how ongoing actions affect the state of the body and the environment. The basal ganglia are associated with the expected reward of the predicted sensory states and the expected action costs. Finally, the primary and the premotor cortices are related to the implementation of the optimal plan by transforming the sensory predictions of the states into motor commands (for review see [133]).

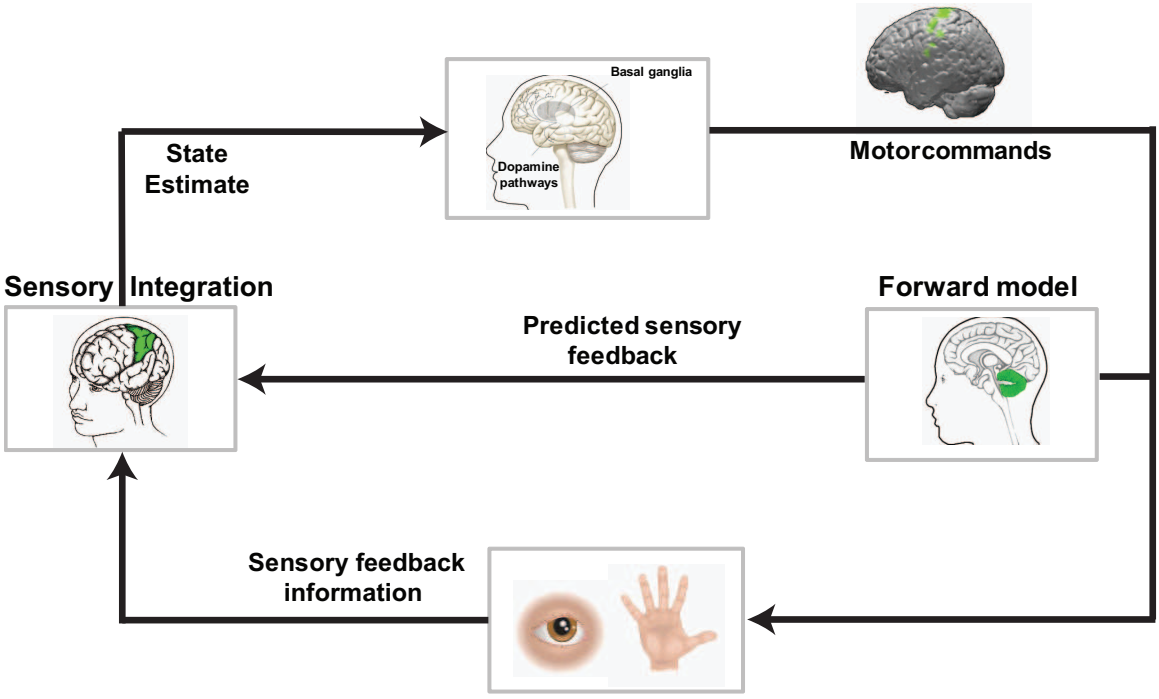

Figure 1.3: Schematic illustration of a simplified feedforward-feedback control scheme in the brain for planning, executing and correcting goal-directed movements.

1.4.1 Cerebellum

The cerebellum has an important role in regulating movements by building internal models to predict the consequences of ongoing actions. It is not easy to perform accurate predictions about the next state, because particular actions can affect the state differently. For instance, our limbs move differently when we hold objects of different weights. Therefore, the brain needs to adapt the internal models based on the sensory feedback information to maintain the accuracy of the predictions. The cerebellum appears to have an significant role of this process [133].

This hypothesis is supported by studies in patients with cerebellar damage, who encounter significant difficulties in learning new tools and adapting their behavior to unpredictable changes [133]. For instance, patients with cerebellar damage may not be able to adapt goal-directed arm movements to unknown external force fields [113], to compensate for novel visual feedback through a mirror [91] or to adapt to a laterally displacing prism [93, 116].

1.4.2 Parietal cortex

The role of the parietal cortex appears to be to integrate the predicted proprioceptive and visual outcomes with sensory information from different modalities to update the predictions about the consequences of motor commands to the state (for review see [29]). Studies in patients with damage in parietal cortex support the hypothesis that the parietal cortex is involved in estimating the state of the system (e.g., hand or limb position) and the environment. Grea and his colleagues studied the role of posterior parietal cortex (PPC) in on-line movement control [67]. They conducted an experiment, in which a patient with bilateral PPC lesion was instructed to reach and grasp a cylinder, which quickly and unexpectedly jumped to different locations on certain trials. They found that the patient did not have any problem reaching and grasping the stationary cylinder, and exhibited the same kinematics with the healthy subjects. However, when she experienced unpredictable changes in cylinder position, she continued to reach toward the original position of the cylinder. Therefore, the researchers concluded that patients with PPC damage are able to plan movements accurately, predicting the position of the target (forward model). However, the feedback sensory information (i.e., cylinder moving to a new location) is not integrated with the prior estimation of the cylinder

position to update the belief of the subject about the new state of the limb and the environment.

Another study explored the role of PPC in visually directed reaching tasks using transcranial magnetic stimulator (TMS) [106]. Similar to the previous task, healthy subjects reached toward a target that jumped unpredictably to new positions. A single pulse of TMS was applied over the PPC just after the hand movement onset. The results showed that most of the subjects failed to correct their plan movements in response to the new target location. However, the disruption of the PPC did not affect the accuracy of movements for a stationary target position.

1.4.3 Basal ganglia

The basal ganglia consist of the striatum - divided by a white matter tract (named "internal capsule") into two sectors named the "caudate" and "putamen" - the internal (medial) and external (lateral) segments of the globus pallidues, the subthalamus, the ventral tegmental area (VTA) and the substantia nigra pars compacta (SNc) and pars reticulata (SNr) [103]. They have an important role in optimal control, because they are involved in forming the expected rewards of the predicted sensory states and the expected costs of the motor commands [133].

Dopamine neurons in VTA and SNc have long been associated with rewarding behavior. They are activated by positive rewards such as food and liquid and by conditioned stimuli predicting such rewards [158, 171]. Additionally, drugs such as cocaine and amphetamine exert their pleasurable sensations by prolonging the effects of dopamine on target neurons, and dopamine neurons are among the best targets for electrical self-stimulation [136, 172]. Moreover, neurophysiological studies have found that direct stimulation of midbrain dopaminergic areas or injection of dopamine agonists into the neostriatum can produce responses similar to those established by natural rewards such as food and liquid [135]. On the other hand, the rewarding effects of food and liquid can be blocked or attenuated by dopamine antagonists [137,138]. Considering these findings, the dopamine neurons in VTA and SNc are plausible "candidates" for encoding expected reward in goal-directed movements.

Moreover, the basal ganglia may be involved in forming the expected costs of motor commands in goal-directed movements. A recent study with Parkinson's disease (PD) patients suggest that

bradykinesia (slowness of movements), which is one of the symptoms of PD, may be related to an abnormally high cost attributed to motor commands [124]. That is, PD patients may be reluctant to move quickly because of a shift in the cost/benefit ratio of the energy expenditure needed to move at normal speed. In addition to PD patients, most patients with degenerative diseases or damage to the basal ganglia have shaky, slow and tiny handwriting (micrographia), which may indicate abnormal high costs associated with the motor commands related to handwriting [133]. Although these findings support the hypothesis that the basal ganglia are involved in estimating the expected motor command costs, there is still an ongoing debate about the extent of their involvement (for review see [133]).

1.4.4 Primary and premotor cortex

The primary motor cortex - known also as the M1 area - is located in the posterior portion of the frontal lobe. It works in association with the premotor cortex to implement the optimal control policy by transforming beliefs about state of the body and the environment into motor commands based on the task goal.

1.5 Neural mechanisms underlying motor control

To gain a better understanding of the neural mechanisms underlying planning and control of movements, we need to understand the functional properties of the areas of interest, their connectivity and the spatial and temporal patterns of activity among them. Functional neuroimaging techniques, such as functional Magnetic Resonance Imaging (fMRI), Position Emission Tomography (PET), electroencephalography (EEG) and magnetoencephalography (MEG), provide the technology to study the spatial and temporal characteristics of the dynamic functional networks established in the brain, while subjects perform a variety of motor and cognitive tasks (for review see [160]). Among these techniques EEG and MEG are considered the most appropriate for studying neural mechanisms underlying voluntary movements, mainly because of their high temporal resolution. EEG and MEG are able to follow changes in neural synaptic activity on a millisecond time scale. In contrast, PET and fMRI are limited in temporal resolution to time scale on the order of a few seconds,

because they measure brain activity indirectly; fMRI measures variations in the Blood Oxygenation Level Dependent (BOLD) signal over time and PET measures flow of blood to different areas of the brain.

EEG and MEG recordings of brain activity in voluntary and self-paced movement tasks reveal a complex spatiotemporal pattern of activity across distinct cortical regions [33]. For instance, slow magnetic fields, which are observed about 1 s prior to voluntary movements, are typically widely distributed over the scalp, even for isolated movements of individual digits; it is thought that they arise from bilateral regions of the sensorimotor cortex [32]. Other EEG and MEG studies have explored the spatial and temporal cortical interactions associated with more complex voluntary tasks, such as reaching targets [18], sequences of bimanual movements [58] and copying geometrical figures continuously and without visual feedback [10].

Despite the significant knowledge that we have acquired from these studies about the spatiotemporal interactions of brain regions in motor control tasks, little is known about how these interactions are associated with the behavioral parameters of these tasks. We studied the spatial and temporal interactions of distinct brain regions underlying continuous and sequential movements and the association of them with movement parameters. We used data from a previous experiment, in which subjects copied a pentagon shape continuously for $\sim$ 45 s using an XY joystick, while neuromagnetic fluxes were recorded from them using a whole-head MEG device [10]. We found that neural interactions and the variability of movement direction are integrated in a feedforward-feedback control scheme. That is, we identified MEG sensors interactions around the motor cortex area and the cerebellum that precede (forward) changes in movement direction. Additionally, we found MEG sensors interactions in the parietal cortex area that follow (feedback) changes in movement direction.

1.6 Uncertainty compensation strategies

These findings suggest that motor behavior involves the cooperation and interaction of distinct brain regions. However, for motor behavior to be robust to uncertainty, the brain needs to represent not

only the state and the consequences of actions, but also their uncertainties, and to build compensation for this uncertainty into its motor strategy. To correctly manage uncertainty, the perceptual-motor control system should either actively seek sensory information to minimize the uncertainty or compensate for uncertainty when further reduction is not possible, instead of passively gather information from the environment. Generally, there are three distinct strategies to act in uncertain and dynamic environments: 1) perform actions robust to uncertainty, 2) delay actions and gather more information and 3) incorporate knowledge of the uncertainty when further reduction is not possible.

1.6.1 Robust uncertainty compensation

Some strategies provide more robustness against uncertainty than others. For instance, if we are uncertain about the position of an object that we want to grasp, we simply open our hand wider [55] and move more slowly (speed/accuracy trade-off) [128] to assure that our fingers will not collide with or miss the object . Let's consider a scenario, in which we attempt to grasp a glass of water, surrounded by other obstacles, in the center of a dining table with poor illumination. Because of these conditions, the sensory information about the glass position is poor. To avoid experiencing social disaster by splashing water over our guests, we have to adopt movement strategies that provide *robustness* against failure by compensating for the consequences of uncertainty through increased caution; taking safer paths [129], reducing speed [104], opening the fingers wider [13, 55, 102].

1.6.2 Collect more information before making a decision

People may delay their decision until more information can be gathered. Let's consider the task, in which a basketball player is trying either to score or pass the ball, while avoiding his opponents. To accomplish this task, the player may wait longer to make a decision in order to collect more information about the position of his teammates and opponents. However, the longer he waits to make a decision, the lower his chance of scoring becomes. A recent study addressed the question of how brain trade-offs between waiting for gathering more information and making a decision in a time-limited reaching task [130]. The results showed that people are able to predict the rate of

information and optimally balance the trade-off between spending time to gather information to reduce uncertainty and leaving enough time to perform the task.

Additionally, people can actively seek for perceptual information to reduce uncertainty. For instance, consider the scenario that you are gambling in a casino playing one-armed bandit. You have the option to select one of the several N one-armed bandit machines that are available at the casino. Each slot machine provides a reward drawn from a specific distribution associated with the specific slot machine. Your ultimate goal is to maximize the total reward earned through a sequence of games. Initially, you do not have any information about the expected reward associated with each slot machine. For that reason, at each trial you are faced with the exploration-exploitation dilemma. That is, at each trial you will be able to "exploit" the slot machine that you expect to have the highest payoff or "explore" other slot machines to gather more information about their expected reward [5]. Note that this idea might be instantiated into the control of eye movements, which are considered an important process of the brain to actively gather information from the environment related to tasks [30, 62].

1.6.3 Incorporate knowledge of uncertainty

Usually people have limited time to collect information before making a decision. For instance, a tennis player has a brief window in time to decide how to hit the ball. Waiting for a long time before making a decision can reduce the uncertainty about the ball position, but it increases the likelihood of missing the ball. Therefore, the tennis player should act based on the current information and the statistics of the ball position uncertainty to increase the chance of hitting the ball.

Previous studies have shown that people maintain and update estimates about uncertainty and use this information to improve task performance and economic gain [11, 70, 77, 81, 97, 149]. In the majority of these studies, tasks are carefully designed so that there is always a single well-defined goal and a best action strategy. However, these tasks do not explain many of the characteristics of natural everyday tasks. Today, little is known about how people compensate for uncertainty in natural tasks, mainly because it is hard to make normative predictions. Part of this thesis focuses on studying aspects of human compensation strategies in natural tasks, using grasping as a paradigm.

We found that people take into account the statistics of the environment and compensate for object position uncertainty by aligning the approach direction of their hand with the direction of maximal position uncertainty [168].

1.7 Thesis organization

The thesis is organized as follows:

Chapter 2 introduces a novel metric to evaluate grasp plans, in terms of the probability that a trajectory will result in object-finger contact that permit forces capable of stably lifting the objects (termed force-closure) [167]. We show how to incorporate shape and contact location uncertainty into grasp stability analysis and how to use this grasp metric to optimize contact locations in the face of shape uncertainty. We extend this metric to evaluate grasp plans for another type of uncertainty (position uncertainty) in chapter 3.

Chapter 3 presents a study of human compensation strategies for grasping objects with position uncertainty. We experimentally test the hypothesis that people compensate for object position uncertainty by adopting strategies that increase the chance of producing force-closure grasping at first contact without requiring post-contact adjustments. In accord with the hypothesis, we found that people compensate for object position uncertainty by opening their fingers wider and approaching the object along the direction of maximal position uncertainty. The novelty of this study is the normative evaluation of human grasping performance based on the probability of achieving force-closure grasping at first contact. We found that compensation strategies result in higher probability of achieving force-closure grasping without requiring post-contact adjustments than non-compensation strategies.

Chapter 4 extends the optimal feedback control theory to model the grasping task. We model the human hand as a 2D, 1-link planar device and build a mix of task-dependent performance criteria that combine accuracy and energetic efficiency. We ran a series of simulations and found that many characteristics of human behavior in grasping objects with position uncertainty can be interpreted within the optimal feedback control framework. That is, the optimal controller compensates for object position uncertainty by opening the gripper wider and aligning the approach direction of the

gripper with the direction of maximal position uncertainty, as long as the cost of compensation is not too expensive.

To understand how the brain encodes information relevant to control, Chapter 5 examines the spatiotemporal neural interactions underlying the continuous and sequential movements used to copy geometrical shapes. Subjects were trained to continuously copy a pentagonal shape using an XY device, while neuromagnetic fluxes were recorded using a whole-head MEG device. Copying a pentagon requires a sequence of movements to reproduce the edges (straight movements) and the corners (curved movements) of the object in a proper spatial relationship. We test the hypothesis that cortical interactions are associated with changes in movement direction. In accord with the hypothesis we found significant coupling between neural interactions and variability of movement direction. Particularly, neural interactions and variability in movement direction are integrated in a feedforward-feedback control scheme.

Finally, Chapter 6 summarizes the main findings of the thesis and discusses broader impact of the results.

Chapter 2

Grasping objects with shape and contact location uncertainty

2.1 Overview

This chapter addresses the problem of selecting contact locations for grasping objects in the presence of shape and contact location uncertainty. Focusing on two-dimensional planar objects and two finger grasps for simplicity, we present a principled approach for selecting contact points by analyzing the risk of force-closure failure. The key contribution of this paper is the development of a method that incorporates shape uncertainty into grasp stability analysis. We propose a grasp quality metric that can be used to identify stable contact regions in the face of shape and contact location uncertainty. The proposed method successfully distinguishes grasps that are equivalent without uncertainty, and we illustrate the properties of this technique with simulation experiments in two classes of objects.

2.2 Introduction

One of the most important problems in grasping and manipulation is the selection of contact points to grasp an object. Grasping involves fixturing the object relative to a gripper, and forms a necessary condition for object manipulation without changing object or finger contacts. Grasp planning

requires a method of evaluating the potential quality of contact points for fixturing the object. Solutions to this problem involve specifying an appropriate grasp quality measure and an algorithm that optimizes this measure to formulate a reaching plan. A successful reaching plan directs the fingers to contact points on the object that are both high quality and achievable by the particular robotic gripper.

Consider the challenge posed by the following scenario: An agent (human or a robotic system) equipped with a hand/robotic gripper and a vision system operates in dynamic environments with the goal of grasping visually sensed but otherwise unknown objects. To select stable contacts, the agent must have access to the 3-dimensional geometry of the object. However, objects for which many surface locations are visually foreshortened or occluded in the image produce significant errors in 3-dimensional reconstruction. How to perform grasp analysis under these conditions is an open question. Since grasp quality will depend on errors in 3-dimensional reconstruction, the effects of shape uncertainty on grasp stability should be included in identifying stable contact locations. The main contribution of this paper is to show how to incorporate shape uncertainty into grasp stability analysis, and to provide a novel grasp quality metric that can be used to optimize contact selection in the face of shape uncertainty.

Studies on grasp measures have led to a variety of theoretical proposals that revolve around notions of force or form closure. These measures take as input a model of object contours (2-dimensional) or object surface (3-dimensional), the number and the type of contacts (point/soft, with/without friction), and return a quality score for each set of possible contacts [2].

In this type of analysis, grasp contact with an object of known geometry is modeled as N point (or line) contacts, which are one of several types: frictionless, frictional, or soft point. The wrenches that end-effectors can exert at these contacts vary with type. For example, frictionless permits only forces along the direction of the normal vector, while frictional also permits forces along the direction of the tangential vector [2].

Force (form) closure occurs when the sum of the set of wrenches (vectors containing forces and moments) at frictional (frictionless) contact points can equilibrate an external wrench. A set of contact locations are considered viable for force-closure if any external wrench can be canceled by

a suitable scaling of the contact wrenches, and the number of contacts required for viability under various conditions to achieve force (form) closure are known [165].

One of the simplest kinds of grasp quality score is a force (form) closure score, a binary number that indicates whether a grasp at a set of contacts is viable [1]. With perfect sensing and positioning, this measure does not distinguish between viable points - in the extreme, all contact locations may be viable for force-closure (e.g. a sphere). Grasp quality metrics suffer from ambiguities of this kind, requiring planning algorithms to use other aspects of the grasp to select contact points (like reach path or wrench magnitude) from the viable set.

However, force-closure ambiguity is largely eliminated by contact perturbations introduced by shape and contact location uncertainty. If we do not incorporate uncertainty in grasp plans, we may generate grasp failures for plans that appear viable. This study proposes an approach for evaluating grasp quality in the presence of uncertainty. In particular, we show how to compute the probability of force-closure grasp, quantifying shape uncertainty using statistical shape analysis and introducing approach coordinates to handle variability in finger positioning and contact location.

2.3 Grasp selection as a constraint optimization problem

In previous studies one of the principle ideas is to treat grasp selection as a constraint optimization problem [155]. Based on this approach, a number of objective functions are used for maximizing a grasp quality measure subject to various constraints, including: aspects of grasp task (e.g., exerted forces), object geometry (e.g., shape, dimension) and/or hand (gripper) characteristics (e.g., degrees of freedom). Grasp quality approaches include force (form) closure [165], resistance to slipping [92, 105], the number of degrees of freedom in object-hand linkage [121] (the number of independent parameters that are needed to specify the position and the orientation of the grasped object with respect to the hand), and grasp isotropy. All of these measures depend on the type of contacts and object geometry, and hence will be affected by changes in either contact or geometry. In addition, none of these measures are designed to handle uncertainty - they assume that the grasping environment is deterministic. Although it is widely appreciated that uncertainty adversely affects grasping, previous work involving grasp planning with different kinds of uncertainty is limited.

A Bayesian approach for grasping an object with orientation uncertainty is presented in [99]. Assuming no information about initial object orientation, the goal of this approach is to move an object to a desired final state by a sequence of actions that minimizes expected cost, where cost is measured in terms of the type and number of required actions. Another approach for grasping an object with orientation uncertainty is presented in [139]. This method is based on estimating the space of grasping motions (i.e., squeeze-grasp, offset-grasp and push-grasp), that guarantee stable grasp of two dimensional planar objects with unknown pose using a parallel-jaw gripper. However, neither of these studies considers shape and contact location uncertainty, and both use frictionless point contacts (form-closure) constraints.

Several authors have looked at finger uncertainty in grasping. In [177], the finger uncertainty is analyzed using perturbation of object-finger locations with friction uncertainty. A new metric for measuring the sensitivity of grasp to contact uncertainty is presented in [65]. Approximating shape of a 2-dimensional planar object with a polygon, the goal of this study is to determine the maximum torque magnitude that the equilibrium grasp can resist. Based on this measure, the effect of positional error on the static equilibrium of the grasp could be determined.

Methods to make grasp plans robust to unknown object identity and friction errors introduced by visual sensing are presented in [3, 6, 83]. However, these methods do not model uncertainty nor do they consider its impact on grasp quality. We are aware of no previous work on the effects of shape uncertainty on grasp quality.

2.4 Shape uncertainty due to visual sensing

Shape uncertainty occurs whenever object geometry is known imprecisely due to imperfect sensing, such as object self-occlusion - we see only the front halves of objects - and perspective projection. We illustrate the origin of shape uncertainty due to perspective projection using an example from computer vision. Particularly, consider estimating the shape of the cellular phone in Fig. 2.1, using a model-based object segmentation algorithm and a pin-hole camera. The projected shape of the phone is geometrically distorted away from the model shape due to a different acquisition viewpoint [26]. However, there is an affine transformation that (approximately) relates the two shapes [150]

(described below). The problem is that errors in the match between object and template can be absorbed into the affine transformation that encodes object pose.

For systems that use flexible templates [4], shape and pose are jointly estimated so that errors in both matching and pose generates uncertainty about the shape of the phone [60]. For this case, the position of the camera with respect to the phone creates uncertainty about its geometric characteristics. The right panel of Fig. 2.1 shows a set of possible phone shapes, which have been generated by taking images under different viewpoints and applying affine transformation. Clearly, following the aforementioned procedure, it is not possible to know which of the estimated shapes correspond to the actual shape of the phone. Hence, we need to maintain the uncertainty about the estimated shape of the objects during grasp planning.

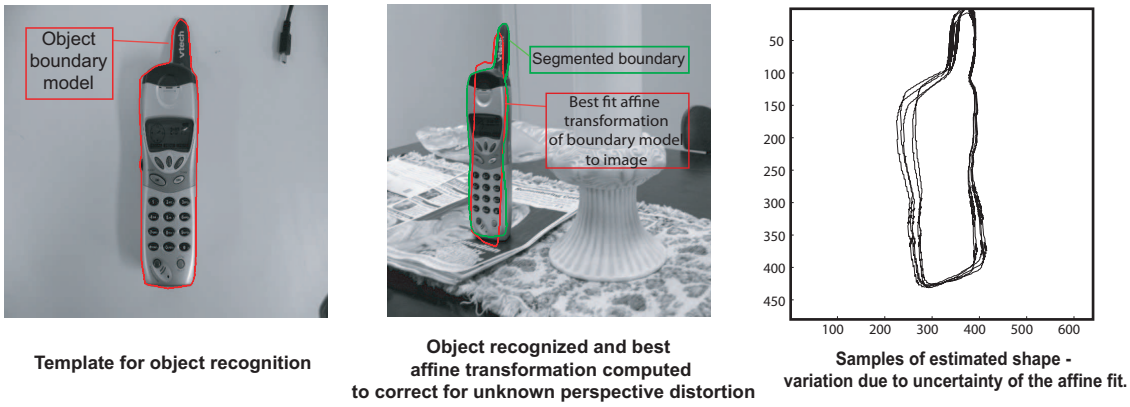

Figure 2.1: Illustration of the origins of shape uncertainty. Template matching used to recognize and localize a target object in a scene, in this case a phone. **Left**: Target object is specified and segmentation is used to create a contour template. **Center**: Recognition and template transformation are determined using SIFT keypoints-a set of reliable feature points determined on the target object and found in the scene image. An affine transformation is estimated (poorly) between the feature point locations on the target object and their locations in the scene. This transformation forms a simple (paraperspective) model [94] of the image deformation under perspective projection. The affine transformation can be inverted to view the detected object from the front. However, the transformation has errors in it that creates uncertainty in the understanding of the detected shape. **Right**: The error in shape understanding of the cellular phone can be visualized by propagating Monte Carlo samples of the feature point matching error to the affine transformation estimates, generating a set of affine transformation samples. The affine matrices can be inverted and applied to the segmented object boundary in the scene, approximately inverting the perspective distortion. The result of this procedure is a set of possible object shapes. Given this sensing method it is not possible to know which of these samples represents the actual shape.

2.5 Methods

In this section we provide the necessary background both on the statistical modeling of the shape and on necessary conditions for force-closure grasp. This theory will be used to develop a method for computing the quality of grasp plans.

2.5.1 Data preprocessing and object recognition

Assume that we have a set of two-dimensional planar objects resulting from image segmentation (e.g. bottles or keys) that belong to the same class but exhibit shape variation (or uncertainty), Fig. 2.2. Initially, we blur segmented images using binomial filters to remove small details and to smooth the outlines of the objects [140].

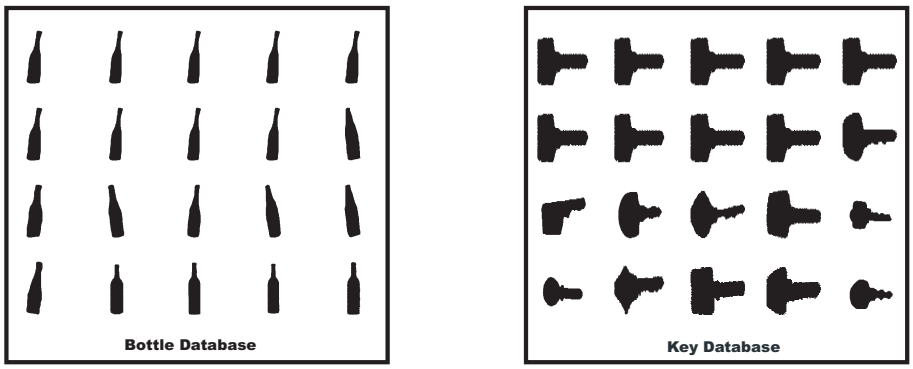

Figure 2.2: Databases of 20 bottles (left) and 20 keys (right) with shape variation used in this study to evaluate the proposed quality metric of grasping

To extract curves from segmented images, we extract a chain of points on the objects boundary and construct an arc-length parameter from the cumulative distance between points. Finally, the N points are interpolated using smoothing natural cubic splines (illustrated in Fig. 2.3) which can be converted to B-spline form via a linear transformation.

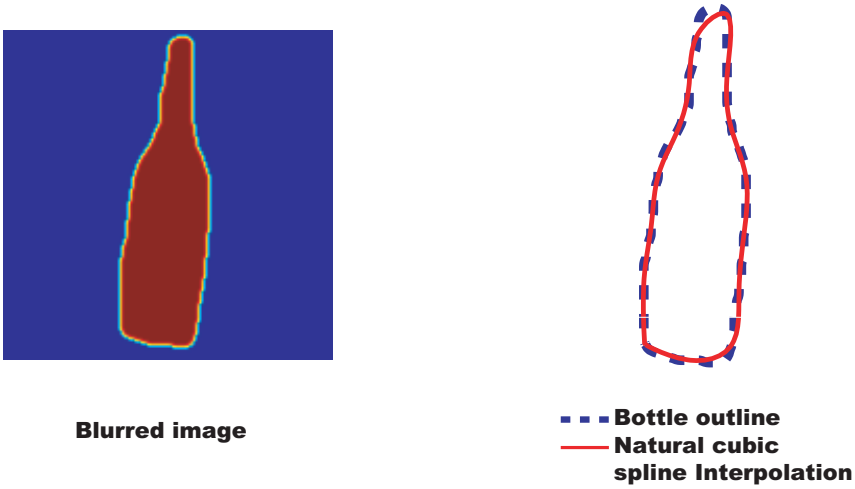

Figure 2.3: **Left**: Blurred image using binomial filter. **Right**: Extracted boundary of a typical sample from the bottle database using model-based object segmentation technique (blue discontinuous line) and natural cubic spline interpolation (red continuous line).

2.5.2 Shape description using splines

We restrict our attention to spline curve and surface representation due to their simplicity and the ease of specifying shape uncertainty in spline models. We assume that any differences between the actual object surface and the spline representation do not significantly affect the results of contact analysis. This is a reasonable assumption for soft-finger contacts with the object. For planar objects, a closed simply connected shape can be represented as a linear combination of B-splines defined on an arc-length parameter, Eq. (2.1)

$$[x(s)y(s)] = \sum_{i=0}^{n} B^i(s) \begin{bmatrix} \alpha_i^x \\ \alpha_i^y \end{bmatrix} = \begin{bmatrix} \vec{B}(s)^T & \vec{0}(s)^T \\ \vec{0}(s)^T & \vec{B}(s)^T \end{bmatrix} \vec{\alpha} = \mathbf{B}(s)\vec{\alpha} \tag{2.1}$$

where $B^i(s)$ are periodic cubic B-spline functions defined on a knot sequence on the arc-length parameter s, $[x(s)y(s)]$ are the Cartesian coordinates of the curve and $\vec{\alpha} = \left[\vec{\alpha}_x^T \vec{\alpha}_y^T\right]^T$ is a $2n \times 1$ vector of coefficients that uniquely specify the shape given the knot sequence. It is straightforward to induce a probability distribution on shapes, $P(\vec{\alpha})$. In general, this one will be a density conditioned

on the current image information.

The major advantage of using a basis function representation for shape is its low dimensional shape-space representations, which are linear in transformation parameters. In addition, basis functions provide simple ways of computing important curve properties like tangents and normals. In particular, the unnormalized tangent at each point s' is linear in the shape parameters and is given by Eq. (2.2).

$$[t_x(s), t_y(s)] = \mathbf{D}(s')\vec{\alpha} \tag{2.2}$$

where $\mathbf{D}(s) = \frac{d\mathbf{B}(s)}{ds}$. Given a counterclockwise parametrization of the curve, the unnormalized normal at each point s' is given by Eq. (2.3)

$$[n_x(s), n_y(s)] = \begin{bmatrix} 0 & -1 \\ 1 & 0 \end{bmatrix} \mathbf{D}(s')\vec{\alpha} = \mathbf{N}(s')\vec{\alpha} \tag{2.3}$$

As explained previously, a common source of shape uncertainty is the distortion due to camera calibration and/or image matching errors. These errors produce affine distortions of the object contours [4]. For example, the projected shape of a 3-dimensional planar curve can be represented in shape-space through Eq. (2.4).

$$\vec{\alpha} = W\vec{q} = \begin{bmatrix} \mathbf{1} & \mathbf{0} & \vec{\alpha}_0^x & \mathbf{0} & \mathbf{0} & \vec{\alpha}_0^y & \vec{\alpha}_0^z & \mathbf{0} \\ \mathbf{0} & \mathbf{1} & \mathbf{0} & \vec{\alpha}_0^y & \vec{\alpha}_0^x & \mathbf{0} & \mathbf{0} & \vec{\alpha}_0^z \end{bmatrix} \vec{q} \tag{2.4}$$

where $\vec{\alpha}_0^x, \vec{\alpha}_0^y, \vec{\alpha}_0^z$ are the 3-dimensional coordinates of the base shape of the curve. In this representation, the components of $\vec{q}$ represent translation, scaling and rotation of the base curve in 3-dimensional space, and W maps the effect of these changes on the projected contour. Note that a probability distribution on the reduced space $\vec{q}$, $P(\vec{q})$, induces distributions on the curve, $P(\vec{\alpha})$

tangents and normals through linear operators. We will take advantage of this in our formulation of the optimal grasping problem given shape uncertainty.

2.5.3 Finding grasp equilibrium

It is known that the force-closure grasp is a necessary condition for equilibrium [165]. Assume that we have two contact points A and B on the outline of a cylindrical object (left panel of Fig 2.4). These contact points permit force-closure grasp, since the segment AB is located inside the two fiction cones defined by the contact points A and B. Using Coulomb's law, force-closure occurs when the component of the contact forces at the points A and B in the direction of the surface normal (**n**) exceeds the coefficient of fiction (μ) times the tangential component (**t**). Geometrically, this relation produces friction cones, whose boundaries are determined by the vectors $\mathbf{n} - \mu\mathbf{t}^+$ and $\mathbf{n} - \mu\mathbf{t}^-$, where $\mathbf{t}^+ = \mathbf{t}$ and $\mathbf{t}^- = -\mathbf{t}$.

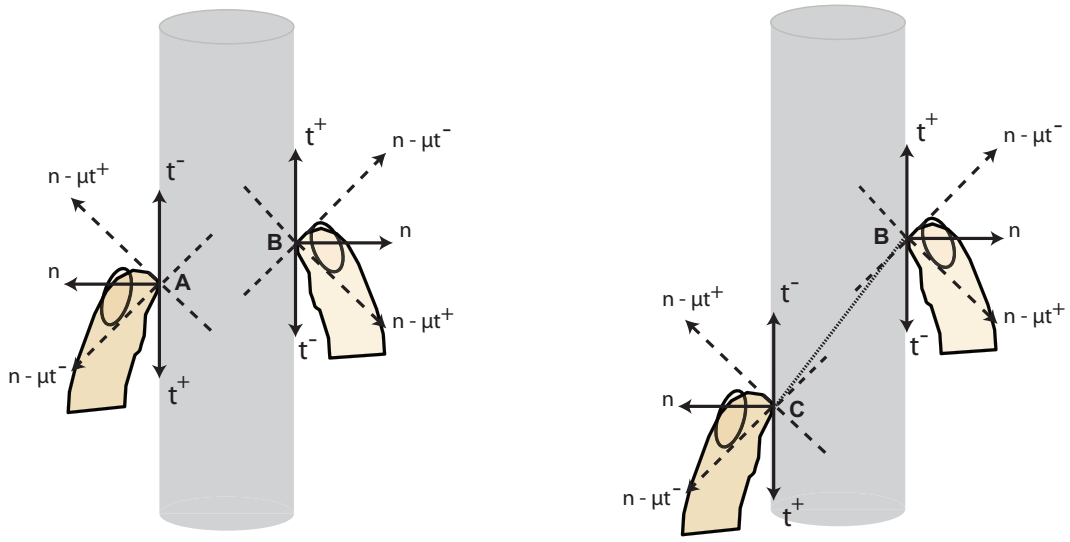

Figure 2.4: **Left**: The contact points A and B produce a planar force-closure grasp, because the segment AB is between the two friction cones defined at the contact points. **Right**: In contrary, the contact points B and C do not produce force-closure grasp, because the segment BC is outside of both friction cones defined at the contact points B and C.

Thus, testing for force-closure is equivalent to testing whether the segment AB is between the two friction cones. To illustrate, if the segment is out of one or both friction cones (e.g., right panel

of Fig 2.4), the two contact points do not construct a planar force-closure and the object cannot be grasped from these two points. In other words, if we define $\mathbf{D_{AB}}$ as the vector from contact point A to B, these two points permit force-closure grasp, if the inequalities in Eq. (2.5) hold.

$$\begin{aligned} (\mu \mathbf{n}_A + \mathbf{t}_A)\, \mathbf{D_{AB}} &\leq 0 \\ (\mu \mathbf{n}_A - \mathbf{t}_A)\, \mathbf{D_{AB}} &\leq 0 \\ -(\mu \mathbf{n}_B + \mathbf{t}_B)\, \mathbf{D_{AB}} &\leq 0 \\ -(\mu \mathbf{n}_B - \mathbf{t}_B)\, \mathbf{D_{AB}} &\leq 0 \end{aligned} \tag{2.5}$$

2.6 Determining feasible locations in planar objects

Assume that a planar object can be represented by N contact points following the procedure that we have described in section 2.5.2. The ultimate goal is to find a feasible set of contact locations to provide an input to reach planning using the inequalities of Eq. (2.5). However, object coordinates (even landmarks) are not stable from the hand's point-of-view in the presence of shape uncertainty and cannot be used directly for planning.

2.6.1 Approach space

To handle this problem, we obtain the feasibility of grasp plan, by computing the probability that the grasp plan will result in contact locations that form force-closure grasp of the object. To make this solution practical, we focus on the reaching movement near the object's boundary (*the approach*), where we assume finger trajectories can be approximated by line segments. Hence for two-finger planar grasps, the approach space requires 3 parameters per finger to specify the origins and directions of the line segments, Eq. (2.6).

$$\vec{l}_i(\lambda) = \vec{x}_{0,i} + \lambda \left[\cos(\theta_i) \sin(\theta_i)\right] = \vec{x}_{0,i} + \lambda \vec{u}(\theta_i) \tag{2.6}$$

where $\theta_i \, \varepsilon \, [0, 2\pi]$ is the direction of the finger i when grasping the object, $\vec{x}_{0,i}$ corresponds to the origin of the finger i and λ is the scale variable of the line segment. In this case, grasp plans with equivalent approaches are presented as points $\vec{g} = \{\vec{x}_{0,1}, \vec{x}_{0,2}, \theta_1, \theta_2\}$ in an approach space $\left(\Re^4, S^2\right)$. For every approach under consideration, we need to compute the probability of successful force-closure grasp. To simplify our analysis, we focus on grasp plans in which the fingers' directions intersect somewhere inside the boundary of the object $\vec{x}_0$, which is called the "approach center". Given an approach, we can compute the possible contact locations of an object with shape uncertainty without using world coordinates. In this way, the choice of approach can be made without exact determination of the contact location on the actual object.

Fig. 2.5 depicts an example of three objects that belong to the uncertainty set. Based on the approach, we can compute the contact locations (red dots) for any value of the uncertain shape parameters $\vec{q}$. Although the analysis is more complicated for extended fingers and non-linear paths, approach analysis can be performed in these cases as well.

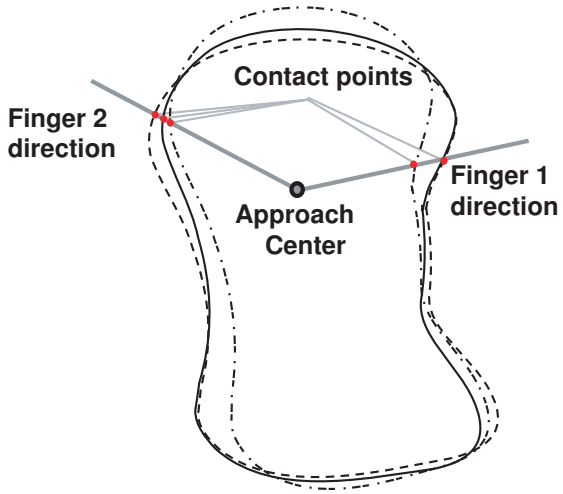

Figure 2.5: Computing contact locations in the approach space. Assuming that the direction of the fingers are intersected in the center of approach, the contacts (red dots) depend on the fingers' angular position and not on the shape's coordinates.

2.6.2 Feasibility analysis of planar objects with shape uncertainty

We decompose the problem of computing the probability of force-closure grasp into two parts. One part is to compute the probability across contact locations given a set of approach coordinates. The probability across contact points incorporates both shape uncertainty and noisy execution of the reach. The second part focuses on computing the probability that a grasp will result in force-closure for each set of contact locations.

For any pair of contact points $\{\vec{x}_{c1}, \vec{x}_{c2}\} = \{\mathbf{B}(s_1^*)\mathbf{W}\vec{q}, \mathbf{B}(s_2^*)\mathbf{W}\vec{q}\}$ obtained by following an approach $\vec{g}_e$, we define a feasibility indicator function $f = \mathbf{I}(\vec{q}, \vec{x}_{c1}, \vec{x}_{c2})$, where $\vec{q} = [q_1, q_2, \ldots, q_m]$ describes the parameters of the object outline. The indicator function returns 1 if the inequalities in Eq. (2.5) hold and 0 otherwise. Using this indicator function, the probability that an executed approach is feasible is given by Eq. (2.7).

$$P(f = 1|\vec{g}_e) = \int_{q_1}\int_{q_2}\ldots\int_{q_m} \mathbf{I}(\vec{q}, \vec{x}_{c1}, \vec{x}_{c2})\, P(\vec{q})\, d\vec{q} \tag{2.7}$$

For any particular shape, we can find the contact points of the executed approach $\vec{g}_e$ by computing the intersection of the finger's line segment paths with the boundary of the object. The computation of the first intersection with the control polygon of the shape's spline curve is simple. We refine this intersection to lie on the spline curve numerically (for 4^{th} order or less B-spline curves, we can find the contact points by solving the intersection of a line segment and a polynomial) resulting in locations on the curve $(s_1^*(\vec{g}_e, \vec{q}), s_2^*(\vec{g}_e, \vec{q}))$. The force-closure conditions are then straightforward to write explicitly in terms of the shape parameters. For instance, using Eqs. (2.2), (2.3), (2.4), we can rewrite the first inequality of Eq. (2.5) as follows:

$$\begin{aligned} \gamma_1 &= (\mu\mathbf{N}(s_1^*)\vec{\alpha} - \mathbf{D}(s_1^*)\vec{\alpha})^T (\mathbf{B}(s_2^*)\vec{\alpha} - \mathbf{B}(s_1^*)\vec{\alpha}) < 0 \Rightarrow \\ &= ((\mu\mathbf{N}(s_1^*) - \mathbf{D}(s_1^*))\mathbf{W}\vec{q})^T (\mathbf{B}(s_2^*) - \mathbf{B}(s_1^*))\mathbf{W}\vec{q} < 0 \end{aligned} \tag{2.8}$$

In the same way, γ_2, γ_3 and γ_4 can be obtained from the rest of the inequalities of Eq. (2.5), using

the terms of the shape parameters. If these inequalities hold, the executed approach $\vec{g}_e$ produces force-closure grasp. Overall, an indicator function that returns 1 when all four inequalities hold can be similarly computed for every $(\vec{g}_e, \vec{q})$ pair. The pseudo-code of the procedure for detecting contact locations that produce force-closure grasp is presented in Fig. 2.6.

For j = 1 to M sample approaches
  For i = 1 to N sample shapes
   sample shape:
   P($\vec{a}$) $\rightarrow \vec{a}_{ij}$
    intersect object:
    $s_1^* \leftarrow$ intersect ($\vec{x}_{0,1}$, θ_1, $\vec{a}_{ij}$)
    $s_2^* \leftarrow$ intersect ($\vec{x}_{0,2}$, θ_2, $\vec{a}_{ij}$)
     compute force-closure condition
     $\gamma_k^{ij}(s_1^*, s_2^*) < 0, \;\; k = 1, \cdots, 4$
  end sample shape
  compute quality metric
  $\mathbf{Q}_j = \sum_{i=1}^{Nsamples} H(\gamma_1^{ij})H(\gamma_2^{ij})H(\gamma_3^{ij})H(\gamma_4^{ij})P(\vec{a}_{ij})$
end approach

Figure 2.6: Pseudo-code of the procedure for identifying stable contact locations under shape uncertainty. The superscripts and subscripts i, j help convey that the stability measure and shape parameters vary within both loops. H(·) corresponds to the Heaviside step function

.

Finally, we also interested in including the effects of noisy execution of an approach by defining a conditional distribution of the executed approach $\vec{g}_e$, given the desirable approach $\vec{g}_{plan}$, $P(\vec{g}_e|\vec{g}_{plan})$. These effects should be taken into account in order to reduce the probability of grasp failure by reducing the feasibility of approaches that are sensitive to perturbations. The effect of noisy execution on the feasibility $\vec{g}_{plan}$ is given by Eq. (2.9).

$$P(f = 1|\vec{g}_{plan}) = \int_{\vec{g}_e} P(f = 1|\vec{g}_e)P(\vec{g}_e|\vec{g}_{plan})d\vec{g}_e \tag{2.9}$$

For low levels of noise, the effects of noisy execution, $P(\vec{g}_e|\vec{g}_{plan})$, can be approximated by a Gaussian distribution.

2.6.3 Computing probability of grasp stability via sampling

Contact locations can be selected by optimizing the grasp stability given by Eq. (2.9). However, straightforward optimization of the grasp stability measure is difficult due to integrals in Eqs. (2.7) and (2.9). For this reason, we have used Monte Carlo integration. Sampling shapes from $P(\vec{q})$ and plans from $P(\vec{g}_e|\vec{g}_{plan})$, we compute the feasibility of each sample pair and average. In this study, we focus on two special cases of approaching an object. First, the object is approached having both directions of the fingers intersect at a common point $\vec{x}_0$ (i.e., approach center), inside the object boundary. We assume that the fingers are moved by actuators with independent noise. The desirable approach $\vec{g}_{plan}$ is described by the $\{\phi_\alpha^*, \phi_\delta^*, \vec{x}_0\}$, where ϕ_α^* and ϕ_δ^* denote the desirable movement direction of the first and second finger, respectively. Let ϕ_α and ϕ_δ describe the actual finger's movement directions near the object boundary, then for each approach center, $\vec{x}_0$, the probability distribution for any grasp plan is given by Eq. (2.10).

$$P(\vec{g}_e|\vec{g}_{plan}) = P(\phi_\alpha|\phi_\alpha^*, \vec{x}_0)\, P(\phi_\delta|\phi_\delta^*, \vec{x}_0) \tag{2.10}$$

A second important case is when the two fingers motions are constrained, as in a two finger parallel gripper where the fingers always move parallel to each other in opposite directions driven by a single actuator. In this case the probability distribution of grasp plans has the form described in Eq. (2.11)

$$P(\vec{g}_e|\vec{g}_{plan}) = \delta(\phi_\delta - (\phi_\alpha + \pi))P(\phi_\alpha|\phi_\alpha^*, \vec{x}_0) \tag{2.11}$$

where $\delta(.)$ is the dirac delta function that enforces the constraint that the approach directions of the two fingers oppose each other.

2.7 Simulation results

In this section, we present and discuss the properties of grasp stability under uncertainty using two different object datasets from the Brown vision laboratory [101]. Each dataset contains 20 two-dimensional planar objects that belong to the same class but exhibit significant shape variation. The shape variation in this case is similar to the shape variation of objects due to visual sensing discussed in section 2.4. To model noise in approach execution, we use a zero mean Gaussian distribution for Eq. (2.10) with variance 0.05 rad, and assume that the friction coefficient is 1 (for simplicity reasons and it is in the range of typical values of soft finger contact).

2.7.1 Determine feasible locations in the bottle database

Two different ways for approaching a typical sample from the bottle database is shown in Fig. 2.7 left. Although a standard force-closure analysis does not distinguish them, case I is more desirable than case II in the presence of shape and contact location uncertainty, because there are more ways to generate feasible contact points. Thus, the probability measure is analogous to a motion perturbation analysis [177], since plans with the highest probability of feasibility are those that survive perturbations in finger locations. Note that the strong point of the proposed method is that it handles not only perturbations in finger locations but also shape perturbations.

The results of estimating Eq. (2.9) by sampling both approach directions and boundaries of bottles are shown in Fig. 2.9. To help visualize the results, the center of approach is fixed at several locations, chosen along the axis of the second moment of the boundary points (see Fig. 2.8), centered around the center of mass of the bottle dataset. The probability of a feasible grasp is displayed as a function of the first and second finger approach directions. The intersection of a set of finger directions with a typical sample of a bottle boundary is displayed next to the probability maps, sampled at 0.3 rad (i.e., $2\pi/0.3 \simeq 21$ contact points).

In Fig. 2.9 the red areas correspond to pairs of finger directions with high probability of producing force-closure grasp. In contrary, blue areas correspond to unreliable regions for grasping the bottles, since the probability to obtain force-closure grasp is very low. Hence, the probability to achieve a stable grasp is higher grasping the bottle around its "body" (red islands) than grasping it

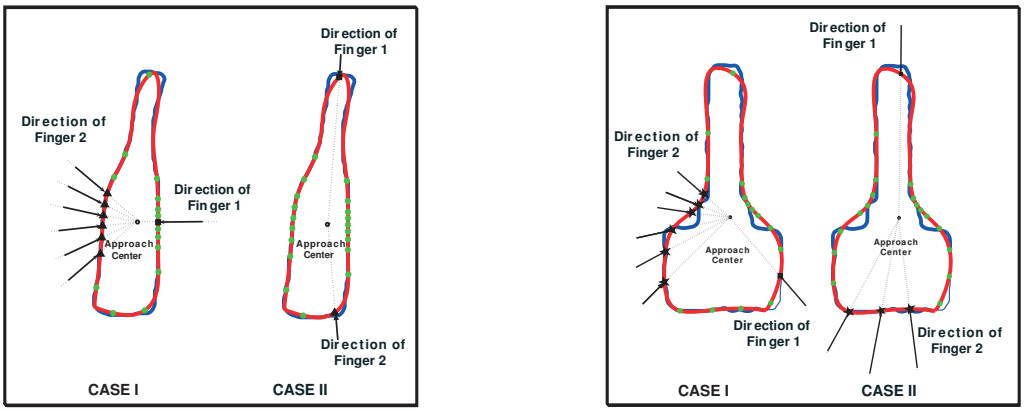

Figure 2.7: Two different ways for reaching a typical sample from the bottle (**left**) and the key (**right**) database. Selecting the "square" point as a location for the first finger, "triangle" points correspond to the candidate locations for the second finger, to construct force-closure grasp. The number of pairs of contact points that permit force-closure grasp is larger in **case I** than **case II** and thus the first case is considered more reliable (i.e., more stable) than the second one. The green points correspond to the possible contacts based on the approach.

from up to down (blue regions). Note that almost all regions would permit force-closure grasp in an analysis ignoring shape and contact location uncertainty. However, the proposed quality metric of grasping shows that some regions are more reliable for grasping the bottles than others. The symmetry in the probability is due to the presumption of exchangeability of finger 1 and 2.

The effect of varying the approach center is show in Fig. 2.9. Notice that the approach center has very little impact on feasibility, since the feasible regions for grasping the bottles are almost the same for the three cases. In other words, there are many points that are equally good for grasping elongated objects like the bottles.

2.7.2 Determine feasible locations in the key database

In addition to the bottle dataset, we compute the probability distribution of feasible regions for a database of keys, Fig. 2.2 right panel. We selected the keys because under increasing blur they converge to shapes similar to bottles. Furthermore, Fig. 2.7 shows that the good and bad approach directions for the keys should be similar to the bottles, once the objects main axes are matched. Nevertheless, we show that these two classes of objects have different stability properties under uncertainty.

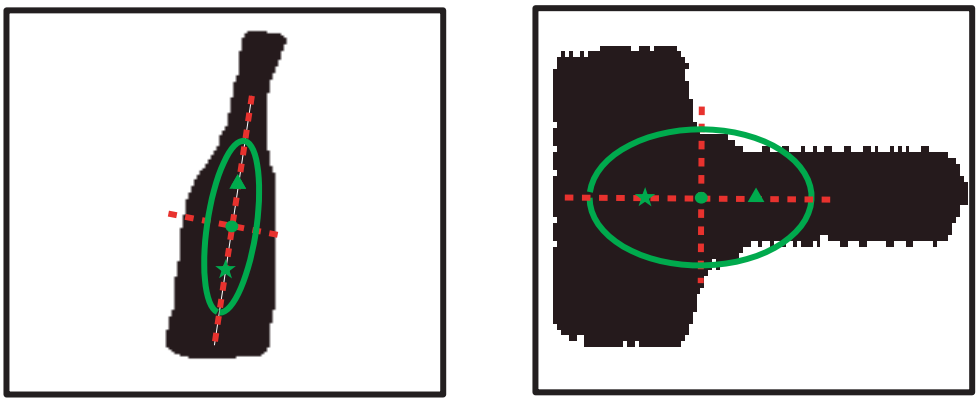

Figure 2.8: Center of approach parameterized by the second moment of the object mass distribution. The second moment is represented by the ellipse, whereas the two dashed lines correspond to the major and minor axis of the ellipse. The center of mass (green dot) is the origin of the ellipse and we compute two points (star and triangle) that lie on the major axis $\pm\sqrt{\lambda_1}/2$ from the center of mass, where λ_1 is the principal eigenvalue. The **left** and the **right** panels of the figure illustrate the second moment of the mass distribution of a typical sample from the bottle and the key database, respectively.

Performing an analysis identical to the bottle case, the probability distribution of the feasible regions for different approach centers are shown in Fig. 2.10. Note that the most "reliable" grasping regions are around the "head" of the key. Furthermore, moving the approach center from the "head" to the "teeth" part of the key, the probability to achieve force-closure grasp decreases. Thus, in contrast to the bottle case, the planned approach center matters for the case of key.

2.7.3 Effects of approach center and finger coupling on stability

The simulation results show that the approach center of grasping an object may significantly affect the probability distribution of the feasible regions. To quantify this effect, we integrate the probability maps across finger approach directions for 11 different approach centers (± 0.2 of the leading eigenvalue) along the object main axis (principal eigenvector), for both bottles and keys. This provides a simple measure of the number of approaches that permit force-closure grasp for a given approach center. The results are shown in Fig. 2.11. While the curve is essentially flat for the bottle database, approaching the key around its "head" significantly improves the chance of achieving force-closure grasp.

Finally, we investigate the effect of finger coupling that results from a parallel two jaws gripper.

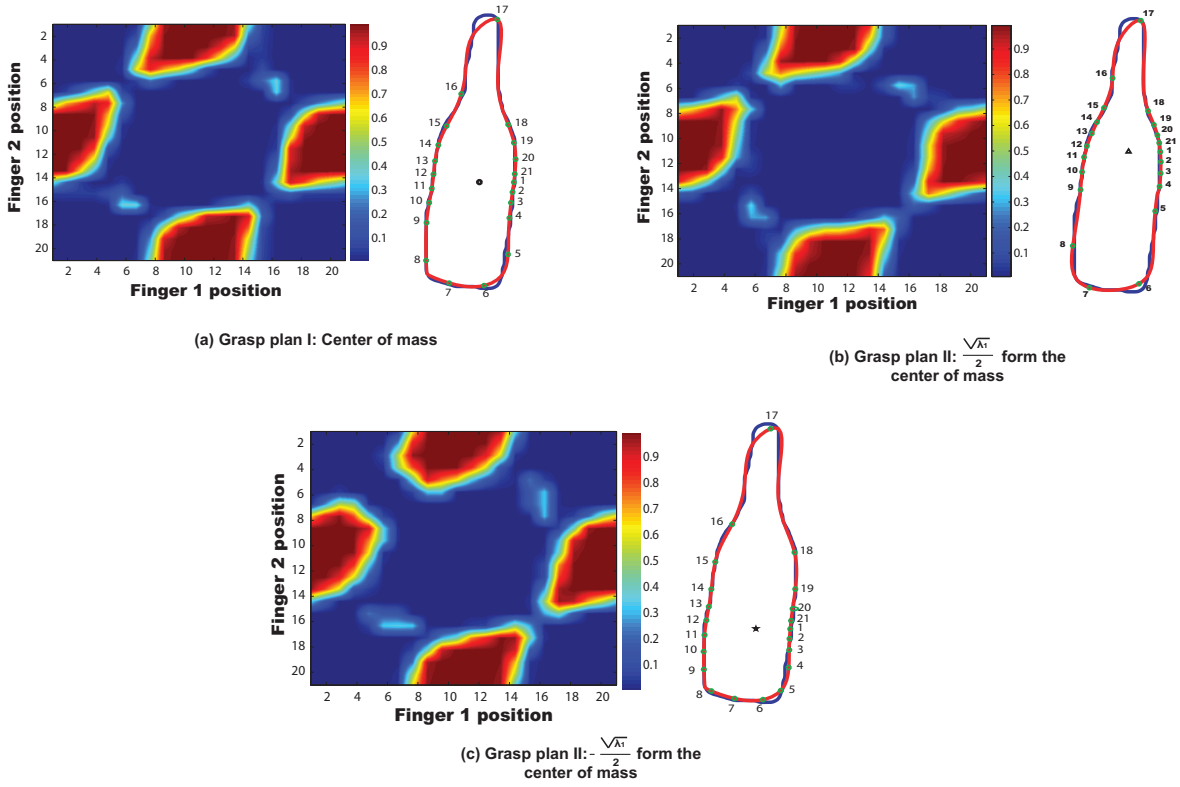

Figure 2.9: Probability distribution of the feasible regions for three different approach centers (see left panel Fig. 2.8). Notice that the pattern of feasible regions is almost independent from the approach center.

In this case, the angular positions of the two fingers are dependent and their directions are opposite. The probability distribution of the feasible regions is shown for both bottle and key database in Fig. 2.12.

The intersection of a set of finger directions with a typical sample of the object boundary is displayed next to the probability distribution maps, sampled at 0.2856 rad (i.e., about 22 contact points). Similar to the previous results, the probability to achieve force-closure grasp is high when the contacts are around the "body" of the bottle, whereas it goes to zero grasping the bottle from up to down. Note that for the key database, there is not any grasp plan that gives force-closure with probability 1. Finally, the advantage of grasping keys at the "head" emerges with the parallel gripper as well, which we believe accords well with intuition and practice for human grasping of individual keys.

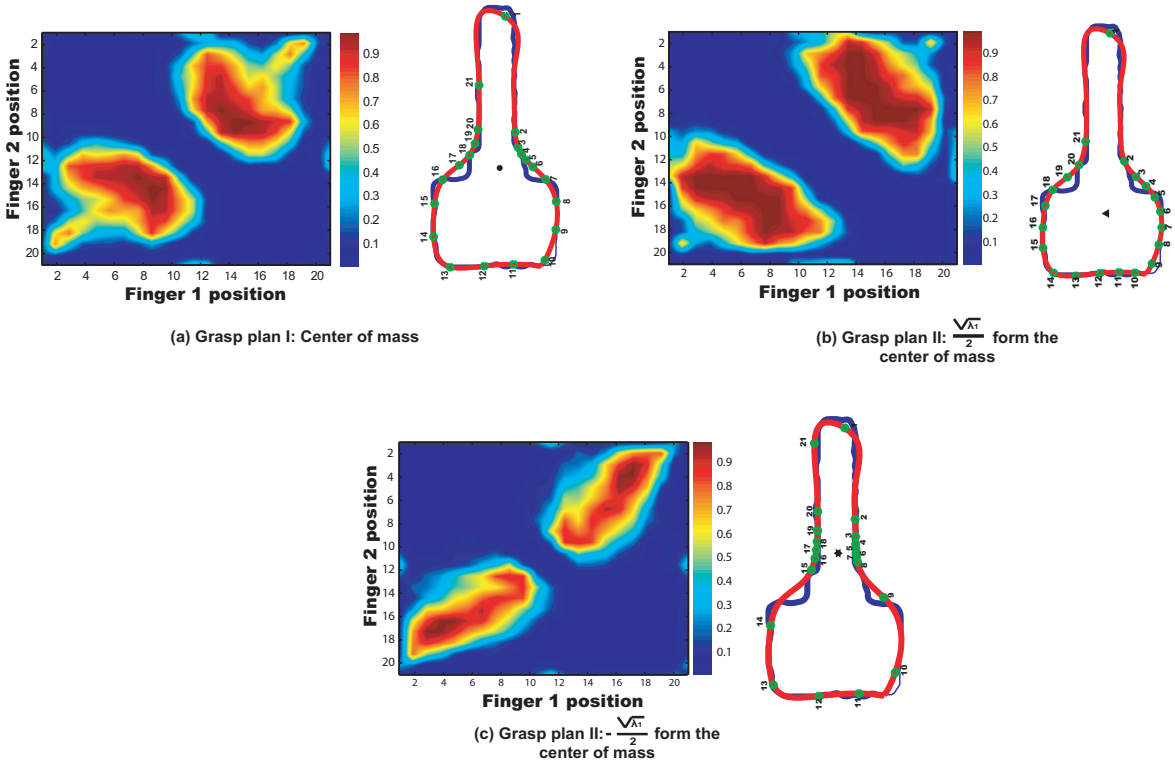

Figure 2.10: Probability distribution of the feasible regions for three different approach centers (see right panel Fig. 2.8). In contrast to the case of bottle, the approach center affects the distribution of feasible regions for the key case.

2.8 Conclusion

In this study, we presented a new approach to identify stable regions for grasping objects in the presence of shape and finger contacts uncertainty. We have focused in 2-dimensional planar objects approximating their shapes with B-spline functions. Modeling the contacts as frictional points, our goal is to compute the probability that a two-fingered grasp plan will result in a force-closure grasp of the object. The main contribution of this work is the development of a method that incorporates uncertainty into grasp stability analysis. We propose a novel quality metric that can be used to identifying stable contact regions taking into account both the objects shape and the finger placement uncertainty. This measure distinguishes the contact stability of points that are equivalent in a standard analysis without resorting to rolling contact or motion perturbations.

One of the advantages of this metric is that it can be applied in different kinds of uncertainty.

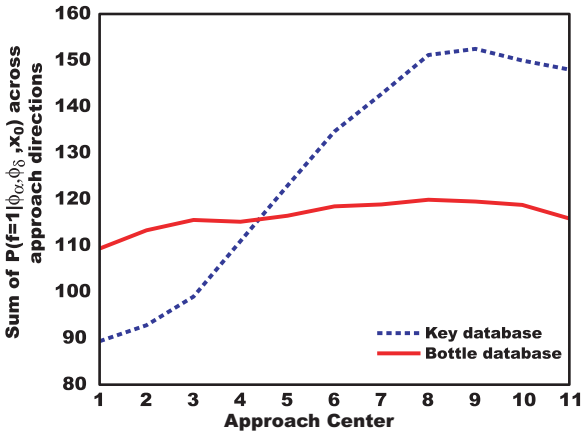

Figure 2.11: Integration of the probability maps across finger approach directions for 11 different approach centers along the main axis of the objects.

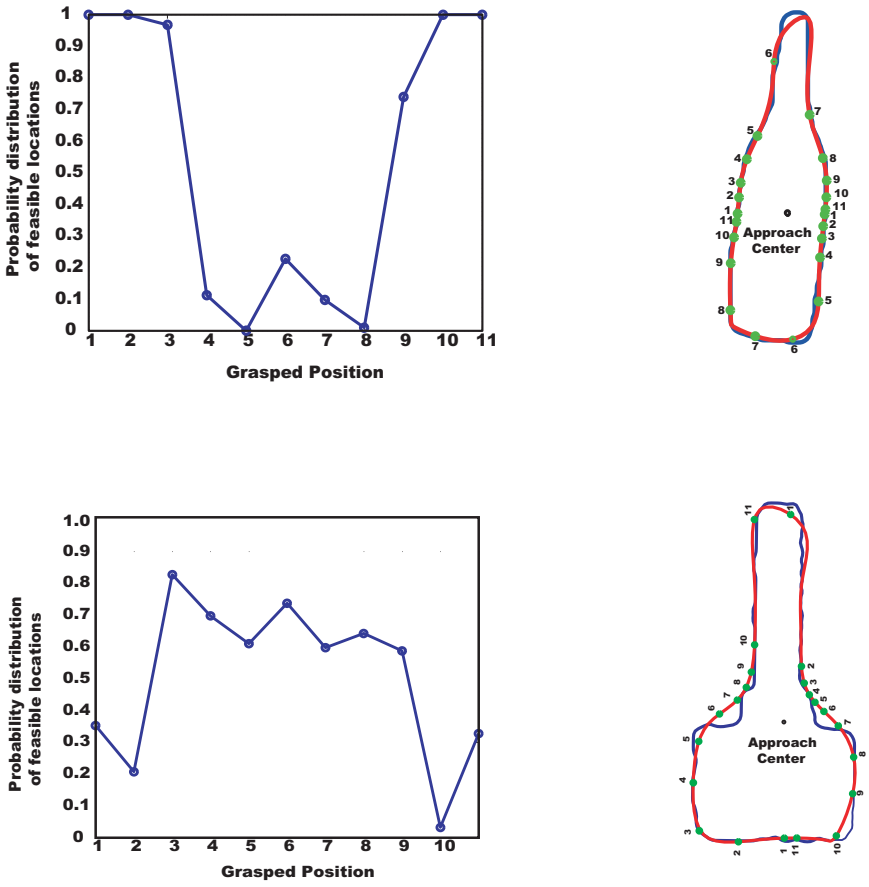

Figure 2.12: Probability distribution of the feasible regions using parallel two jaws gripper. Note only the pairs of contact locations (i, i), with $i = 1 \cdots, 11$ (green points) can be grasped by the parallel two jaw gripper.

Particularly, on the next chapter we present a study in which the proposed method is used to evaluate human performance in grasping objects with directional position uncertainty.

Chapter 3

Effects of position uncertainty in grasping movements

3.1 Overview

Due to noisy motor commands and imprecise and ambiguous sensory information, there is often substantial uncertainty about the relative location between our body and objects in the environment. Little is known about how well people manage and compensate for this uncertainty in purposive movement tasks like grasping. Grasping objects requires reach trajectories to generate object-fingers contacts that permit stable lifting. For objects with position uncertainty, some trajectories are more efficient than others in terms of the probability of producing stable grasps (i.e., force-closure grasping). We hypothesize that people attempt to generate efficient grasp trajectories that produce stable grasps at first contact without requiring post-contact adjustments. We tested this hypothesis by comparing human uncertainty compensation in grasping objects against optimal predictions. Participants grasped and lifted a cylindrical object with position uncertainty, introduced by moving the cylinder with a robotic arm over a sequence of 5 positions sampled from a strongly oriented 2D Gaussian distribution. Preceding each reach, vision of the object was removed for the remainder of the trial and the cylinder was moved one additional time. In accord with optimal predictions, we found that people compensate by aligning the approach direction with covariance angle to maintain

grasp efficiency. This compensation results in higher probability to achieve stable grasps at first contact than non-compensation strategies in grasping objects with directional position uncertainty, and the results provide the first demonstration that humans compensate for uncertainty in a complex purposive task.

3.2 Introduction

Optimal sensorimotor control models actions as decisions that maximize the desirableness of outcomes, where the desirableness is captured by an expected cost or utility to each action sequence. These models provide explanations for many aspects of our ability to compensate for uncertainty [79,98,127]. In particular, humans are near optimal at integrating sensory information with internal models of motor actions to produce estimates of world states and action consequences [42, 43, 85, 112]. Moreover, people maintain and update estimates of their uncertainty, and use this information to improve task performance and economic gain [11, 70, 77, 81, 97, 149]. The vast majority of research on optimal visuomotor control involves point-to-point movements. However, these studies have neglected normal purposive movements involving the application of forces to objects in our environment, with the intent of changing either the object's motion, as in grasping, or our own motion, as in walking. Planning for such movements requires anticipating the effects of object-body contact on subsequent dynamics. Due to the complexity of anticipating the effects of applied forces to object motion, it is significantly more challenging to adapt the optimal sensorimotor control framework to problems like grasp planning, and it is much less clear that the visuomotor system will have models complex enough to allow for optimal control strategies.

In grasp planning, fingers must be targeted toward points on the object's surface that will allow the application of forces sufficient for lifting and dexterously manipulating the object. In particular, the finger-object contacts should permit forces that are capable of stably lifting the objects and counterbalance external forces and torques exerted on the object (*force-closure grasping*) [165,177].

Once people place their fingers on contact points supporting force-closure, they can begin to lift the object. Hence, the duration of a grasping task depends on the time to produce force-closure grasping, and this time is minimized by movement trajectories that produce force-closure at first

contact. Failure to satisfy force-closure conditions at first contact requires subsequent adjustments to rearrange the contact points - a process that requires extra time and effort. Little is known about how people recognize contact points supporting force-closure or how this process is affected by uncertainty.

The purpose of this work is to study uncertainty compensation in grasping and compare human performance against normative predictions. An illustration of precision grasping objects with position uncertainty is presented in Fig. 3.1. If the position of the cylinder is precisely known, all the movement trajectories will produce force-closure grasping at first contact. However, if the cylinder position is distributed along a strongly oriented 2D Gaussian distribution, some of the movement trajectories are more efficient in terms of force-closure grasping than others. The probability of achieving force-closure grasping at first contact as a function of index finger/thumb approach is presented in Fig. 3.2. (see appendix A and Results section for more details). The grasp trajectory that produces force-closure grasping irrespective of the cylinder position involves index finger and thumb approaching the distribution center in opposite directions along the axis of maximal uncertainty. This predicts that people should reorient the approach direction of their hand to grasp the cylinder along the direction of maximal uncertainty.

We test what, if any, changes in grasping strategy occur as compensations for object location uncertainty. Using a robotic arm to generate oriented distributions of cylindrical object locations, we investigate whether people adopt grasping strategies that minimize the impact of uncertainty on grasp success in terms of force-closure grasping at first contact.

3.3 Results

A schematic representation of the apparatus is shown in Fig. 3.3 Participants were instructed to reach rapidly with the right hand to precision grasp and lift a cylindrical object mounted on a robotic arm, in 3 conditions that varied in the amount of position uncertainty. In one condition the cylinder was stationary throughout the reach (**no motion condition**). In the other two, the object visibly moved through a series of randomly drawn positions. After the object was occluded, it either moved to a new random location (**random-end location condition**) or to a fixed location (**fixed-end location**

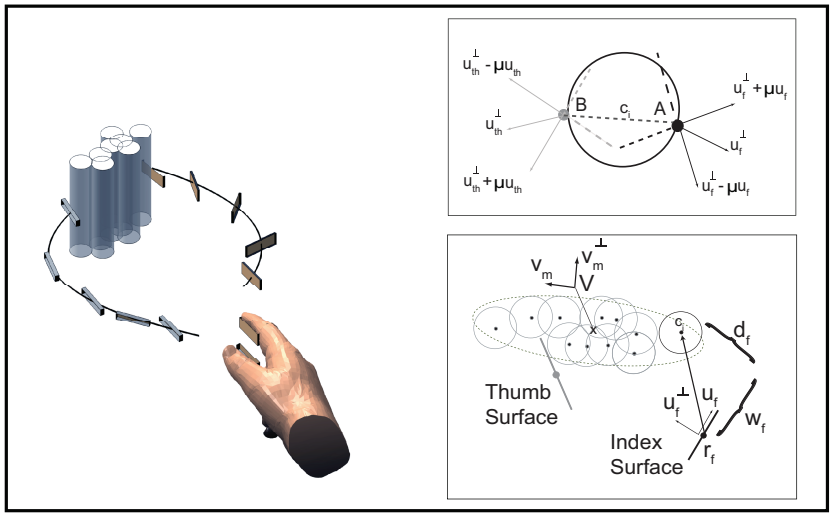

Figure 3.1: Graphical illustration of grasp analysis with directional position uncertainty. The critical aspect of grasping an object with position uncertainty is the control of the contact surfaces of the index finger and thumb (rectangular patches). These surfaces must be moved along paths that will make appropriate contact with the object at any of its possible locations (gray transparent cylinders). Appropriate contact involves the concept of force-closure (see materials and methods). *Upper inset*: Force-closure grasping representation. Assume that a reach trajectory results in two contact points of the index finger (A) and the thumb (B) on the surface of the cylinder $\mathbf{c}_i$.This trajectory produces force-closure grasping because the line segment (AB) is located between the two friction cones defined by the contact points A and B. Based on the Coulomb's law, two contact points produce force-closure when the component of the contact forces at these points in the direction of the surface normals $(\mathbf{u}^{\perp})$ exceeds the coefficient of friction μ times the tangential components. The friction cones are determined by the vector $\mu\mathbf{u}_{\cdot}^{\perp} - \mathbf{u}^{\perp}$ and $\mu\mathbf{u}_{\cdot}^{\perp} + \mathbf{u}^{\perp}$, where $(.)$ corresponds to subscript *th* and *f* for the thumb and the index finger, respectively. Note that **u** refers to the surface tangents. *Lower inset*: Graphical representation of the fingers' contact surface approach for grasping a cylindrical object with directional position uncertainty. The thumb and the index finger contact surfaces are displayed as line segments with local position **r** and normals **u**. For visualization reasons, we present only the characteristics of the index finger, whereas the characteristics of the thumb is similar to the index finger, but with the subscript *th*. The gray circles describe the possible cylinder locations based on the object's position distribution, which is illustrated as ellipse with center **x** and major and minor axes $\mathbf{V}_m$ and $\mathbf{V}_m^{\perp}$, respectively. Given a possible cylinder location $\mathbf{c}_i$, the reach trajectory will produce force-closure if the line segment defined by contact points of the thumb and the index finger surface on the cylinder surface, is between the two friction cones at the two contact points. Note that (w, d) corresponds to the local contact coordinates of the index finger (with subscript *f*) and thumb (with subscript *th*) (see materials and methods section).

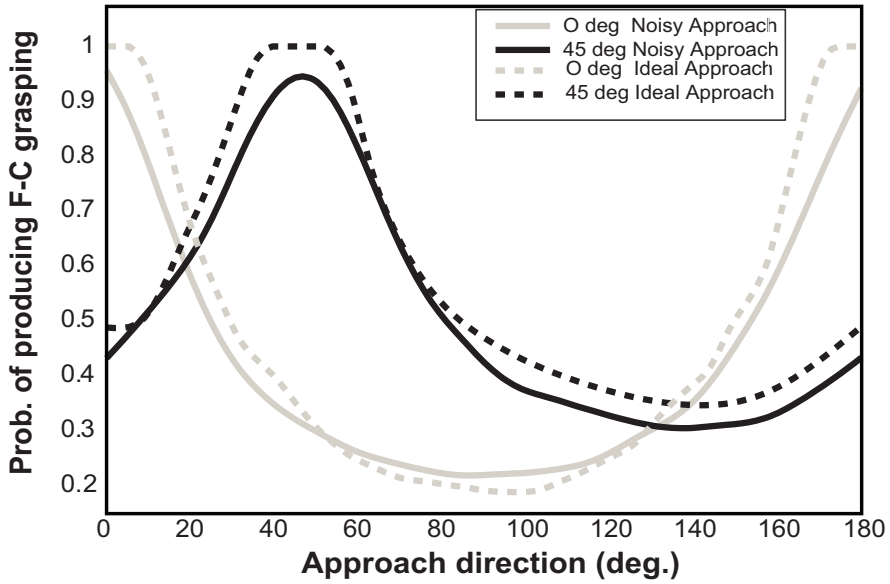

Figure 3.2: Effects of approach direction in the probability of producing force-closure for ideal (dashed lines) and noisy (solid lines) approaches for 0° (gray) and 45° (black) covariance orientations. Noisy approaches were generated by adding noise to both approach direction (variance $= 4.5\ deg.^2$) and fingers orientation (variance $= 2.5\ deg.^2$).

condition). The chance that the reach trajectory will end with the fingers making object contact at points permitting force-closure depends on the path the index finger and thumb take to the object. The critical part of the trajectory occurs near the end of the movement, when the fingers approach possible object locations.

Trajectory characteristics are illustrated for a single participant on the no-motion (left), fixed-end location (middle) and random-end location (right) conditions in Fig. 3.4, which shows statistics on the set of trajectories in each condition. The three panels display the frequency that trajectories passed through each spatial location as a color map, where blue indicates probabilities near zero and red indicates high probability regions. The position distribution of the cylinder is illustrated by the white ellipse. In addition, we computed the average velocity and orientation of the contact surfaces of both index finger and thumb at each spatial location. The results illustrate the highly stereotyped trajectories in this experiment, with an initial forward transport phase that brings the index finger and thumb near the object, followed by an approach period in which both digits move

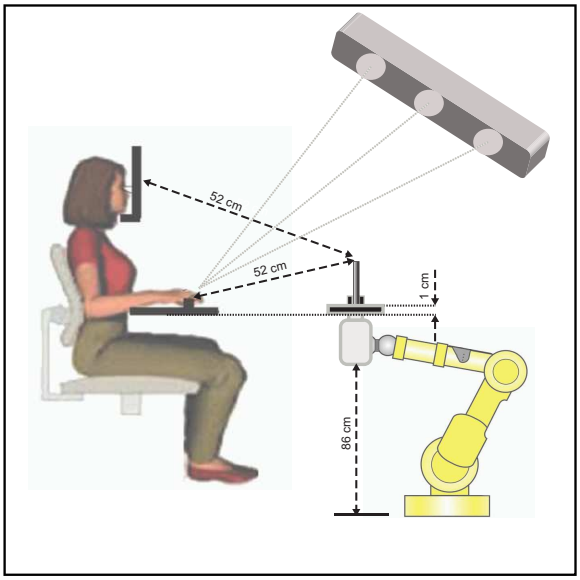

Figure 3.3: The experimental apparatus used in this study.

more slowly and mainly in a direction perpendicular to the contact surface of the fingers. Note that this perpendicular approach is a critical component for producing force-closure grasping at first contact and that it is much more prominent in the random-end location condition. In addition, there are significant differences on the grip aperture profile across the 3 conditions. While grip aperture remained narrow for most of the reach trajectory in the no-motion condition, it widened near the beginning of the trajectory in the random-end location and fixed-end location conditions. Interestingly, grip aperture is larger in the fixed-end location condition than the no-motion condition, suggesting that object motion induces uncertainty even for an object felt to be in exactly the same position on every trial.

We investigated whether participants modified their index finger/thumb approach direction with the orientation of the object position distribution. We predicted a change in approach direction from an analysis of the conditions for force-closure at first contact. Force-closure occurs when the fingers make contact on the object at locations that permit the application of forces in the direction of both the surface normals and surface tangents that can potentially cage the object. A necessary condition for force-closure is that the required tangential forces are less than the forces applied to the surface

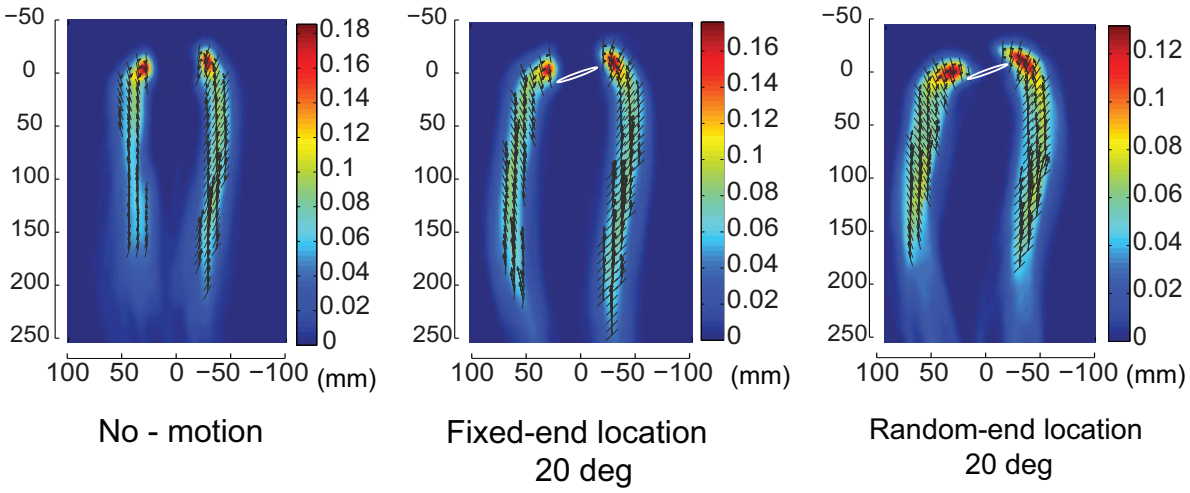

Figure 3.4: Examples of trajectory characteristics for the three conditions, **left**: no motion, **middle**: fixed-end location and **right**: random-end location. The reach strategy in each condition is revealed by an analysis of the average orientation (black line segments) and velocity (arrows) of the finger's and thumb's contact surfaces at each location along the trajectories. A superimposed density map shows the probability of a trajectory passing through each spatial location, where blue and red indicate zero and high probability, respectively.

normals, scaled by the coefficient of friction. Geometrically, this relation produces friction cones at the contact points of the thumb and the index finger with cylinder, whose boundaries are determined by the surface tangent and normal vectors of both fingers (Fig. 3.1 upper inset). In the presence of object location uncertainty, approach direction affects the ability to achieve force-closure, as illustrated in Fig. 3.1. Particularly, Fig. 3.1 shows a graphical representation of the trajectory of the index finger and thumb contact surfaces (rectangular patches) to an array of possible object locations, displayed as transparent cylinders. The relevant geometry for computing force-closure for a possible cylinder location is presented in the lower inset. The center of the distribution of cylinder locations is shown as $\mathbf{x}$, the principal axis of uncertainty as $\mathbf{v}_m$ and the thumb and index finger contact surfaces are shown as line segments, with local position $\mathbf{r}$ and direction $\mathbf{u}$. For each possible cylinder location $\mathbf{c}_i$ force-closure is only possible if the cylinder surface is in the approach path for both digits (w_f is less than the finger surface width) and the angle between the index finger and thumb is sufficiently large.

On the basis of this analysis, the choice of a grasp strategy can be turned into a statistical decision problem, where the objective is to select an approach that maximizes the probability of force-closure at first contact (see Materials and Methods section). The analysis shows that the optimal approach direction is aligned with the major axis of the covariance of cylinder locations. For a given trajectory, we can compute the probability of force-closure by determining the proportion of sample cylinder locations that satisfy the force-closure conditions. Fig. 3.2 shows the theoretical impact of varying approach direction on the probability of force-closure for ideal approaches (dashed lines) and noisy approaches (solid lines) generated with random perturbations added to both the approach direction (variance $= 4.5\ deg^2$) and the finger surface orientations (variance $= 2.5\ deg^2$). The results are shown for two orientations of object location uncertainty, 0° (gray) and 45° (black). The principal effect of additional variability is to narrow the range of approaches that produce high force-closure probabilities.

3.3.1 Approach direction compensation

If participants exhibit the predicted compensation, we should observe approach direction vary to align with the axis of maximal uncertainty. We estimated the planned approach direction for each participant and condition by computing the covariance of sensor positions across trajectories, illustrated in Fig. 3.5A. The direction of approach was extracted from the principle axis of the covariance spatial distribution of finger locations across the set of trajectories gathered over the ten time steps closest to the average first contact (see Materials and Methods section). To insure the covariance estimates were based on compatible trajectory points, we restricted the analysis to a cluster of trajectories with similar temporal characteristics, comprising about 80% of the trajectories in an experimental condition. This measure captures how trajectories are spatially constrained near contact, with the main axis providing a measure of the direction of the constraint, and the ratio between major and minor axes of the covariance provides a measure of the importance of the constraint. The major/minor axis ratio, averaged across participants for each covariance angle is plotted in Fig. 3.5B, shows that the approach direction of the index finger is significantly more constrained

than the thumb. Constraint differences in the index finger and thumb may be explained by differences in the timing of first contact - the index finger typically contacted before the thumb. Once contact is made, there are additional forces on the hand affecting the trajectories and additional information about the object's location that may influence the subsequent trajectory path. In fact, we found that trajectories in the thumb frequently exhibited direction changes after first contact by the index finger. These changes may arise because the index finger is longer and has a degree of freedom more than the thumb, making adjustments to the location and orientation easier.

Because the data suggest that locus of control is the index finger, we focused our analysis of approach direction on the index finger, shown in Fig. 3.5C. In the random-end location condition, where the final object location varied unpredictably, approach direction is significantly related to the object uncertainty direction ($R - square > 0.8038, F_{[0.05;1,3]} > 12.2905$ and $p < 0.0393$), and scales almost linearly for all participants. However, all participants' slopes were less than predicted by ideal compensation (shown by the black discontinuous line). In contrast, for the fixed-end location condition, where the final position was fixed across trials, the approach direction was near constant (Fig. 3.5D).

3.3.2 Does compensation increase the probability of force-closure grasping?

To quantify how much the change in approach direction observed in the random-end location condition affected grasp efficiency, we computed the probability of force-closure for each participant and covariance angle. We estimated the force-closure probability for each trajectory by determining the proportion of sampled object locations that would satisfy the force-closure conditions at first contact, and averaged across trajectories (see Materials and Methods section). An ideal grasp strategy with no approach noise has a probability of one. To illustrate the computation, two different trajectories of a single participant with high and low probability of force-closure are shown in Figs. 3.6A and 3.6B, respectively. Sample cylinder locations are shown in gray, red describes the actual cylinder position, and the approach of the index finger and thumb contact surfaces are illustrated by a time series of line segments. In Fig. 3.6A the index finger makes contact with a sample cylinder location (black), which given the approach of the thumb, satisfies the criteria for force-closure. In fact,

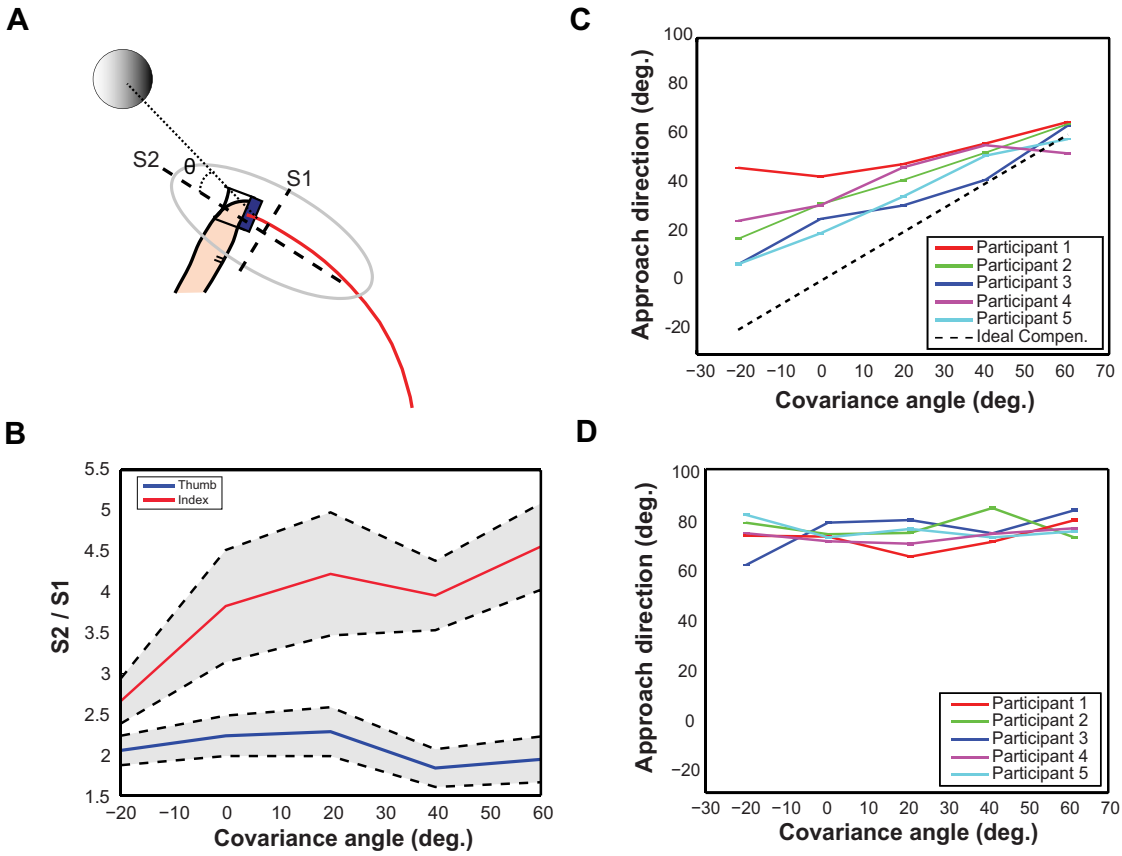

Figure 3.5: (**A**): Diagram illustrating the approach direction computation and definition of the covariance angle. The gray solid circle represents the cylinder location, the red line represents the average trajectory, and ellipse represents the covariation of the spatial distribution of finger locations across trajectories for the last 10 time steps preceding contact. S1 and S2 correspond to the minor and major axes of the trajectory covariance ellipse, and approach angle θ is the angle between S2 and the x-axis (dotted line). (**B**) Average ratio S2/S1 across participants for each covariance angle of the major and minor axes of the trajectory covariance for the thumb (blue line) and the index finger (red line), with standard errors shown in gray. (**C**) Approach direction for each covariance angle and participant in the random-end location condition. Error bars are ± 1 standard error. The black discontinuous line shows ideal compensation. All participants less than fully compensate with slopes (0.26, 0.4, 0.58, 0.65, 0.67) uniformly less than the ideal of 1. (**D**) Same as C for the fixed-end location condition.

this trajectory will produce force-closure for almost all the cylinder locations generated from this distribution (0° orientation). In contrast, the trajectory in Fig. 3.6B fails to produce force-closure for the location shown in black, and for most of the other sample locations.

The probability of force-closure provides a measure of the benefits of modifying approach direction with uncertainty. Fig. 3.6C shows the results (averaged across covariance angles) from the random-end location condition. To provide a baseline measure of performance, we compared these results to a simulated non-compensation strategy, in which we compute the probability of force-closure for each covariance angle using the trajectories from the no-motion condition (see Materials and Methods section). The difference between these probabilities is a measure of the benefits achieved by approach compensation.

We can also gain insight into the benefits of compensation by focusing on the set of trajectories with low performance. We identified the set of trajectories that produced force-closure for less than 20% of sample locations (values between 20% and 50% produced similar results). Because these trajectories will require post-contact adjustments in fingers positions before lift occurs for the majority of cases, we call this measure the *proportion of inefficient trajectories*. The results from this analysis were compared with the results from the hypothetical scenario, in which people do not compensate (simulated non-compensation strategy) across all covariance angles. Note that participants showed large differences in this measure but similar trends. To make these trends easier to visualize, we subtracted the mean across covariance angles of this measure from each participant's data. The results are shown in Fig. 3.6D. On average there were fewer inefficient trajectories in the random-end condition than the simulated non-compensation strategy. The dashed and the solid lines summarize the regression results across participants for both the simulated non-compensation strategy and the random-end location condition. In accord with expectations, a non-compensation strategy produces inefficiency curves that significantly vary as a function of covariance angle (R-square $= 0.9309$, Slope $= -0.0022$, $F_{[0.05;1,3]} = 40.4193$, p $= 0.0079$). In contrast, the inefficiency curves in the random-end location condition show that by modifying approach direction, participants were able to maintain a low inefficiency rate for all covariance angles (R-square $= 0.0015$, Slope $= 3.4900e-005$, $F_{[0.05;1,3]} = 0.0044$, p $= 0.9513$). Moreover, a test of the two regression

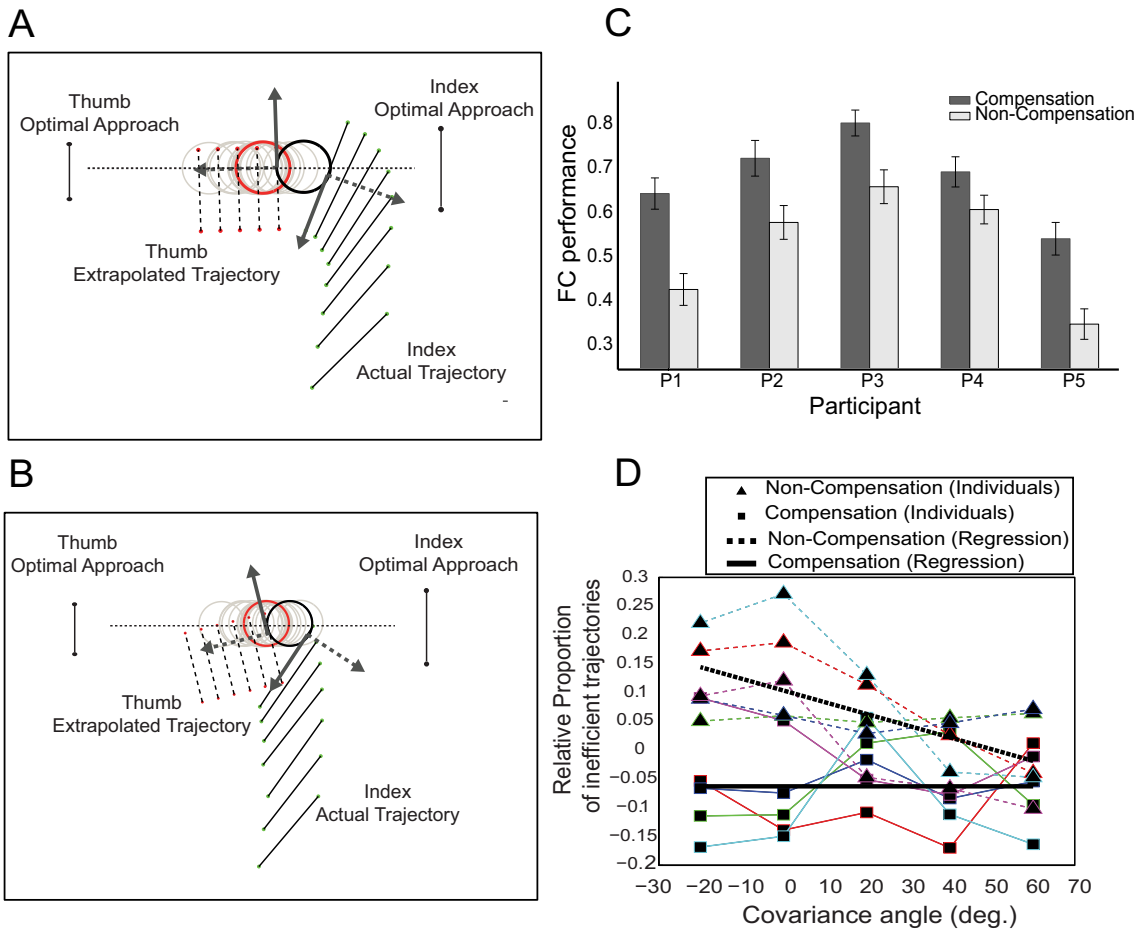

Figure 3.6: (**A**) Illustration of the analysis for computing force-closure for a given reach trajectory. Gray circles represent possible cylinder locations sampled from a covariance matrix with major axis along the dotted line, and the red circle shows the actual cylinder location. Index finger and thumb contact surface locations are illustrated by a time series of line segments. The black circle shows index finger contact with a sampled cylinder location. Once the index finger contacts a possible location, the thumb is extrapolated to assess whether the trajectory would satisfy the conditions for force-closure. This reach trajectory produces force-closure grasping. (**B**) Illustration of a trajectory with force-closure failure for most of the sample locations. (**C**) Probability of producing force-closure is shown for each participant adjacent to a simulated non-compensation strategy. (**D**) Relative proportion of inefficient trajectories trajectories that produce force-closure for less than 20% of sample location. Square and triangle points represent estimates of the proportion of inefficient trajectories vs. covariance angle for each participant (each color corresponds to a particular participant same as Figs. 3.5C and 3.5D). Note that ± 1 standard errors of these estimates are so small that are not visible as error bars on the figure. Dashed and solid lines show the regression results across participants

results showed that these trends are different (ANCOVA, $F_{[0.05;1,6]} = 11.95$, p = 0.0135).

3.3.3 Effects of position uncertainty on grip aperture profile

We also tested whether people modify their grip aperture profile as a function of condition and covariance orientation, by computing the mean value of the maximum grip aperture (MGA) across trials and regressed the results against covariance angles. For all conditions, we found no significant variation of MGA magnitude or time with covariance angle. However, there were significant differences across conditions for all participants (one-way ANOVA, $F_{[0.05;1,598]} > 106.4595$ and p < 0.001) excluding Participant 5, shown in, Fig. 3.7.

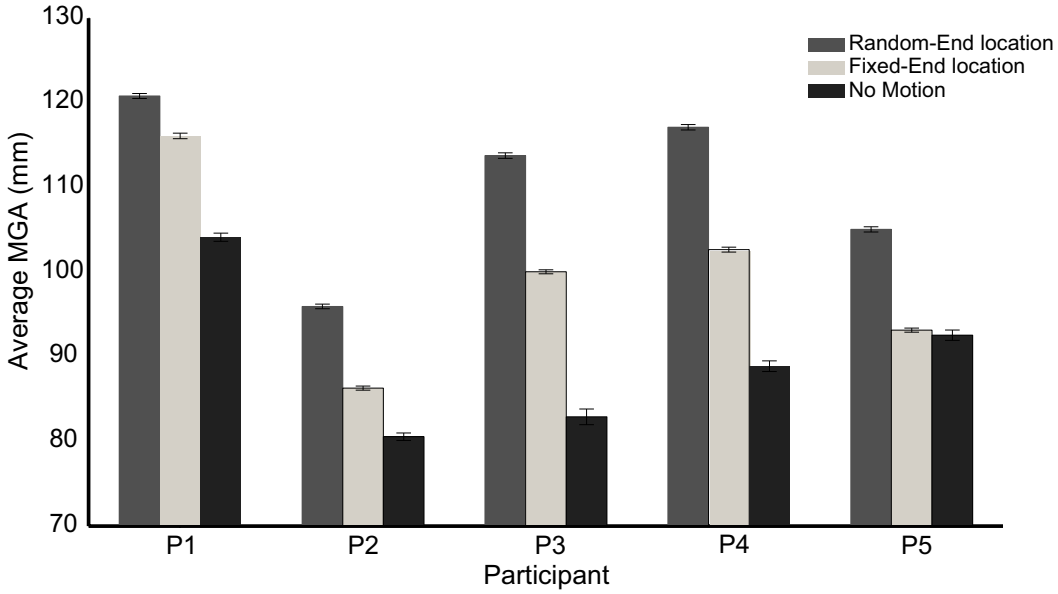

Figure 3.7: MGA averaged across trajectories and covariance angle for each condition and participants

Interestingly, almost all participants increased their gripwidth on the "fixed-end location" condition in response to the observed object motion, despite the fact that the final object position is both visible and always the same.

3.4 Discussion

We have adopted principles from Statistical Decision Theory [36] to account for human behavior in a purposive movement task: grasping objects with position uncertainty. Previous studies have applied Statistical Decision Theory to model reach behavior, providing evidence that the sensorimotor system's computation can be modeled as Bayes optimal, incorporating proprioceptive and environmental information to minimize the effect of uncertainty on task performance [70, 78–81, 97]. To simplify modeling and the assessment of optimality, these studies have focused on artificial environments and simple tasks involving point-to-point reaching movements. It is quite challenging to extend the optimality approach to the study of purposive movements. The goals and the consequences of such movements are determined by the application of forces and the effects of noise and uncertainty, but movement plans need to be expressed in terms of limb motions. Previous studies involving purposive movement tasks have provided evidence that people modulate their grasping strategies when they can predict changes in objects' intrinsic characteristics, such as center of mass [71, 75, 76, 120], surface shape [123], texture [146] and weight [147]. Particularly, the sensorimotor system uses information acquired from previous manipulations of the same object to select digit contact points and the forces required for object manipulation. However none of these studies provide models that can explain the anticipatory motor behavior that participants adopted in grasping. One of the novelties of the current work is that we used normative predictions to evaluate the benefits of uncertainty compensation, based on the hypothesis that participants attempt to minimize overall the grasp time and use this idea to construct a natural cost function on grasp approach based on the concept of force-closure grasping at first contact. We showed how the approach phase of a reach trajectory determines the time efficiency with which an object can be grasped and lifted, and generated testable predictions: participants should modify approach to allow grasp closure along the direction of maximal uncertainty and increase peak gripwidth (see appendix A). We observed both kinds of compensation strategies across conditions; a gripwidth change without approach modification in the fixed-end location condition, but both gripwidth and approach changes in the random-end location condition. Previous studies have also observed gripwidth compensation for uncertainty. In particular, MGA increases without visual information [13], and people modify their MGA with the

amount of visual uncertainty about object position [55, 102]. However, MGA did not scale with the orientation of the cylinder position distribution.

Note that modifying the approach direction requires extra energy to rotate the hand, which means that the advantages of compensation in terms of efficiency must outweigh these costs. Non-compensation strategies increase the chance of not producing force-closure at first contact, which must be corrected by time-consuming and metabolically costly finger repositioning after contact. Finger repositioning occurs in a sensory feedback loop that takes time. Contact locations and forces must be sensed and appropriate adjustments computed and executed, with a minimum time lag around 200 ms [71]. Grasping is also frequently time critical - an object can potentially move during a reach, or the initial contact by one finger can impart an impulse which will move the object if not quickly counteracted by the opposing finger. In addition, in many tasks if force-closure is not met at first contact, there may not be a second chance for grasping the objects. Hence, good initial contacts minimize natural costs associated with time and energy expended during corrective movements and reduce the chance of negative results.

The probability of achieving force-closure grasping is not the only criterion used to plan grasping movements, and our results showed that participants did not fully optimize this measure. Grasp planning may attempt to optimize other cost criteria in addition to force-closure grasping at first contact. Possible biomechanical cost functions, such as energy expenditure [145], joint mobility [88], muscle tension changes [109], mean torque changes [176], mean square rate of change of acceleration [156], and peak work [87] create competing criteria and constraints that must be simultaneously satisfied (see also [80]). Hence, perfect compensation may have been difficult to achieve for some covariance angles and the additional energy required may not be worth the small gain in grasping performance [133]. Especially, participants may sacrifice perfect compensation to increase comfort of their grasp [144]. Another possibility is that trajectories are selected to minimize the uncertainty in hand and finger positions [31]. Because participants grasped the object while it was out of view, this kind of uncertainty may have been non-negligible. However, in Fig. 3.2, we showed that simulated errors in hand and finger position actually narrow the ranges of approaches that produce high force-closure probabilities, and reduce the probability of producing force-closure grasping.

It is important to note that our analysis of optimal grasping behavior with position uncertainty will not hold in all contexts. In the optimal analysis we permitted differences between the thumb and index finger contact times. This is appropriate for our experiment because the cylindrical object was held in a cradle. In general, time differences will not affect sufficiently heavy objects. For objects light enough to be toppled by contacting with one of the fingers, there will be an advantage to contacting the object with both fingers simultaneously. For this class of objects, there is a trade-off between minimizing the chance of knocking over the object and maximizing the chance of contacting the object. For instance, catching a frisbee by opening the fingers wider increases the chance to contact the object, but decreases the chance to catch it by contacting with both fingers simultaneously. We can extend the current analysis using similar Statistical Decision Theory principles and adding a new cost to penalize non-simultaneous contact of both fingers with the object.

An interesting question is what cues drive the compensation strategies we observed. Like previous studies, that showed integration of visual and proprioceptive information in motor tasks [153, 162, 163], participants may use visual and/or haptic feedback from the finger-cylinder contact to compensate for the position uncertainty of the object. Comparing fixed-end location and random-end location conditions suggests that the haptic error participants experienced in the latter condition is critical for compensating approach direction. Although participants observed the distribution of object position in both fixed-end location and random-end location conditions, only when they felt the location variability did they modify their approach direction. Nevertheless, the visual movement is not without effect. Particularly, we found gripwidth varies between the fixed-end location and random-end location conditions for most of the participants (excluding Participant 5). The results suggest that the sensorimotor system cannot ignore the cylinder motion even when it is uninformative. However, we found that participants did not adjust the approach direction with the covariance angle on the fixed-end location condition, but rather had a preferred approach direction of about 70° for all covariance angles.

We also examined whether there was evidence of learning by dividing trajectories into "early" and "late" groups and compared their characteristics. We did not find any significant differences in trajectory characteristics between the two groups, for any attempted split. The absence of significant

learning effects is likely due to trajectory variability and the number of trials (100). However, it may also indicate that uncertainty compensation strategies are relatively constant.

In conclusion, the results show that people plan for the effects of uncertainty in selecting object contacts in purposive movement tasks.

3.5 Materials and Methods

3.5.1 Participants

Five right-handed (25-30 years old, 4 men and 1 woman) participants with normal or corrected-to-normal vision participated in the study for monetary compensation. The appropriate institutional review board approved the study protocol and informed consent was obtained based on the Declaration of Helsinki.

3.5.2 Apparatus

Participants were instructed to reach rapidly with and then use a precision grasp to lift a cylindrical object (2.2 cm diameter and 11.5 cm height) held in a cradle on a platform mounted on a robotic arm that precisely moved the object ($<$ 1 mm error), Fig.3.3. Trajectory data were recorded by placing three infrared sensors on hard foam blocks attached to the fingernails of both index finger and thumb, which were tracked via an Optotrak 3020 with sampling rate 100 Hz. Reaches began with index finger and thumb placed on a reference block located 52 cm away from the average position of the cylinder and 1 cm above the platform plane. For convenience, we transformed all data to a coordinate frame in which the x-dimension corresponds to a straight line connecting the midpoint of the finger starting location to the midpoint of the average of the cylinder contact locations. The y-dimension is formed from the cross-product of the x-dimension and the cylinder's main axis. Finally, the z-dimension is perpendicular to x and y-dimension. Head-stabilized (via chinrest) participants viewed the cylinder at a distance of 52 cm through liquid crystal glasses which were used to occlude the object during reach time. Ear plugs and closed ear headphones were used to eliminate auditory cues to the motion of the object while it was out of view. A trip switch

guaranteed the object was lifted at least 5 mm.

3.5.3 Experimental paradigm

Participants selected a comfortable reference position by placing both fingers along the top edges of the reference block at the beginning of the experiment. At the start of each trial, participants viewed the cylinder for a period of time that depended on condition, and then vision was removed by shutting down the crystal liquid glasses. Thereafter, they were cued to rapidly reach, precision grasp and lift the object within 1200 ms while it was out of view. The trial was considered successful if the participant lifted the cylinder to trigger the switch within the timeout, however, none of the participants failed to grasp the cylinder within 1200 ms. The fingers had to be returned within 3 mm of their starting positions before the next trial was begun.

Participants were familiarized with the task by running a number of training trials on the non-motion condition. Once they were ready and felt comfortable with grasping the cylinder, the real trials began. On the no-motion condition the cylinder was stationary and the view time was 1 sec before glasses occluded the vision of the object. In the fixed-end location condition, the robotic arm moved the cylinder over a sequence of 5 random positions (1 sec each) sampled from a strongly oriented 2D Gaussian distribution. The cylinder was returned to the based (initial) position and the view was occluded after 1 sec. Thereafter, participants reached and grasped the cylinder, while it was out of view. Note that participants were told that the cylinder always returned to the base position. In the random-end location condition, the cylinder moved over a sequence of 5 positions (1 sec each) randomly generated by a strongly oriented 2D Gaussian distribution. Thereafter, the view of the object was occluded and the object moved to a new random position selected from the same Gaussian distribution. Finally, participants reached and grasped the cylinder, while it was out of view. In this condition, participants were told that the cylinder moved to a new position from within the same distribution of the 5 visible positions. For both fixed-end location and random-end location conditions, we used an 80° range of distribution orientations $(-20^\circ, 0^\circ, 20^\circ, 40^\circ, 60^\circ)$, designed to fit within, but strongly challenge participants' natural biomechanical reaching posture. The standard deviations of the major and minor axes of the covariance were 12 mm and 0.25 mm,

respectively. Note that the covariance angle was defined with respect to the x-dimension of the coordinate frame. Trials from each covariance angle were blocked, and 100 trials of reaching, grasping and lifting the cylindrical object were performed for each block.

3.5.4 Spatial trajectory data

Kernel density estimation was used to analyze the spatial distribution, velocities and orientations of the thumb and index finger trajectories as illustrated Fig. 3.4. We computed the frequency that reach trajectories passed through a grid of spatial locations (1 mm $\times$ 1 mm) in the 2D space (ignoring z-axis). We produced a density estimate from the frequency data using a Gaussian Kernel with standard deviation of 5.5 mm. The colors of the density map describe the probability density values with red corresponding to high and blue corresponding to low density regions. Smoothed estimates of the average velocity (arrows) and orientation (line segments) at each spatial location were also computed, because the number of measurements varied across cells. For each cell, velocity and orientation estimates were generated by performing a weighted average of these values from trajectories across neighboring cells, using a Gaussian filter with standard deviation of 3.5 mm as a weighting function.

3.5.5 Trajectory analysis

We computed approach direction for the average trajectory for each participant on the two conditions (fixed and random-end location). Because averages are strongly affected by outliers, we excluded trajectories that had substantially different temporal characteristics. Note that trajectory data were spatially variable, but timing was consistent for trajectories with similar velocity profile. From the histogram of the time of maximal x-velocities, we selected the trajectories that fell within 80$\%$ the histogram mean (i.e., 10 $\%$-90$\%$ percentiles of the distribution) and averaged them. From the average trajectory, we computed the approach direction of the main axis of the ellipse that describes the spatial variation of the fingers centroids, Fig. 3.5A. The approach direction was computed as the direction of the principal axis of the covariance ellipse that describes the spatial variation of the sensor centroids across both trajectories and time points from the contact time through the preceding

100 ms (10 time steps). This 100 ms time period was selected because it corresponds to the average duration for closing the fingers (kinematically identified as the period in which the x-velocity is near zero and the y-velocity indicates the fingers are moving toward each other). Bootstrap resampling was used to estimate the mean and the standard error of the approach direction for each participant and covariance orientation. The mean and the standard error of the approach direction were computed from 100 bootstrap resamples. Because contact times were difficult to automatically detect from kinematic data, all candidate contact times were cross-checked both by visual inspection and by verifying that the index finger x- and y-velocity were near-zero and the distance of the finger to the cylinder was consistent with contact.

In addition, we measured MGA, because it serves as a measure of position uncertainty [13] and changes with viewing eccentricity [55, 102] and without vision [13]. In particular, fingers are opened wider for grasping objects without precise information about their position, most likely to avoid finger-object collision or missing the objects. On each block of the experiment, we computed the average MGA by measuring the maximum distance between the centroid of sensors on the index finger and the thumb for every trajectory and averaging these values across the 100 trajectories. Note that this distance is 4.5 cm larger than between the contact surfaces of the index finger and thumb, due to the widths of the fingers and the 1 cm thick foam blocks the sensors were mounted on.

3.5.6 Calibration of finger contact surfaces

To evaluate object-finger contact, we computed an estimate of the index finger and thumb contact surfaces relative to the sensor locations via a calibration procedure. The index finger and thumb were placed in grooves on a calibration block and the sensor locations were recorded. The orientation and position of the calibration block were also recorded by placing sensors in known locations on the calibration block. The groove angle, length and depth were precisely known due to the geometry of the block and the block required precision grip contacts similar to those made on the cylindrical object. We converted this information to approximate the index finger and thumb contact surfaces and computed a homogeneous transformation that converted between sensor and finger coordinates. In particular, finger coordinates had an origin at the center of the estimated region of potential

contact, and had directions aligned so that one axis (the surface normal) was perpendicular to the calibration block surface (and hence index finger and thumb normals were parallel but opposite in direction), one axis pointed in the direction of the groove (along the length of the index finger and thumb), and the other axis roughly corresponded to finger width. Once projected into the x-y plane the surface approximation became a line segment that has a 1-2 mm error from the actual index finger/thumb contact surface.

3.5.7 Evaluation of human strategies for grasping objects with directional position uncertainty

According to an optimal statistical modeling approach, the goal is to select a visuomotor grasping strategy that chooses a desired movement trajectory by optimizing the expected gain. The gain function takes into account the costs and benefits of possible outcomes of the movement [80]. Although there are multiple factors that affect grasping as described in the discussion, we focus on the gain provided by achieving force-closure at first contact. We use "optimal strategy" to refer to a grasping strategy that maximizes the probability of satisfying force-closure without post-contact adjustments. Selecting the optimal strategy can be described as an optimization problem as follows, where uppercase refers to random variables and lower case to instances.

The optimal movement policy $\bar{s}^*$ maximizes Eq. (3.1)

$$\bar{s}^* = \arg\max_{\bar{s}} \left\{ G(\bar{s}) = \int_s \int_c R(c,s) P(c) p(s|\bar{s}) ds dc \right\} \tag{3.1}$$

where S is a random variable denoting an executed movement strategy, $\bar{S}$ are reach plans, C represents cylinder locations, $P(c)$ is the distribution of cylinder locations, $R(c,s)$ is an indicator function for the event of successful cylinder contact satisfying force-closure conditions given that the actual movement trajectory is s. The conditional distribution $p(s|\bar{s})$ is the probability of performing the actual movement trajectory s given that the planned movement trajectory is $\bar{s}$. Finally,

$G(s)$ corresponds to the probability that force-closure conditions are satisfied following the movement trajectory s. In the appendix A, we show how to solve Eq. (3.1) to find the optimal strategy.

To keep the analysis tractable, we made the following simplifications. Due to the shapes of both cylinder and fingers, and the post-contact lift direction of the cylinder, we can safely neglect the spatial dimension along the cylinder's z-axis and focus on the perpendicular plane. Within the plane, the contact surfaces of the index finger and thumb can be approximated as line segments (see lower inset of Fig. 3.1). The index finger's contact surface is parameterized by the line segment's midpoint $\mathbf{r}_f$, directions $\mathbf{u}_f$ parallel and $\mathbf{u}_f^{\perp}$ to the surface, and a half-width ϵ. The thumb's contact surface is parameterized similarly, but with subscripts th. With this representation, a reach plan is a desired trajectory $S(t) = \{\mathbf{r}_f, \mathbf{r}_{th}, \mathbf{u}_f, \mathbf{u}_{th}\}$, where time dependence is suppressed inside the brackets to make the notation less complex.

Possible locations for the cylinder (with radius ρ) centroid is modeled as a random vector $\mathbf{c}_i$ sampled from a 2D Gaussian density $P(c)$. To simplify the conditions for contact, we project the samples $\mathbf{c}_i$ into a frame of reference defined by the index finger's (or thumb's) contact surface, forming *contact coordinates*. Contact coordinates are simply the position of points in the environment with respect to the index finger and thumb surfaces. Let $\mathbf{U}_f = \left[\mathbf{u}_f \mathbf{u}_f^{\perp}\right]$, then the contact coordinates for the cylinder with respect to the index finger are given by Eq. (3.2).

$$\begin{bmatrix} w_f \\ d_f \end{bmatrix} = \mathbf{U}_f^T \left(c_i - r_i\right) \tag{3.2}$$

Contact coordinates for cylinder with respect to the thumb are similarly defined. The analysis of optimal grasping is presented in lower inset of Fig. 3.1.

The force-closure indicator function $R(C, S)$, is based on the following necessary conditions for object-finger contacts to be in force-closure:

1. The index finger and thumb are touching the cylinder on the appropriate sides: $d_f = \rho$ and $d_{th} = \rho$.

2. The contact point is within the width of the index finger or thumb: $|w_f| \leq \epsilon$, $|w_{th}| \leq \epsilon$

3. Nguyen [165] showed that a necessary condition for force-closure requires the index finger and thumb contacts to be at surface locations that are within each other's friction cones and include the center of mass (see upper inset of Fig. 3.1). For a coefficient of static friction μ and given $\mathbf{A} = \mathbf{c} + \rho \mathbf{u}_{th}^{\perp}$ and $\mathbf{B} = \mathbf{c} + \rho \mathbf{u}_{f}^{\perp}$ are the contact points of the thumb and index finger respectively, the necessary conditions for force-closure are:

$$\gamma_1 = \left(\mu \mathbf{u}_{th}^{\perp} + \mathbf{u}_{th}\right)^T D_{AB} \leq 0 \tag{3.3}$$

$$\gamma_2 = \left(\mu \mathbf{u}_{th}^{\perp} - \mathbf{u}_{th}\right)^T D_{AB} \leq 0 \tag{3.4}$$

$$\gamma_3 = -\left(\mu \mathbf{u}_{f}^{\perp} + \mathbf{u}_{f}\right)^T D_{AB} \leq 0 \tag{3.5}$$

$$\gamma_4 = -\left(\mu \mathbf{u}_{f}^{\perp} - \mathbf{u}_{f}\right)^T D_{AB} \leq 0 \tag{3.6}$$

where $D_{AB} = \rho \left(\mathbf{u}_{f}^{\perp} - \mathbf{u}_{th}^{\perp}\right)$

Due to the cylinder geometry, the 4 conditions above are equivalent to the simplified condition, Eq. (3.7) that the angle between the surface normals is greater than 90°, for a coefficient of friction μ = 1 (reasonable for skin-plastic contact):

$$\left(\mathbf{u}_{th}^{\perp}\right)^T \mathbf{u}_{f}^{\perp} \leq 0 \tag{3.7}$$

Hence, the indicator function $F = R(C, S)$ is given by Eq. (3.8)

$$F = H\left(-\left(\mathbf{u}_{th}^{\perp}\right)^T \mathbf{u}_{f}^{\perp}\right) H\left(|w_f| - \epsilon\right) H\left(|w_{th}| - \epsilon\right) \delta\left(d_f - \rho\right) \delta\left(d_{th} - \rho\right) \tag{3.8}$$

Where H and δ denote Heaviside step function and the Delta Dirac, respectively (see the appendix A for more details).

To compare human performance to optimal, we estimated the probability of force-closure from trajectory data. For each participant and condition, we treated the set of trajectories as samples from $p(s|\bar{s})$, the distribution of trajectories given the participant's strategy in that condition. To

estimate $G(\bar{s})$, we also computed the expected probability of force-closure for each trajectory and then averaged across trajectories, which can be considered a kind of Monte Carlo integration.

We estimated the expected probability of force-closure $\int_c R(c,s)P(c)dc$ associated with an observed trajectory by measuring the proportion of sampled cylinders that could have been contacted by the fingers along the trajectory and that would have satisfied the conditions for force-closure, had the cylinder been at one of these sampled locations. For each movement trajectory in a random-end location condition with a specific covariance angle, we generated M (where M = 1000) virtual "cylinder positions" drawn from a $P(c)$ with mean and covariance equal to those used in the random-end location condition block of the experiment. The main difficulty in computing this estimate was that either the index finger or thumb was stopping when it made contact with the actual cylinder before sweeping through all sampled cylinder locations. After one of the fingers made contact, the remaining trajectory was biased by the knowledge of the actual cylinder location, and thus should not be used to estimate the probability of force-closure given the reach plan. However, evaluating the conditions for force-closure requires both fingers to contact the cylinder. To overcome this problem, we took advantage of the fact that trajectories were near-linear and had low-variability close to the center of the cylinder distribution. Thus, we assumed that the remaining trajectory of the non-contacting finger can be replaced by extrapolating in the direction of average trajectory (across all trials) for that finger at the contact time, until the extrapolation either contacted or missed the cylinder. Because the proportion of locations intersected was affected by this collision, we normalized the counts by the number of cylinders that the ideal strategy would successfully grasp if the index finger and thumb were stopped at the same locations. This computation is illustrated for two different trajectories in Figs. 3.6A, and 3.6B, respectively.

We tested the optimality of participants' grasp strategies and to provide a comparison, we also estimated the deterioration in grasping performance if participants do not compensate for uncertainty. To provide a baseline comparison for this grasp performance measure, we estimated the probability of force-closure if participants had adopted a non-compensation strategy for the random-end location condition (and hence would not have compensated for the cylinder location uncertainty). We simulated the non-compensation strategy by estimating the expected probability of force-closure

for no-motion condition trajectories on the “random-end location condition” cylinder locations.

Chapter 4

An optimal feedback control framework for grasping objects with position uncertainty

4.1 Overview

As we move, the relative location between our hands and objects changes in uncertain ways, due to noisy motor commands and imprecise and ambiguous sensory information. The impressive capabilities humans display for interacting and manipulating objects with position uncertainty suggest that our brain maintains representations of location uncertainty and builds compensation for uncertainty into its motor control strategies. Our previous work demonstrated specific control strategies are used to compensate for location uncertainty. However, it is an open question whether compensation for position uncertainty in grasping is consistent with the stochastic optimal feedback control, mainly due to the difficulty of modeling natural tasks within this framework. In the current study, we develop a stochastic optimal feedback control model to evaluate the optimality of human grasping strategies. We investigate the properties of the model through a series of simulation experiments and show that it explains key aspects of previously observed compensation strategies. It also provides a basis for individual differences in terms of differential control costs - the controller only

compensates to the extent that performance benefits in terms of making stable grasps outweigh the additional control costs of compensation. These results suggest that stochastic optimal feedback control can be used to understand uncertainty compensation in complex natural tasks like grasping.

4.2 Introduction

A preponderance of the studies in human motor control focuses on goal-directed movements, where the goal can be expressed as a desired configuration of the body. The optimal feedback control framework has proven quite successful at modeling goal-directed movements, such as reaching to touch targets and pointing to directions. According to this theory, optimal movement strategies are generated by optimizing performance criteria that include both goal-related costs and action costs [49–52, 74, 132, 134, 152]. The success of optimal feedback control theory stems in part from its ability to model probabilistic information that the sensorimotor system incorporates into motor strategies in goal-directed movements, including uncertainty about world states, body configurations, and noise in sensory inputs and motor commands [31, 50, 51, 85, 127].

However, the goal-directed movements described above do not capture many characteristics of the majority of every day movements, which are complex and purposive movements that involve the application of forces to an object, with the intent of changing either the object's motion (as in grasping), or one's own motion (as in walking). Planning for such movements requires anticipating the effects of object-body contact on subsequent dynamics. Due to the complexity of anticipating the effects of applied forces to an object's motion, it is significantly more challenging to model complex purposive movements within the optimal feedback control framework, especially when the target position can vary unpredictably. While there are few studies that model purposive movements, such as grasping [63], walking [57, 148], jumping [56, 118] and snowboarding/surfing [72], within the optimal feedback control framework, they do not consider uncertainty in the task goal.

In the current study, we propose an optimal control framework to model uncertainty compensation strategies in grasping. The goal of the optimal controller is to generate strategies that produce a stable grasp at the first contact, avoiding colliding with or missing a cylindrical object; this goal can be formally defined through suitable cost functions. Discovering appropriate cost functions that

characterize human behavior in natural tasks constitutes a critical step in formalizing theories of motor control. Moreover, optimality analyses are determined by three components; the controlled system dynamics, the observability of the system, and what cost functions are being optimized. Modeling motor control strategies for goal-directed movements as optimal solutions to cost functions has a long history, including control-related costs like energy consumption [57, 170] or their kinematic proxies - derivative of hand [156] and derivative of joint torque [176], and performance based criteria like end-point variability [31]. For complex and purposive movement tasks, the difficulty is not capturing control costs; rather the difficulty is in expressing the more complex task goals via cost functions. We developed cost functions that capture the key requirements of an agent that needs to rapidly grasp and manipulate objects with low tolerance for error. These criteria encourage movement plans that produce stable grasps at first-contact, while avoiding colliding with or missing the object, as illustrated in Fig. 4.1A. To keep the analysis as simple as possible, we modeled the human hand as a 2-dimensional, 1-link planar gripper with 2 rotational degrees of freedom (d-o-f) assuming that only the index finger is movable, Fig. 4.2.

We ran a number of simulations to validate the proposed model and found that many aspects of human compensation for grasping objects with position uncertainty can be explained by the optimal control model, including individual differences. We show that the controller compensates for object-position uncertainty by modifying the grip aperture profile and approaching the cylinder along the direction of maximal position uncertainty. Importantly, the controller compensates for uncertainty only when the benefits from compensation in terms of the successful grasp outweigh the control costs. In addition, individual differences observed between participants in grasping strategies under position uncertainty could be explained due to variation of control costs, such as wrist rotation and "open-close" of the fingers. To the best of our knowledge, this is the first optimal control study that interprets experimental data from complex purposive tasks with target location uncertainty.

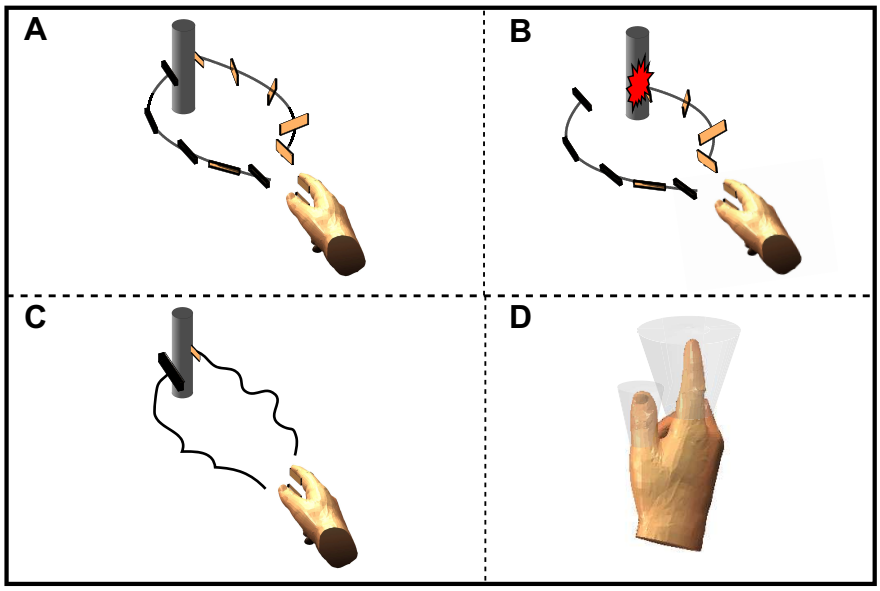

Figure 4.1: **A**: Illustration of a typical trajectory that satisfies the goal criteria and produces a stable grasp at first contact. **B**: The controller takes into account the task constraints and produces efficient trajectories so that the gripper does not collide with or miss the cylinder. **C**: Illustration of a hypothetical trajectory with high control costs.. **D**: Gray cones represent the areas that fingers are able to move due to biomechanical structure of them.

4.3 MATERIALS AND METHODS

4.3.1 Optimal control for grasping objects

Hand Modeling

To preserve interpretability, it is important to use a model no more complex than absolutely necessary. To achieve this simplicity, the majority of previous studies model the human hand as a "point of mass" [50, 51] or as a "n-link planar device" with linear dynamics and kinematics [63, 156, 176]. In the current study, we modeled the human hand as a 2-dimensional 1-link planar device with 2 rotational degrees of freedom (d-o-f), in which only the index finger is movable, Fig. 4.2.

Let $\mathbf{p}^h = [x_h(t),\ y_h(t)]^T$, $\theta(t)$ and $gw(t)$ denote the midpoint of the wrist, the orientation and the gripwidth of the planar gripper, respectively at a given time t. Assuming that the target position, is on $\mathbf{p}^c = [x_c(t),\ y_c(t)]^T$, the discrete-time state is described through an 11-dimensional vector $\mathbf{x}_t$, Eq. (4.1)

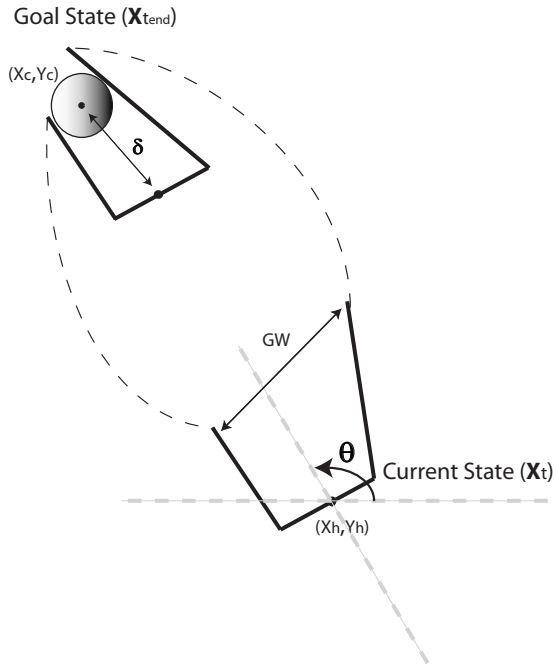

Figure 4.2: Graphical representation of the current $\mathbf{x}_t$ and goal $\mathbf{x}_{t_{end}}$ state for the 1-link planar gripper with 2 rotational d-o-f, which was used in this study to model the human hand.

$$\mathbf{x}_t = \Big[x_h(t),\ y_h(t),\ \dot{x}_h(t),\ \dot{y}_h(t),\ \theta(t),\ gw(t),\ \dot{\theta}(t),\ \dot{gw}(t), x_c(t), y_c(t),\ 1\Big]^T \tag{4.1}$$

The gripwidth variable $gw(t)$ is not directly observable, but it can be estimated by the angular position of the movable finger $\phi(t)$ in Eq. (4.2)

$$gw(t) \simeq L_{mv}\left(\phi(t) - \phi^0\right) \tag{4.2}$$

where L_{mv} is the length of the movable finger and ϕ^0 is the minimum value of ϕ when gw is zero, meaning both fingers are in contact.

Finally, we assume that the gripper controls the translational $\ddot{\mathbf{p}}^h = [\ddot{x}_h(t),\ \ddot{y}_h(t)]^T$ and angular acceleration $\ddot{\theta}(t)$, as well as the acceleration of opening and closing the fingers, $\ddot{gw}(t)$, Eq. (4.3).

$$\mathbf{u}_t = \left[\ddot{x}_h(t);\ \ddot{y}_h(t);\ \ddot{\theta}(t);\ g\ddot{w}(t)\right]^T \tag{4.3}$$

4.3.2 Optimal control

Previous studies have shown that control policies in goal-directed movements can be modeled by the optimization of cost functions that mix a measure of expected loss (or reward) with a measure of motor costs [132]. Let $\mathbf{x}_t$ denote a vector that describes the state of a biological system (e.g., hand) and the environment, and $\mathbf{u}_t$ represent a vector of the motor commands at a certain time *t*. Given the system's controlled dynamics and sensory and motor noise, the stochastic optimal feedback control finds a sequence of motor commands that optimizes the cost function described in Eq. (4.4),

$$J\left(\mathbf{x}_{[t_1,t_{end}]}, \mathbf{u}_{[t_1,t_{end}]}\right) = E\left(\mathbf{x}_{t_{end}}^T Q_{t_{end}} \mathbf{x}_{t_{end}} + \sum_{k=t_1}^{t_{end}-1} \left(\mathbf{x}_k^T Q_k \mathbf{x}_k + \mathbf{u}_k^T R \mathbf{u}_k\right)\right) \tag{4.4}$$

where Q_k and R are matrices that weight the two costs associated with the expected loss and the motor commands, respectively.

To overcome feedback instabilities due to noisy sensors and temporal delays, the sensorimotor system uses internal forward models to predict the next state of the system at time $t+1$, $\hat{\mathbf{x}}_{t+1|t}$ based on the expected sensory feedback $\hat{\mathbf{y}}_t$, the current state estimate $\hat{\mathbf{x}}_t$ and control commands $\mathbf{u}_t$, [74]. We modeled the hand and state space to enable the use of linear dynamics and measurement equations for the forward model (4.5).

$$\begin{aligned} \hat{\mathbf{x}}_{t+1|t} &= \hat{A}\hat{\mathbf{x}}_t + \hat{B}\mathbf{u}_t \\ \hat{\mathbf{y}}_t &= \hat{C}\hat{\mathbf{x}}_t \end{aligned} \tag{4.5}$$

where $\hat{A}$, $\hat{B}$ and $\hat{C}$ correspond to the estimated system dynamics and observation matrices, respectively.

The actual dynamics of the system are given by Eq. (4.6), considering that both control commands and state variables are corrupted by multiplicative noise, which are normally distributed with zero mean and a standard deviation proportional to the magnitude of the control commands and state variables.

$$\begin{aligned} \mathbf{x}_{t+1} &= A\mathbf{x}_t + B\mathbf{u}_t + \xi_t + C(\mathbf{u}_t)\epsilon_t \\ \mathbf{y}_t &= H\mathbf{x}_t + \omega_t + D(\mathbf{x}_t)\epsilon_t \end{aligned} \tag{4.6}$$

where A, B and H are the actual system dynamics and observation matrices, respectively. In addition, $C(\mathbf{u}_t)$ and $D(\mathbf{x}_t)$ are matrices for the control-dependent and state-dependent noise. Finally, ξ_t, ω_t and ϵ_t are normally distributed variables with zero mean and covariances $\Omega^{\xi} \geq 0$, $\Omega^{\omega} \geq 0$ and $\Omega^{\epsilon} = I$, respectively.

The actual sensory feedback $\mathbf{y}_t$ is combined with the expected sensory feedback $\hat{\mathbf{y}}_t$ via Eq. (4.7) to update the estimate about the state of the system and the environment.

$$\hat{\mathbf{x}}_{t+1|t+1} = (A - BL_t)\hat{\mathbf{x}}_{t+1|t} + K_t\left(\mathbf{y}_t - H\hat{\mathbf{x}}_{t+1|t}\right) + n_t \tag{4.7}$$

where the matrices L_t and K_t define the optimal control law and the Kalman gain, respectively, at any given time t. The internal noise n_t has zero mean and covariance $\Omega^n \geq 0$ and is added to the estimator to account for the multiplicative noise, which affects the predictions and consequently the control law. We compute L_t and K_t using methods described in [50].

Based on the current state estimate and the goal of the task, the controller generates these motor commands u_t^* that optimize the expected cost function in Eq. (4.4). This is a modified form of the Linear Quadratic Gaussian (LQG) regulator in optimal control, in which the system dynamics are linear, the cost function is quadratic and the noise is Gaussian [50], but with signal dependent noises. However, the cost function which captures the grasping problem is not quadratic - it is a complex nonlinear function of the state variables. To generate control commands, we iteratively

re-approximate this cost by a quadratic function at each time step, as described below.

Optimal control cost function in a grasping task

Classical optimal control studies fail to model natural movement tasks, mainly because they ignore potential constraints of the movements. Natural tasks frequently generate conflicting requirements between safety and success. For instance, in attempting to grasp an object in the midst of obstacles, optimal planning should provide both a stable grasp and robustness against failure - knocking over or missing the object. For that purpose, we built a mixture of "grasp-dependent" performance criteria incorporating also collision avoidance constraint in the cost function, which ensures that gripper neither collides with nor misses the object.

We model the goal of grasping objects as a cost function that decomposes into terms mainly associated with the task goal F_g, the constraints of the task F_c, the biomechanical constraints of the hand F_b, and the energy consumption constraints F_e. A generic form of the optimal control cost function is given by Eq. (4.8).

$$J\left(\mathbf{x}_{[t_1,t_{end}]}, \mathbf{u}_{[t_1,t_{end}]}\right) = F_g(t_{end}) + \sum_{t=t_1}^{t_{end}} F_c(t) + \sum_{t=t_1}^{t_{end}} F_e(t) + \sum_{t=t_1}^{t_{end}} F_b(t) \tag{4.8}$$

The first term in Eq. (4.8) describes the goal of the task - movements that produce stable grasps at first contact similar to the one presented in Fig. 4.1A. This term is a function of 4 individual criteria $F_g(t_{end}) = \sum_1^4 f_i(t_{end})$, which are all evaluated at the end of the movement trajectory t_{end}. Given the geometric characteristics of the cylinder, the necessary conditions for a stable grasp are the following:

1. The cylinder is between the fingers.
2. The finger-object contacts are within the width of the fingers.
3. The fingers contact the cylinder on the appropriate sides: $d_{st} = \rho$ and $d_{mv} = \rho$
4. Both fingers contact the cylinder with zero velocity.

where ρ describes the radius of the cylinder, and d_{st} and d_{mv} are the distances between the center of the cylinder to the tip of the stationary and movable finger, respectively.

The 1^{st} condition can be expressed mathematically through the cost term f_1, which penalizes actions that produce trajectories with the cylinder outside the gripper at t_{end}. Let's denote $\mathbf{p}^h(t_{end})$ as the midpoint of the wrist, and $\mathbf{p}^{mv}(t_{end})$ and $\mathbf{p}^{st}(t_{end})$ the tip of the movable and stationary fingers, respectively. We define f_1 as a sum of 3 Heaviside step functions H, whose values are zero once the cylinder is in the region defined by the fingers and the wrist, Eq. (4.9).

$$f_1(t_{end}) = H(\mathbf{p}^{mv}(t_{end})) + H(\mathbf{p}^{st}(t_{end})) + H(\mathbf{p}^h(t_{end})) \tag{4.9}$$

The 2^{nd} condition encourages positional accuracy of the gripper at the end of the trajectory. We can express this condition mathematically by computing the Euclidean distance between the midpoint of the wrist $\mathbf{p}^h(t_{end})$ and the center of the cylinder position $\mathbf{p}^c(t_{end})$. This distance should be less that a predefined threshold $\delta > 0$. To simplify the calculations, we expressed $f_2(t_{end})$ as the difference between the square of the Euclidean distance and δ^2, Eq. (4.10).

$$f_2(t_{end}) = \left(||\mathbf{p}^h(t_{end}) - \mathbf{p}^c(t_{end})||_2^2 - \delta^2 \right)^2 \tag{4.10}$$

The 3^{rd} condition insures that the gripper will close the fingers and grasp the cylinder at the end of the trajectory. Consequently, the gripwidth gw should be equal to the diameter of the cylinder at t_{end}, Eq. (4.11).

$$f_3(t_{end}) = (gw(t_{end}) - 2\rho)^2 \tag{4.11}$$

Finally, we introduce a cost term f_4 that enforces that the gripper contacts the cylinder with zero velocity, Eq. (4.12).

$$f_4(t_{end}) = \dot{\mathbf{p}}^h(t_{end}) \tag{4.12}$$

Grasping the cylinder successfully requires movement trajectories that avoid collisions with the object before the gripper is closed around it. Because the object position is uncertain, collisions could happen at any point in the trajectory, but are more likely to happen near the estimated location of the object (e.g., Fig. 4.1B). To make sure the object is graspable at any point and avoid collisions, the gripper needs to be oriented such that the position of the object falls within the span between the two fingers at each point of the trajectory. $F_c(t)$ incorporates such a collision avoidance constraint using a cost similar to f_1, except that it is weighted with a scalar factor w_c and is evaluated at each time step across the movement trajectory Eq. (4.13).

$$F_c(k) = w_c \Big(H(\mathbf{p}^{mv}(k)) + H(\mathbf{p}^{st}(k)) + H(\mathbf{p}^h(k)) \Big) \tag{4.13}$$

The third part of the cost function in Eq. (4.8) is related to minimizing control, Eq. (4.14).

$$F_e(k) = \mathbf{u}(k)^T R \mathbf{u}(k) \tag{4.14}$$

where $R > 0$ is a scale factor of the energy-like cost function. The purpose of this criterion is to penalize actions (i.e., motor commands) of large magnitude, similar to one illustrated in Fig. 4.1C.

Finally, in biological systems some actions cannot be achieved due to biomechanical constraints. Particularly, both thumb and index finger are able to move around specific regions as shown in Fig. 4.1D. Hence, the last term in Eq. (4.8) prohibits actions at any time t that cannot be achieved by the gripper due to the biomechanical constraints. However, in this study, we chose to exclude this factor from the optimal control analysis because the relevant biomechanical constraints are hard to model and vary between participants.

Each of these costs is defined in terms of a known cylinder position. To model the effects of object location uncertainty, we take the expectation of this cost function with respect to a distribution representing the set of possible object locations. To model the experimental data, we assume object location uncertainty takes the form of a 2D Gaussian distribution $N \sim (\bar{\mathbf{p}}^c, \Sigma^c)$. Therefore, the optimal policy is given by minimizing the *expected* cost function of Eq. (4.8) with respect to the cylinder position distribution, $E_{\bar{\mathbf{p}}^c,\Sigma^c}\{J\left(\mathbf{x}_{[t_1,t_{end}]}, \mathbf{u}_{[t_1,t_{end}]}\right)\}$. This expectation can be computed analytically, and the resulting expected cost function can be expressed in terms of the mean and covariance of the cylinder position distribution (see Appendix B).

Approximating the cost function

The signal-dependent Linear Quadratic Gaussian (LQG) framework is not directly applicable, because the expected cost function is not quadratic. Particularly, the expected values of f_1, f_2 are not quadratic with respect to the state variables. Nevertheless, we can generate high quality approximations of the solution to these cost functions using iterative quadratic approximation. That is, we approximated the expected values of f_1 and f_2 with a 2^{nd}-order Taylor series approximation around their minimum. Because the expected value of f_1 is a highly non-linear function of the gripper position $\mathbf{p}^h(t)$, orientation $\theta(t)$ and gripwidth $gw(t)$, it was critical to this approximation to find the minimum of the cost function with respect to the state of the gripper. Traditional optimization techniques that are based on gradient methods have a great risk of being trapped at local optimal solutions for complex and non linear cost functions. For this reason, we used Evolutionary Algorithms (EAs) to find a global solution $(\mathbf{p}_0^h, \theta_0, gw_0)$ that minimizes $E_{\bar{\mathbf{p}}^c,\Sigma^c}\{f_1(t_{end})\}$ [39]. In contrast, the expected value of f_2 is a 4^{th}-order polynomial with respect to the gripper position $\mathbf{p}^h(t)$ and has an analytic solution for its minimum.

We constructed quadratic approximations for both the expected values of f_1 and f_2 at each step of the reaching trajectory. For any given position of the wrist with respect to the mean position of the cylinder, we built a quadratic approximation of the expected f_1 as a function of the gripper orientation and the gripwidth variables. This approximation must be recomputed for each position of the gripper. To accomplish this, we minimized the expected f_1 with respect to the gripper orientation

and gripwidth, and recomputed the Taylor series approximation around this minimum. The optimal control policy is recalculated from the current state $\mathbf{x}_t$ at every 5 time-steps until the gripper is with 5 cm of the cylinder. The quadratic approximation of the expected f_2 is handled in a similar way.

In the following, we demonstrate how the methodology described above can be used to identify optimal strategies to grasp objects with directional position uncertainty. The simulations are meant to model the experimental conditions of the human study presented in Chapter 3. The distance between the mean position of the cylinder and the initial position of the gripper is 50 cm (i.e., cylinder mean position (50 cm, 50 cm), gripper initial position (80 cm, 10 cm)) and the initial gripper orientation is 90 deg. In addition, the cylinder position is generated by a Gaussian distribution with

$$N \sim \left(\begin{bmatrix} 50 \\ 50 \end{bmatrix}, \mathbf{V} \begin{bmatrix} 12 & 0 \\ 0 & 0.25 \end{bmatrix} \mathbf{V}^T \right), \text{where } \mathbf{V} = \begin{bmatrix} \cos(\alpha) & -\sin(\alpha) \\ \sin(\alpha) & \cos(\alpha) \end{bmatrix}$$

where α corresponds to the orientation of the cylinder position distribution. The controller is assumed to know the mean and covariance of this distribution, but not the actual object location.

Note that the standard deviation of the major and minor axes of the cylinder position distribution is one order of magnitude larger than the those used in the human study presented in Chapter 3. The reason is that low standard deviation values result in poor quadratic approximations of the expected f_1 and f_2.

The discrete-time motion equation for the gripper is given by Eq. (4.15):

$$\mathbf{p}^h(t_k + \delta t) = \mathbf{p}^h(t_k) + \delta t\, \dot{\mathbf{p}}^h(t_k) + n_t + \sum_{i=1}^{4} \epsilon_t^i C_i \mathbf{u}_t \tag{4.15}$$

where $\delta t = 0.01$ s is the sampling period of the discretization.

The sensory feedback y_t carries information about the state variables of the system (i.e., position, velocity, orientation and gripwidth) corrupted by two independent sources of Normal distributed noise - one with standard deviation proportional to the magnitude of the state variables $\sum_{i=1}^{11} \epsilon_t^i D_i \mathbf{x}_t$, and one with constant standard deviation ω_t.

Both the discrete-time motion equation and the sensory feedback equation can be transformed into the form of Eq. (4.6) with the following matrices:

$$A = \begin{bmatrix} 1 & 0 & \delta t & 0 & 0 & 0 & 0 & 0 & 0 & 0 & 0 \\ 0 & 1 & 0 & \delta t & 0 & 0 & 0 & 0 & 0 & 0 & 0 \\ 0 & 0 & 1 & 0 & 0 & 0 & 0 & 0 & 0 & 0 & 0 \\ 0 & 0 & 0 & 1 & 0 & 0 & 0 & 0 & 0 & 0 & 0 \\ 0 & 0 & 0 & 0 & 1 & 0 & \delta t & 0 & 0 & 0 & 0 \\ 0 & 0 & 0 & 0 & 0 & 1 & 0 & \delta t & 0 & 0 & 0 \\ 0 & 0 & 0 & 0 & 0 & 0 & 1 & 0 & 0 & 0 & 0 \\ 0 & 0 & 0 & 0 & 0 & 0 & 0 & 1 & 0 & 0 & 0 \\ 0 & 0 & 0 & 0 & 0 & 0 & 0 & 0 & 1 & 0 & 0 \\ 0 & 0 & 0 & 0 & 0 & 0 & 0 & 0 & 0 & 1 & 0 \\ 0 & 0 & 0 & 0 & 0 & 0 & 0 & 0 & 0 & 0 & 1 \end{bmatrix}, \quad B = \begin{bmatrix} 0 & 0 & 0 & 0 \\ 0 & 0 & 0 & 0 \\ \delta t & 0 & 0 & 0 \\ 0 & \delta t & 0 & 0 \\ 0 & 0 & 0 & 0 \\ 0 & 0 & 0 & 0 \\ 0 & 0 & \delta t & 0 \\ 0 & 0 & 0 & \delta t \\ 0 & 0 & 0 & 0 \\ 0 & 0 & 0 & 0 \\ 0 & 0 & 0 & 0 \end{bmatrix}, H = [\mathbf{I}_{8\times 8} \mid \mathbf{0}_{8\times 3}] \quad (4.16)$$

The observation matrix H consists of a 8×8 unitary matrix, and a 8×3 zero matrix, because the system is not fully observable - the actual cylinder position is not known at any given time t.

The control-dependent cost is defined through the matrix $R = \frac{1}{t_{end}}\{diag\,[r_{ii}]\}_{4\times 4}$, where r_{ii}'s are the control costs of the gripper motion in x and y direction, rotation and "open-close" the fingers, respectively. Additionally, the time-varying matrix $Q(t) = [q_{ij}]_{11\times 11}$ describes the state-dependent cost and is given by Eq. (4.17).

$$Q(t) = \begin{cases} Hf_1\left(\vec{s_1}^*\right), & t < t_{end} \\ Hf_1\left(\vec{s_1}^*\right) + Hf_2\left(\vec{s_2}^*\right) + Hf_3 + Hf_4, & t = t_{end} \end{cases} \quad (4.17)$$

where $Hf_1\left(\vec{s_1}^*\right)$ and $Hf_2\left(\vec{s_2}^*\right)$ are the Hessian matrice of the quadratic approximations of f_1 and f_2, respectively, evaluated at their minimum $\vec{s_1}^*$ and $\vec{s_2}^*$. Also, Hf_3 and Hf_4 are the Hessian matrices of the quadratic cost terms f_3 and f_4, respectively.

The scaling matrices for the control-dependent system noise and state-dependent system observation noise are $C = B \times \sigma_c$; $\sigma_c = 0.5$ and $D = diag\,[d_{ij}]_{8\times 8}$; $d_{ij} = 10^{-5}$ describes the individual noise in each of the observed state variables. Note that σ_c and d_{ij} are unitless variables defined as the noise magnitude relative to the control and state signal magnitude, respectively [50].

4.4 Results

We focus the analysis of model trajectories on measures that vary across uncertainty conditions, such as maximum grip aperture (MGA) and approach direction of the gripper. MGA is an important behavioral characteristic because it serves as a measure of position uncertainty [13, 175] and scales with viewing eccentricity [55, 102]. We estimated the approach direction of the gripper by averaging the gripper orientation from the contact time and the preceding 100 ms. This time interval was selected because it corresponds to the time period used to estimate the approach direction in the human study. Additionally, the duration for grasping the cylinder was $t_{end} = 120$ time steps (1200 ms), because it corresponds to the time that participants had to reach and grasp the cylinder (see Chapter 3 for more details).

4.4.1 The role of collision avoidance constraint in grasping objects with position uncertainty

In the simulations, the gripper started 50 cm away from the cylindrical object. The cylinder position was distributed along a strongly oriented 2D Gaussian distribution with 60° orientation, 12 cm and 0.25 cm standard deviation of major and minor axes, respectively, Fig. 4.3A. In addition, the control-dependent cost was set to $R = \frac{1}{120}\{diag[10^{-5},\, 10^{-5}, 1, 10^{-8}]\}$. Note that in the human study, we found that people preferred an approach direction of about 70°, when the position of the cylinder did not vary unpredictably. We consider this approach direction the "minimum energy cost path" for grasping the cylinder, due to the initial object-finger relative position. We incorporate this energy-like criterion in the model by setting the minimum rotation cost to be 70°.

Figs. 4.3B and 4.3C show the importance of the collision avoidance constraint on grasping objects with position uncertainty. When the collision avoidance constraint cost function is weighted

by $w_c = 2^{-6}$, the fingers open wider almost from the beginning of the trajectory, to avoid colliding with the object.

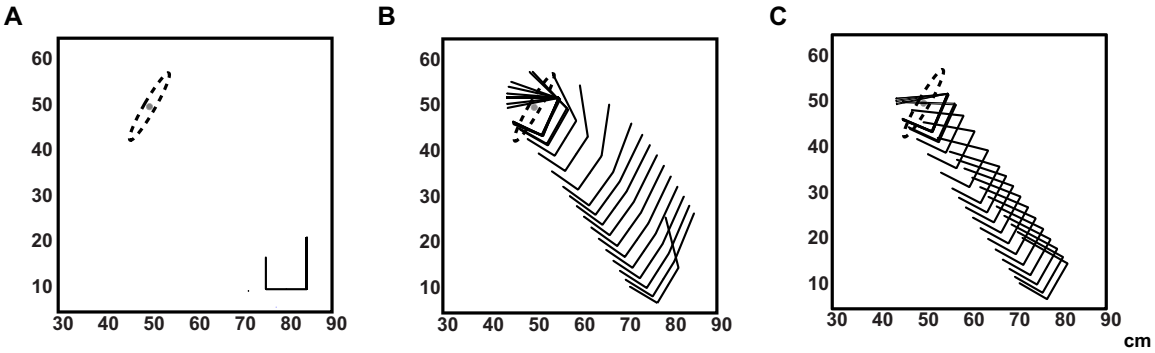

Figure 4.3: **A**: Initial position of the gripper and the cylinder, in a typical simulation of the grasping task with 60° orientation of the cylinder position distribution (discontinuous ellipse). The gray spot denotes the mean position of the cylinder. **B**: If we incorporate the collision avoidance constraint term into the cost function, the fingers open wider to avoid missing or hitting the cylinder. **C**: Otherwise, the grip aperture remains narrow across the reach trajectory increasing the chance for colliding with or missing the cylinder.

To gain insight into the effects of the collision avoidance constraint on optimal strategies, we varied the weight factor (w_c) and measured MGA and approach direction of the gripper for different covariance angles of the cylinder position distribution. We found that MGA scales almost linearly with w_c, Fig. 4.4A, whereas we found no significant variation of approach direction with variation in w_c. In essence, the collision avoidance constraint affects only the grip aperture profile but not the approach direction of the gripper.

4.4.2 Impact of position uncertainty on grasping trajectories

We ran a series of simulations by varying both the size and the orientation of the cylinder position distribution to test the effects of position uncertainty on optimal grasping strategies. The initial configuration of the cylinder-gripper was the same as that shown in Fig. 4.3A, but with different covariance angles of the cylinder position distribution. Fig. 4.5 illustrates simulated optimal trajectories of the gripper for 3 different orientations of the cylinder position distribution (i.e., -20°, 20° and 40°). Notice that the approach direction of the gripper varies with the orientation of the cylinder position distribution.

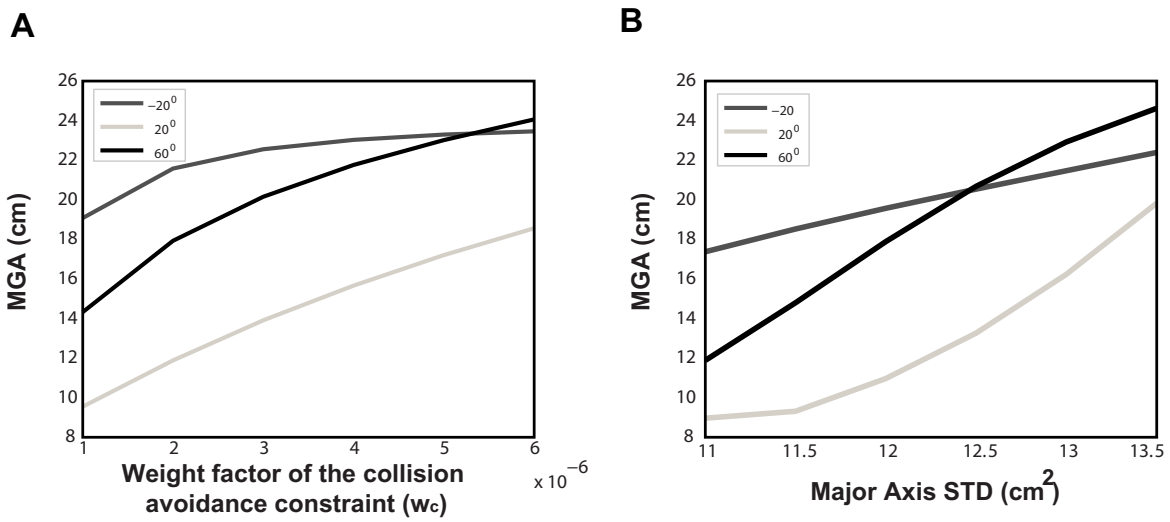

Figure 4.4: **A**: Collision avoidance constraint affects the grip aperture profile. MGA scales almost linearly with the weight factor of the collision avoidance constraint. **B**: MGA scales with the magnitude of the cylinder position uncertainty.

We tested whether the magnitude of position uncertainty affects the optimal grasping policy by varying the standard deviation of the covariance major axis. The results presented in Fig. 4.4B show that MGA scales almost linearly with the size of uncertainty. However, we found no significant variation of MGA time and approach direction with variation of uncertainty size. These results are consistent with experimental findings of grasping objects with position uncertainty due to peripheral vision, in which MGA scales with the size of uncertainty [55, 102].

Furthermore, we tested the effects of the covariance orientation on optimal grasping strategies,

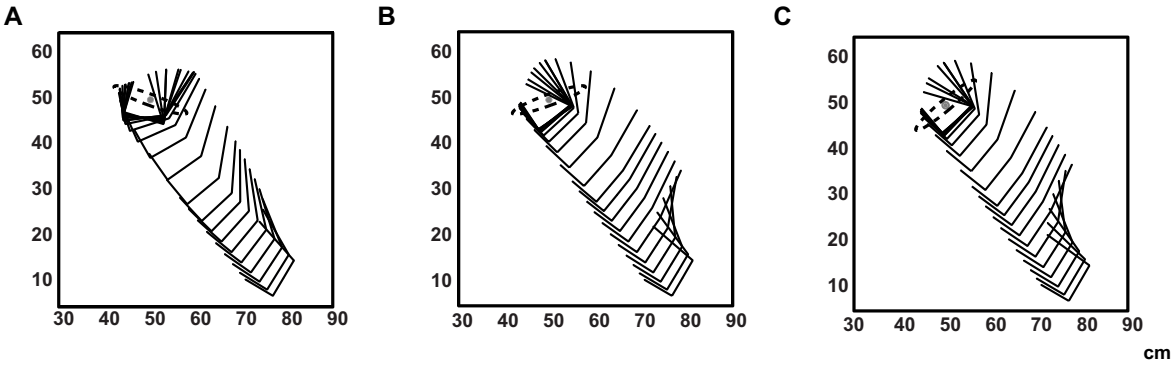

Figure 4.5: Simulated optimal trajectories for grasping the cylindrical object with covariance orientation: **A**: -20° **B**: 20° and **C**: 40°.

by measuring the approach direction and MGA for an 80° range of distribution orientation (i.e., $-20^0, 0^0, 20^0, 40^0$ and 60^0). In accordance with our predictions, we found that approach direction scales almost linearly with the covariance angle for low gripper rotation cost, Fig. 4.6A. In addition, we found no significant variation on MGA and MGA time across the different covariance orientations, consistent with the experimental findings presented in Chapter 3.

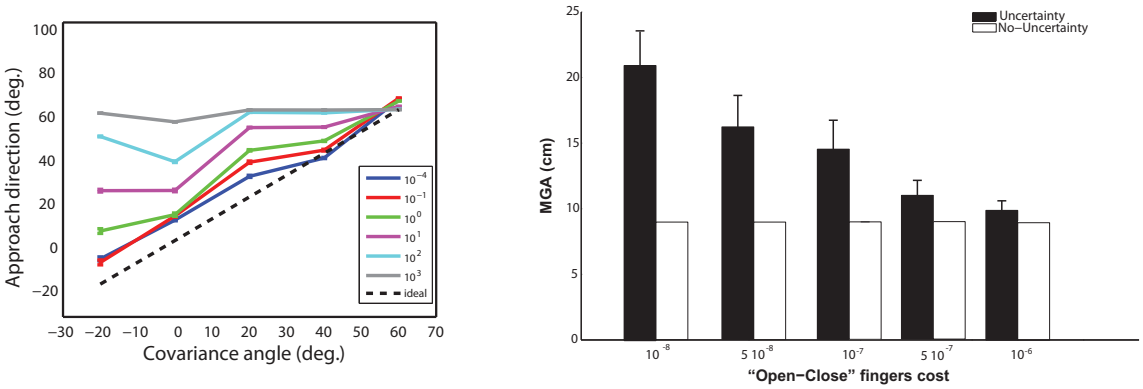

Figure 4.6: **A**: Approach direction vs. covariance orientation for different gripper rotation costs. Error bars are $\pm$ 1 standard error. The black discontinuous lines show ideal compensation. **B**: MGA averaged across covariance angles for different gripper rotation and "open-close" fingers costs.

4.4.3 Impact of control-dependent cost on optimal grasping strategy

There are usually trade-offs between competing criteria in purposive movements. For instance, in grasping tasks, we trade off between reaching the objects in a precise manner, contacting them on the appropriate sides, exerting the necessary forces for stable grasps and consuming the lowest energy. Accordingly, we tested the hypothesis that the controller compensates for object-position uncertainty as long as the costs to rotate the gripper and "open-close" the fingers are not too high.

To test this hypothesis, we ran a series of simulations, in which we varied both the control costs for the gripper rotation r_{33} and "opening-closing" of the fingers r_{44} and measured the approach direction and MGA of the gripper. Fig. 4.6A depicts the approach direction for each covariance angle for a set of different gripper rotation costs (while keeping the "open-close" fingers cost fixed at 10^{-8}). The results show that the approach direction scales with the orientation of cylinder position distribution, as long as the cost for rotating the gripper is low. However, when the cost for gripper

rotation becomes too high, the controller does not compensate anymore.

Varying the gripwidth control cost while keeping the rotation cost constant (i.e., 0.1) changed the MGA but not the grasp orientation. Fig. 4.6B shows the MGA for different "open-close" fingers costs in two conditions: a) no uncertainty and b) uncertainty about the cylinder position (average MGA across the 5 covariance orientations). Notice that the MGA difference between the two conditions increases as the cost for gripwidth control goes down.

On the whole, optimal strategy for grasping objects with position uncertainty involves opening the finger wider and aligning the approach direction of the fingers with the direction of maximal position uncertainty. However, when this strategy becomes too expensive, the controller does not compensate anymore.

4.5 Discussion

We proposed an optimal feedback control framework to model human behavior in purposive movement tasks like grasping when the position of the target is not precisely known. Optimal feedback control theory is considered the most successful framework to model a variety of biological movements, such as point-to-point reaching movements [34, 50, 152], throwing balls to targets [51] and others (for review see [49]). To simplify modeling and the assessment of optimality, these studies have focused on simple goal-directed tasks, which exclude ubiquitous complex purposive movements that involve the application of forces on objects. It is quite challenging to extend the optimal feedback control theory to model purposive movements. There are only few studies that account for human behavior in purposive movement tasks, such as jumping [118], grasping objects [63], walking [57, 148] and snowboarding/surfing [72]. However, none of these studies provide models that can explain human compensation strategies in purposive movement tasks.

One of the novelties of this study is the cost function that we designed to model human behavior for grasping objects with position uncertainty. Rather than hand tune a cost function to match human trajectories or model the full details of object-finger contact, our cost function encodes the minimum requirements needed to accomplish the grasping task. This is interesting because grasping is a complex task, but a simple cost function captures most of human reaching behavior. Much of the

simplicity stems from the fact that grasping has stronger constraints - making stable contacts without object finger collision constrains optimal trajectories. In contrast, goal-directed tasks like pointing or touching are trajectory ambiguous, in that multiple trajectories could satisfy the task constraints. Reducing the trajectory ambiguity requires invoking cost functions that ensure accuracy and energy efficiency, like minimum variance with signal-dependent noise [31].

An interesting question is how the cylinder position uncertainty affects the optimal grasp plan. By varying both the size and the orientation of the cylinder position distribution, we found that uncertainty modulates the optimal grip aperture profile and the approach direction of the gripper. These results are consistent with findings in human studies, where MGA increases as the amount of visual uncertainty of the object position increases [21, 55, 102] and approach direction scales with the orientation of the cylinder position distribution (see Chapter 3).

Optimal strategies for grasping objects with position uncertainty involve a series of actions that require energy consumption. If the only criterion was the reward for grasping the cylinder, then people would reach and grasp the objects as fast as possible, open their fingers as wide as possible and align perfectly the approach direction with the orientation of the cylinder position distribution. However, reaching trajectories display stereotyped movements, which involve an initial forward transport phase that brings the hand near to the object, followed by a period in which digits move slowly and contact the object [86]. Additionally, fingers do not open widely across the whole trajectory and the hand does not align perfectly with the covariance orientation of the cylinder position distribution [168]. These differences from reward-based predictions can be explained by movement constraints and control costs that prevent people from compensating utterly. Optimal control shows that the benefits of compensation in terms of the probability of stably grasping must outweigh the action costs. These effects of control costs on compensation strategies may explain the individual differences observed among participants in our previous work presented in Chapter 3. Different subjects may have different control costs (i.e., rotating the hand and "opening-closing" fingers). Hence, for some participants, the additional control cost required to rotate the hand and/or open the fingers wider may not be worth the small gain in grasping performance.

The proposed optimal feedback control model captures many characteristics of human compensation strategies for grasping objects with directional position uncertainty. Other factors that affect human control have not been captured, however, such as biomechanical constraints or unequal weights on the individual criteria of the optimal control cost function. Estimating the relative weights of the individual criteria through the experimental data is a challenge procedure that is beyond this study. Additionally, people may attempt to optimize and other criteria in addition to stable grasp at first contact, collision avoidance and energy consumption.

The proposed model can be extended to incorporate more realistic dynamics of the human hand. For instance, building on previous studies, we can design realistic dynamics, like the dynamics of N-link arm [53, 169], or incorporate more realistic contact physics in the finger object interactions. Currently this is quite computationally challenging, because it is difficult to design optimal control models for complex redundant systems with non-trivial constraints. One way to tackle this problem is to apply local methods for optimal control, such as differential dynamic programming [41] and iterative LQG [169] to find optimal solutions to the non-linear optimal control model. Additionally, the human hand can be modeled using a hierarchical control framework similar to the one proposed in [54]. This model consists of two layers; a low-level feedback controller, which receives information about the plant state and sends this information to a high-level feedback controller, which solves the original control problem but operates on a simplified model. The proposed framework has been successfully applied to a more realistic human hand model with 7 d-o-f and 14 muscles, whose dynamics resemble those of an actual hand, in tasks like reaching and drawing. For the current study, however, little benefit in insight would be gained from using a more complex model. One of the key results is that simple cost criteria are sufficient to produce trajectories characteristic of human behavior. For some tasks, compensation for uncertainty may exploit intrinsic aspects of the full hand/arm dynamics (like damping), but the full dynamics are not needed to explain grasping behavior for the data we considered.

In addition, we can apply the optimal feedback control framework to model grasping tasks in a more natural environments with obstacles close to the cylinder location. Experimental studies suggest that placing obstacles near the target affects the speed [104] and other parameters, such as

the MGA [114] of the grasping movements. An interesting question that we could address within the optimal control framework is how obstacles affect the optimal strategies for grasping objects with position uncertainty. To accomplish this, we need to incorporate the probability distribution of the obstacles' position in the state. Additionally, the proposed optimal control framework can be extended to study other purposive movement tasks, such as walking and jumping, by building appropriate natural cost functions. For instance, in the walking task, the cost function should include "walking-dependent" criteria that ensure balance during walking, environmental constraints, such as speed, step length and frequency, collision avoidance constraints and control-cost criteria.

In conclusion, the results suggest that compensation strategies in grasping are consistent with the stochastic optimal feedback control with simple task completion and collision avoidance criteria.

Chapter 5

Analysis of spatiotemporal interactions of magnetoencephalographic (MEG) data during copying

5.1 Overview

Although a wealth of knowledge about how people acquire and use information to interact and communicate with the environment has been accumulated, little is known on how the brain encodes this information. From what has been observed in many neurophysiological and functional neuro imaging studies, it appears that information processing involves the cooperation and interaction of multiple, distinct brain regions. In this chapter, we examine the spatiotemporal neural interactions underlying the continuous and sequential movements used to copy geometrical shapes. We experimentally tested the hypothesis that interactions among subsets of magnetoencephalography (MEG) sensors carry information related to changes in movement direction during the copying task. For this study, we took data from a previous experiment, in which 10 subjects continuously copied a pentagonal shape for 45 s using an XY joystick. The subjects performed this task while neuromagnetic fluxes were recorded from their head using a whole-head MEG device [10]. Our initial hypothesis was that neural interactions implement the feedforward-feedback motor control scheme

for planning, executing and correcting movements.

5.2 Introduction

Over the years, many studies have explored the way the brain encodes spatial and temporal information related to spatiomotor tasks. These studies have employed mainly a "center → out" task, sequential motor tasks, and tracing and copying of geometrical shapes. In early $1980's$ Georgopoulos and his colleagues, recorded neural activity from single neurons in the arm region of the motor cortex of macaque monkeys, as the monkeys performed a 2D "center → out" task in 8 directions (at 45° intervals). About half of the recorded cells showed activity related to the task. Of these, more than two thirds exhibited systematic variation with the movement direction. Specifically, each cell's firing rates increased as the monkey's movement trajectory neared the "preferred direction" of the cell and decreased as it moved away from the cell's "preferred direction"; this phenomenon is known as "directional tuning" [16]. Based on this observation, Georgopoulos and his colleagues proposed the "population vector theory" as a framework to describe how an ensemble of neurons in the motor cortex encodes movement directions in 2D [14, 17] and 3D space [7, 8]. According to the theory, each neuron in the ensemble "votes" for its preferred direction by adjusting its firing rate. The actual movement trajectory can be reconstructed by linearly summing the weighted directional contributions of the individual cells [14, 17]. Further work has been done to capture the full kinematics of hand, by extending the directional tuning model to include hand position [143] and hand velocity [35].

Other studies have used tracing and copying shapes, as well as sequential motor tasks, to assess neural mechanisms underlying movement sequences and serial order behavior. Averbeck and his colleagues studied the involvement of prefrontal cortex in copying geometrical shapes, such as triangles, squares and pentagons [22, 23, 25]. They found that the prefrontal cortex carries significant information about the serial position of the movement trajectory and the spatial characteristics of the shape. However, temporal characteristics of the movement trajectory, such as maximum speed and time to maximum speed, were less correlated with neural activity. In a recent study, Averbeck and his colleagues found that superior parietal cortex (SPC) had an enriched representation of

both spatial and temporal characteristics of the copied shapes, with the temporal enrichment being stronger than the spatial enrichment [24]. Other neurophysiological studies have explored the neural mechanisms underlying movement sequences in other brain regions, such as basal ganglia [69], supplementary motor area (SMA) and pre-SMA [68, 161, 174], and premotor and primary motor cortices [46, 47].

Despite the significant contribution of neurophysiological studies to understanding how the brain encodes and processes information, these studies are limited since "they do not see the whole brain". The advantage of modern brain imaging methods, such as functional Magnetic Resonance Imaging (fMRI), Position Emission Tomography (PET), electroencephalography (EEG) and magnetoencephalography (MEG) is that they enable us to study brain functionality "as a whole". These imaging technologies have helped researchers formulate the idea that the brain has a hierarchical structure, in which large-scale cortical networks interact to encode and process information from the environment. To better understand on how the brain does this, it is necessary to understand the functional properties of cortical areas, their connectivity and the spatiotemporal pattern of activity among them.

Previous studies have used fMRI to assess the function of different brain regions and their interconnections with other cortical areas, while subjects performed a variety of motor and cognitive tasks, such as copying geometrical shapes [154, 164] and attention tasks [96, 119]. fMRI uses strong magnetic fields to measure variations in the Blood Oxygenation Level Dependent (BOLD) signal over time (hemodynamic response) as the neural activity changes in a given brain area. Although modern MRI scanners are able to achieve a spatial resolution of $3-5$ mm, their temporal resolution is limited to $3-5$ s, due to relative slow hemodynamic response of the brain [151].

EEG and MEG overcome this poor temporal resolution, by directly measuring the electromagnetic activity, respectively of the brain and sampling at high rates to achieve a temporal resolution on the order of ms [110, 122, 126]. In both EEG and MEG, sensors are arranged on the surface of the head. MEG sensors record the synchronous synaptic activity in thousand of neurons in brain regions typically near the sensors. EEG sensors measure the associated scalp potentials. Although EEG and MEG signals originate from the same neurophysiological processes, there are

important differences. Magnetic fields are less distorted than electric fields by the inhomogeneous conductivity of the intervening tissues (e.g., skull, scalp, cerebrospinal fluid). Thus, the higher spatial precision of MEG signals makes the MEG spatial localization less ambiguous. Because MEG signals are on the order of few femtoteslas, it is necessary to conduct the experimental acquisition within magnetically shielded chambers. It is also better to conduct EEG acquisitions in electrically shielded rooms, but this is less crucial than MEG.

Both MEG and EEG techniques provide excellent temporal resolution, but relatively low spatial resolution compared to fMRI. Due to the high temporal resolution, these techniques are suited for studies in which the timing of neural activity is of interest [160], such as assessing short temporal interactions between cortical regions during cognitive and motor control tasks. Previous studies have used EEG to explore cortical interactions during simple motor control tasks, such as paced finger movements [28, 100], simple finger movements with different rates [95] and also more complex movements, such as the visuomotor task of reaching a target [18] and tasks involving sequences of bimanual movements [58]. Similarly, other studies have used MEG to assess changes in neural activity and functional coupling of cortical regions during cognitive and motor control tasks, such as fixation on single spot [59] and copying geometrical figures continuously and without visual feedback [10].

Although these studies revealed significant findings about the functional coupling of cortical regions in spatiomotor tasks, they did not address the question on how these interactions are associated with behavioral parameters of these tasks. The major objective of this study was to explore the spatial and temporal interactions of brain regions underlying movement sequences and the association of these interactions with movement parameters. Data were taken from a previous study [10], in which 10 subjects were instructed to copy a pentagonal shape continuously for 45 s using an XY joystick, while neuromagnetic fluxes were recorded from the whole head of subjects by MEG. After removing extraneous noise (e.g., cardiac artifact) from the recordings, we used a Box-Jenkins Autoregressive, Integrated Moving Average (ARIMA) model to the unsmoothed and unaveraged MEG raw data, to remove confounding autocorrelations and trends (i.e., to "prewhite" the data). Since we were interested in assessing neural interactions over small time intervals, we divided the

prewhitened time series obtained from each MEG sensor into time-bins of 51 ms; we then computed the cross-correlation between pairs of sensors over ± 25 time-lags (~ 51ms) within each time-bin. Additionally, we used the circular standard deviation of the movement direction within that interval to estimate the variability of the movement direction for 51ms trajectory segments. We applied ARIMA model to the individual time series of the circular standard deviations to yield residual practically stationary. Next, we performed a cross-correlation analysis between the strength of the peak pair wise MEG cross-correlations and the circular standard deviations across all pairs of sensors and subjects. We found that neural interactions and variability of movement direction are integrated in a feedforward-feedback control scheme. That is, we found neural interactions that precede (forward) or follow (feedback) changes in movement direction. Furthermore, we explored whether there are differences on neural interactions associated with low and high variability of movement direction. For that purpose, we assigned all the trajectory segments into two groups based on a threshold on the variability of movement direction - namely segments with high and segments with low directional variability. We found a rich and consistent pattern of neural interactions with respect to the sign, the strength and the time-lag of cross-correlations. Although, these patterns tend to be conserved between the two groups, we found pairs of sensors that have significantly different strength of cross-correlations between the two groups.

5.3 Materials and methods

5.3.1 Subjects

Ten healthy right-handed subjects (23-41 years old, 5 men and 5 women) with normal or corrected-to-normal vision and with no known neurological or physical dysfunction participated in the MEG-imaging study for monetary compensation. The appropriate institutional review board approved the study protocol and informed consent was obtained prior to the study based on the Declaration of Helsinki.

5.3.2 Experimental paradigm

Task

Subjects were instructed to perform three 45 s consecutive tasks (two fixation and one copy task), Fig. 5.1. In the first task ("rest" task"), subjects fixated a spot of blue light presented on the center of the screen. When the color of light turned red, the spot was surrounded by an outline of a pentagon, and the subjects continued fixating for another 45 s ("visual task"). Finally, the fixation spot turned green and subjects copied the outlined pentagon continuously using an XY joystick with the right hand ("motor task"). Subjects were instructed to fixate during all tasks. They copied the pentagon counterclockwise at their own speed without visual feedback of the joystick movement. In the current study, we focus only on the motor task.

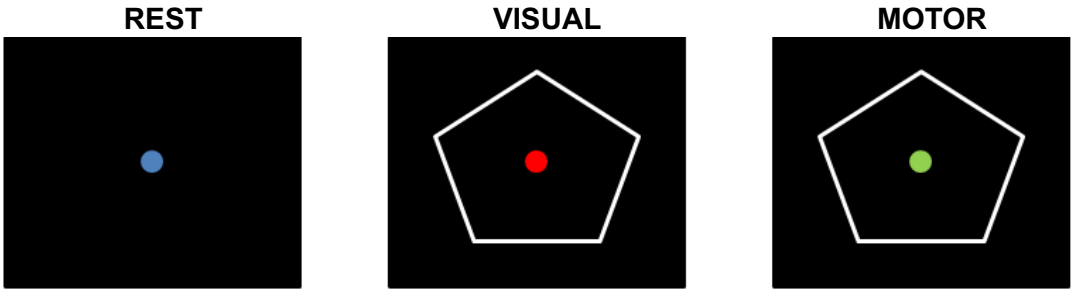

Figure 5.1: Illustration of the experimental paradigm. **Rest task**: A blue fixation spot was presented on the center of the screen and subjects were required to fixate for 45 s. **Visual task**: The color of the fixation spot turned red and was surrounded by a pentagonal outline; the subjects continued fixation for another 45 s. **Motor task**: When the fixation spot turned green, subjects were instructed to copy the pentagon counterclockwise at their own speed using an XY joystick with their right hands. No visual feedback was provided.

Experimental set-up

The task stimuli were generated by a computer and were presented on a display 62 cm in front of the subjects, using a Liquid Crystal Display (LCD) project and a periscopic mirror system. The 2D pentagon displayed subtended approximately 10° of visual angle. The subjects lay supine in the recording chamber having their head inside the cryogenic helmet-shaped dewar, Fig. 5.2 (left panel). During the motor task, the subjects copied the pentagon using a 2D joystick (joystick model

Figure 5.2: **Left**: The 248-sensor whole-head MEG system is located inside a shielded room that reduces electromagnetic and environmental noise. **Right**: The subjects lay supine in the recording chamber with their heads inside the cryogenic helmet-shaped dewar. The joystick was mounted comfortably at arm's length on the right side.

541 FP, Measurement Systems, Norwalk, CT; remodeled by removing all the magnetic parts). The joystick was placed on a rectangular plastic sheet (22.6×19.5) cm^2 and raised 3.5 cm above the resting bed and tilted at an angle of $30.6\,^\circ$.

5.3.3 Data acquisition

Magnetoencephalography (MEG)

Brain activity was recorded using a 248-sensors whole-head axial MEG system (Magnes 3600 WH, 4-D Neuroimaging, San Diego, CA), Fig. 5.3. The cryogenic helmet-shaped dewar of the MEG system was located inside a shielded room that reduced electromagnetic and environmental noise Fig. 5.2 (right panel). The MEG data were recorded at 1017.25 Hz and filtered down to $0.1 - 400$ Hz during acquisition.

Hand movement

The XY position of the joystick was sampled synchronously at the same rate as the MEG signals (i.e., 1017.25 Hz).

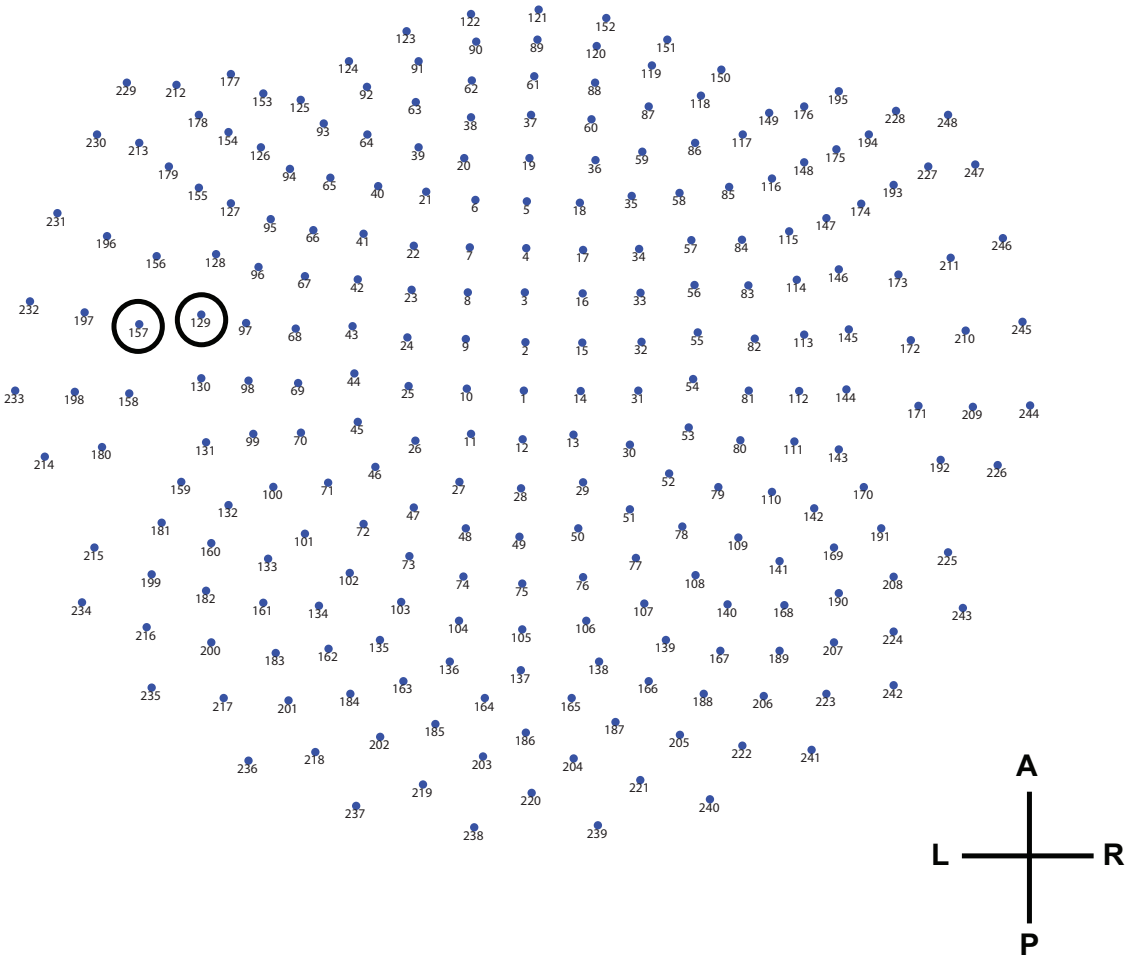

Figure 5.3: 2D projection of the 248-channel axis gradiometer MEG system used to record brain activity

5.3.4 Data Analysis

The MEG data were 248 time series with $\sim 45,000$ values per sensor per subject. The obtrusive, cardiac artifact was removed from the MEG data using the event-synchronous subtraction method [9].

5.3.5 Time series analysis

Neurophysiological time series often are not stationary with respect to their mean and variance, and in many cases are dominated by trends, which should be recognized before any analysis is done. Without removing nonstationarities from the data, spurious associations could arise [10, 64,

66]. Since the main goal of this study was to assess pair wise interactions between MEG time series, the data should be stationary. Therefore, we used Autoregressive Integrated Moving Average (ARIMA) modeling to remove any autocorrelation and possible trends in the recorded MEG data. The autoregressive (AR) model eliminates any linear dependencies (i.e. autocorrelations) within the individual time series; the integrated factor (I) differentiates the time series to remove possible linear trends; and the moving average (MA) model smoothes the time series by taking the weighted linear summation of random shocks (i.e., noise terms). Based on a previous MEG studies [10, 59], an ARIMA(25,1,1) model was adequate to obtain quasi-stationary time series (i.e. "prewhitened" data).

5.3.6 MEG time series cross-correlation analysis

The major objective of this study was to assess how spatiotemporal neural interactions are changes with time during the copying task. To analyze this, we divided each prewhitened MEG time series into *N* time-bins of length 51 ms and performed a cross-correlation analysis between all possible pairs of sensors (30,628) over ± 25 time-lags including zero-lag. The cross-correlation function (CCF) between pairs of stationary residuals was computing using the IMSL statistical routine DCCF (Compaq Visual Fortran Professional Edition, version 6.6B). We normalized the distribution of the pair wise cross-correlation before averaging across subjects using Fisher's z-transformation, Eq. (5.1).

$$z_{ij}(t) = \frac{1}{2}\left[\ln\left(1 + c_{ij}\left(t\right)\right) - \ln\left(1 - c_{ij}\left(t\right)\right)\right] \tag{5.1}$$

where $c_{ij}(t)$ is the pair wise cross-correlation between sensor i and j at time-lag t.

To characterize the cross-correlogram, we determined the time-lag at which the peak cross-correlation occurred, t_{max}, and the value at that time-lag $z_{ij}(t_{max})$. Hence, $30,628\times$N$\times 10$ (where N is the number of time-bins and 10 the total number of subjects) peak of cross-correlations $z_{ij}(t_{max})$s with the corresponding t_{max}s were available for further analysis.

5.3.7 Behavioral data analysis

The XY output of the joystick was smoothed using a cubic spline approximation to reduce noise from the joystick. Fig. 5.4 illustrates a typical example of a 5.5-s-long segment of the original and smoothed trajectory. In addition, we computed two measures to characterize the "straightness" of the movement and the variability of movement direction within a time-bin:

Index of linearity, *I*

The index of linearity *I*, characterizes the general straightness of the movement trajectory and is defined as the ratio of the maximal deviation of the actual trajectory from the straight trajectory to the length of the straight trajectory. The straight trajectory corresponds to the line connecting the start and the end points of the actual trajectory [27]. If the index of linearity is 0, the movement trajectory is a perfect straight line, whereas if it is 1, the movement trajectory is circular. We used the index of linearity to estimate the straightness of the movement trajectory within a time-bin of 51 ms. Fig. 5.5 shows an example of two 51 ms long segments of the trajectory with low (green segment) and high (red segment) indexes of linearity (i.e, I_{small} = 0.1562, I_{large} = 0.2178).

Circular standard deviation, $\bar{S}$

The circular standard deviation, $\bar{S}$, of the movement direction describes the variability of movement direction within a 51 ms time-bin, Eq. (5.2)

$$\bar{S} = \sqrt{(-2\ln \bar{R})}, \quad \bar{R} = \frac{1}{M}\sqrt{\left(\sum_{t=1}^{M}\cos\theta_t\right)^2 + \left(\sum_{t=1}^{M}\sin\theta_t\right)^2} \tag{5.2}$$

where M is the length of the time-bin (51 ms) and θ_t is the instantaneous direction of the movement at a given time t. The lower the circular standard deviation, the lower the variability of movement direction. For example, the circular standard deviation of the "green" and "red" 51-ms-long segment of the movement trajectory in Fig. 5.5 is 4.9848 and 35.4538, respectively.

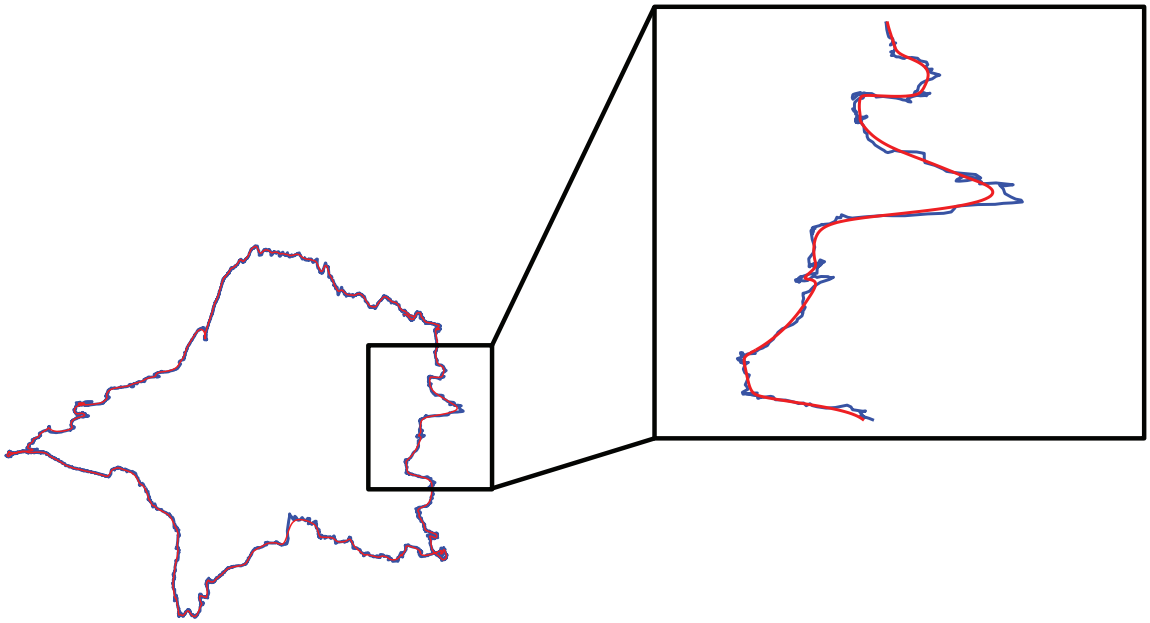

Figure 5.4: Illustration of the original (blue) and smoothed (red) movement trajectory from a typical 5.5 s-long segment (out of 45 s total).

5.3.8 Analysis of the relation between neural interactions and variability of movement direction

Our initial hypothesis was that neural interactions are associated with the variability of movement direction during the copying task. To test that, we performed a cross-correlation analysis between the peak of MEG cross-correlations $z_{ij}(t_{max})$s and the log-transformation of the circular standard deviations $\bar{S}$s. However, we found that the time series of the log-transformed circular standard deviations were not stationary. Following the same procedure with the neural data, we used an ARIMA model to remove the autocorrelation structure of the circular standard deviation time series. After extensive ARIMA modeling and diagnostic checking, including the computation and evaluation of the autocorrelation (ACF) and the partial autocorrelation function (PACF) of the residuals, we found that ARIMA(10,1,0) was adequate to yield quasi-stationary time series. Note that the time series of the peak of MEG cross-correlations $z_{ij}(t_{max})$s were quasi-stationary and did not require ARIMA modeling. We performed the cross-correlation analysis within $\pm$ 3 time-lags, including zero. We chose this time-lag based on previous studies, which found that neural activity precedes actual hand movement by some amount of time [35, 173]; the time between the neural activity and the hand

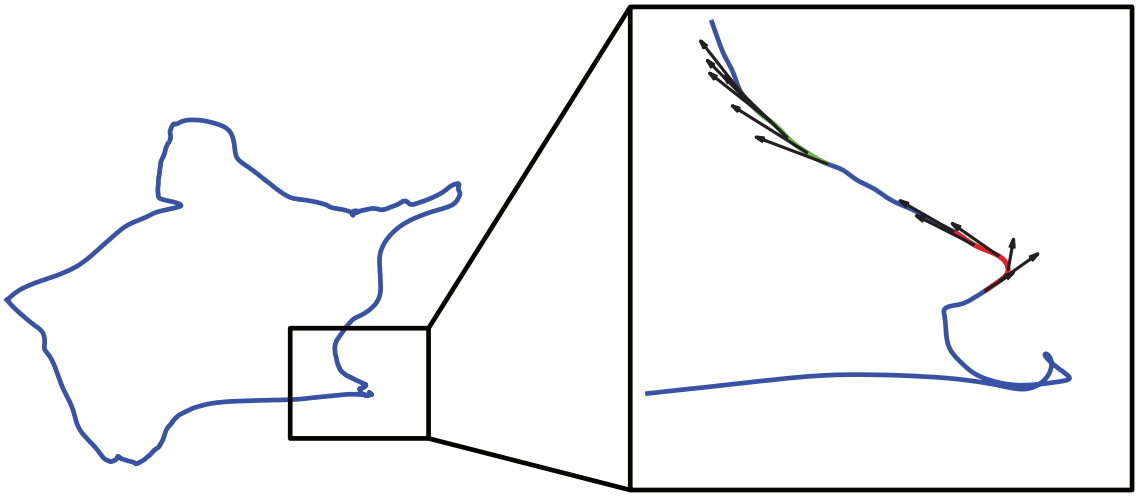

Figure 5.5: Illustration of two 51 ms long segments (out of 45 s total) of the movement trajectory with low (green segment) and high (red segment) indexes of linearity (I_{low} = 0.1562, I_{high} = 0.2178) and circular standard deviation ($\bar{S}_{low}$ = 4.9848, $\bar{S}_{high}$ = 35.4538). Black arrows correspond to the instantaneous direction of the movement.

movement varies linearly with the radius of curvature of the movement trajectory [47], but it is does not exceed 150-200 ms.

To better understand on how neural interactions are related to variability of movement direction, we further explored these interactions for trajectory segments with low and high directional variability. From the histogram of the circular standard deviation, we classified the time-bins into two categories: 1) time-bins, in which the corresponding circular standard deviation of the movement direction was less than 20% the histogram mean and 2) time bins, in which the corresponding circular standard deviation of the movement direction was equal to or greater than 20% the histogram mean. Although this threshold was selected somehow arbitrarily, other threshold values (e.g., 25% , 30%) gave similar results. We then compared the pattern of neural interactions with respect to the sign, strength and time-lag of the peak of the cross-correlations between the two categories.

5.4 Results

5.4.1 Prewhitening neural data

Before beginning the time series analysis, we discarded the first and last $1,000$ points (i.e,. the first and the last 1,000 seconds) to avoid potential interference from processes at the start or end of the task [10]. We then evaluated the stationarity of the raw data. Figs. 5.6 and 5.7 display a 3 s long segment of the MEG data from sensors 129 and 157, respectively, before and after applying the ARIMA(25,1,1) model. Before the model was applied, the raw series were not stationary with respect to their mean and standard deviation. However, the non-stationarity was significantly reduced after applying the ARIMA model. In addition, Figs. 5.8 and 5.9 (A and C panels) display the autocorrelation function (ACF) and the partial autocorrelation function (PACF) of the raw data recorded from sensors 129 and 157, respectively. The structure of ACFs and PACFs indicate that raw data are not stationary with respect to their autocorrelation. However, after applying ARIMA model, ACFs and PACFs for both sensors became flat, indicating that the prewhitened data (i.e., ARIMA residuals) are also stationary with respect to their autocorrelations, Figs. 5.8 and 5.9 (B and D panels) (see [10] for further information about time series analysis in MEG data).

The importance of prewhitening the original time series for assessing interactions between pairs of MEG sensors is shown in Fig. 5.10. Panels A and B of Fig. 5.10 depict the cross-correlation function (CCF) between sensors 129 and 157 over ± 25 time-lags before and after applying ARIMA(25,1,1) modeling. It is clear that the CCF structure of the raw data is dominated by the autocorrelated structure of the individual time series, since the two sensors are highly correlated across the whole span of 51 lags. The actual CCF between these two sensors is more localized around ± 4 time-lags and with lower, but still statistically significant, correlations. Panels C and D of Fig. 5.10 illustrate the CCF between sensors 129 and 157 for an arbitrary time-bin of 51 ms, before and after ARIMA(25,1,1) modeling.

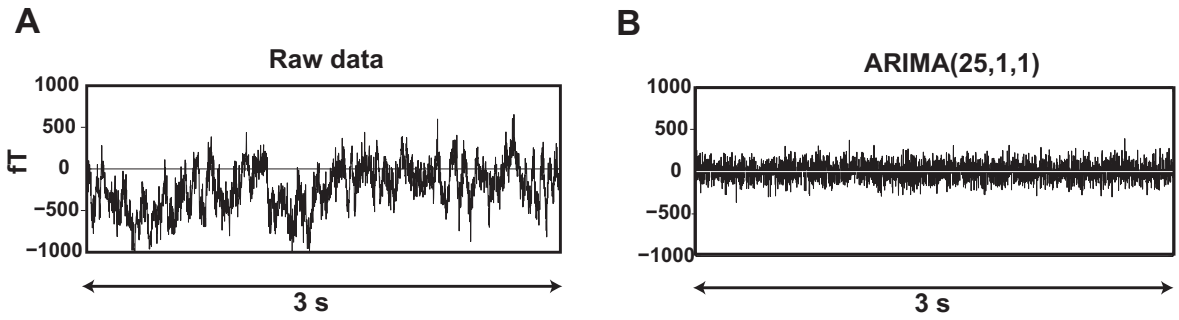

Figure 5.6: MEG raw data (3-s-segment out of 45 s total) from sensor 129 (**A**) before and (**B**) after applying ARIMA(25,1,1) modeling.

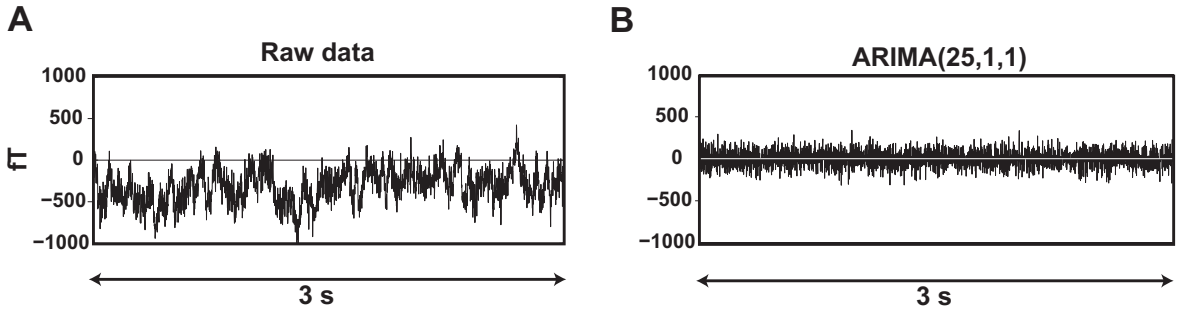

Figure 5.7: MEG raw data (3-s-segment out of 45 s total) from sensor 157 (**A**) before and (**B**) after applying ARIMA(25,1,1) modeling.

5.4.2 Cross-correlation analysis of MEG time series

We calculated the cross-correlation over 51 ms time-bins for every possible pair of sensors over $\pm$ 25 time-lags ($\sim$ 51 ms - 1 lag is equivalent to 0.983 ms, as the sampling frequency is 1017.25 Hz). From the 248 MEG sensors, we produced $\begin{pmatrix} 248 \\ 2 \end{pmatrix}$ $\times$ *N time-bins* $\times$ *10 subjects* cross-correlograms and then normalized the distribution of the cross-correlations using Fisher's z - transformation (see Methods section) to calculate the descriptive and other statistics.

We characterized the cross-correlogram by computing the sign, the strength of the peak cross-correlation $z_{ij}(t_{max})$ and the time-lag t_{max} at which the peak of cross-correlation occurred. The frequency distribution of the peak of cross-correlations across pairs of MEG sensors, time-bins and subjects is illustrated in Fig. 5.11A (only where $p < 0.05$). The distribution is almost symmetric around 0, although there are slightly more positive (90,528,648 out of 178,111,539 total = 50.83%)

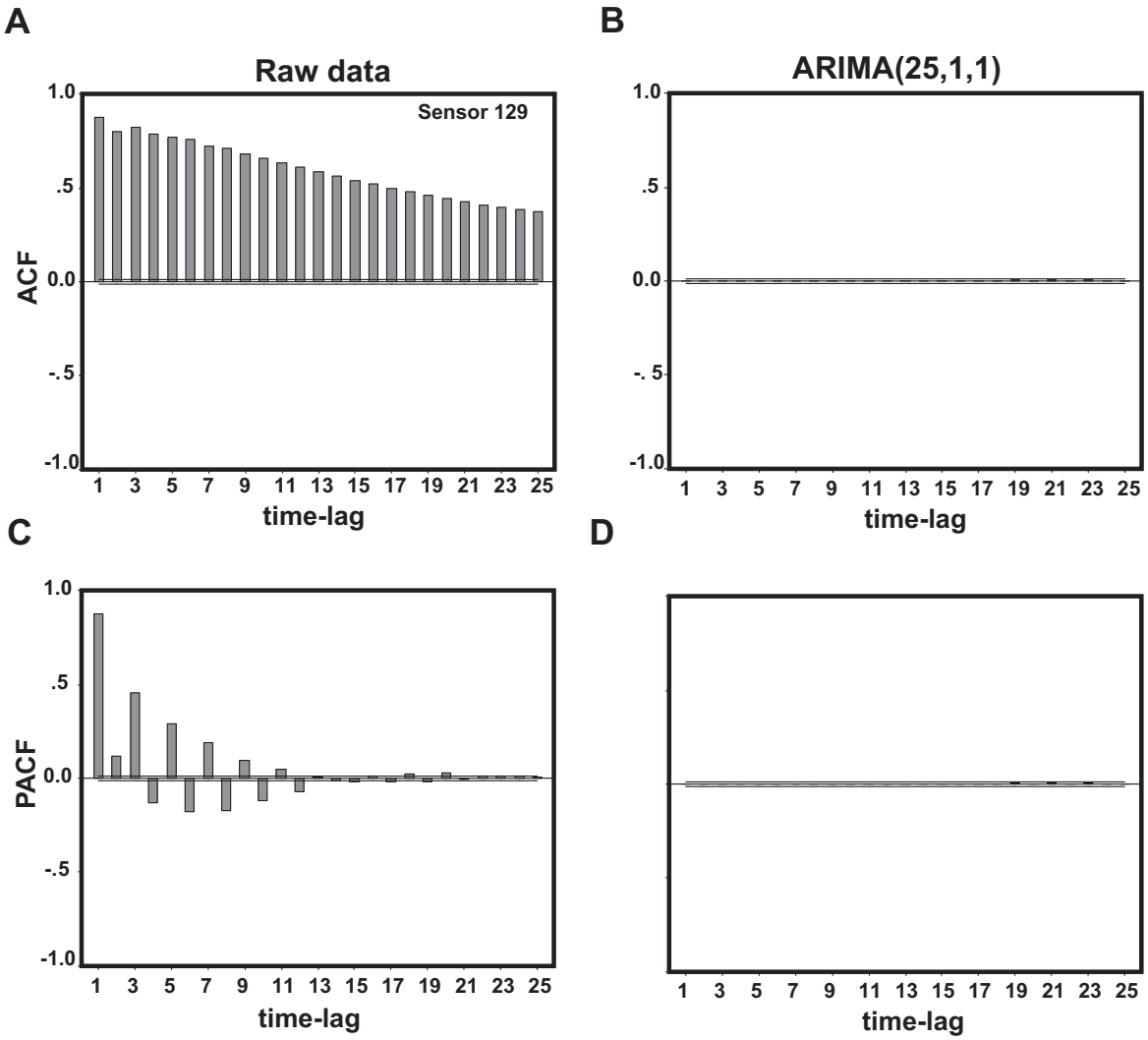

Figure 5.8: ACF structure of the MEG signal recorded from sensor 129 before (**A**) and after (**B**) applying an ARIMA(25,1,1) model. PACF structure of the MEG signals recorded from the same sensor before (**C**) and after (**D**) applying the model. The black lines that are close to the reference zero-line, denote 95 % statistical significance level from the ACF and PACF value. Notice that the strong autocorrelation and partial-autocorrelation structure on the raw data disappeared after applying ARIMA(25,1,1) modeling. That is, the ACFs and PACFs are flat.

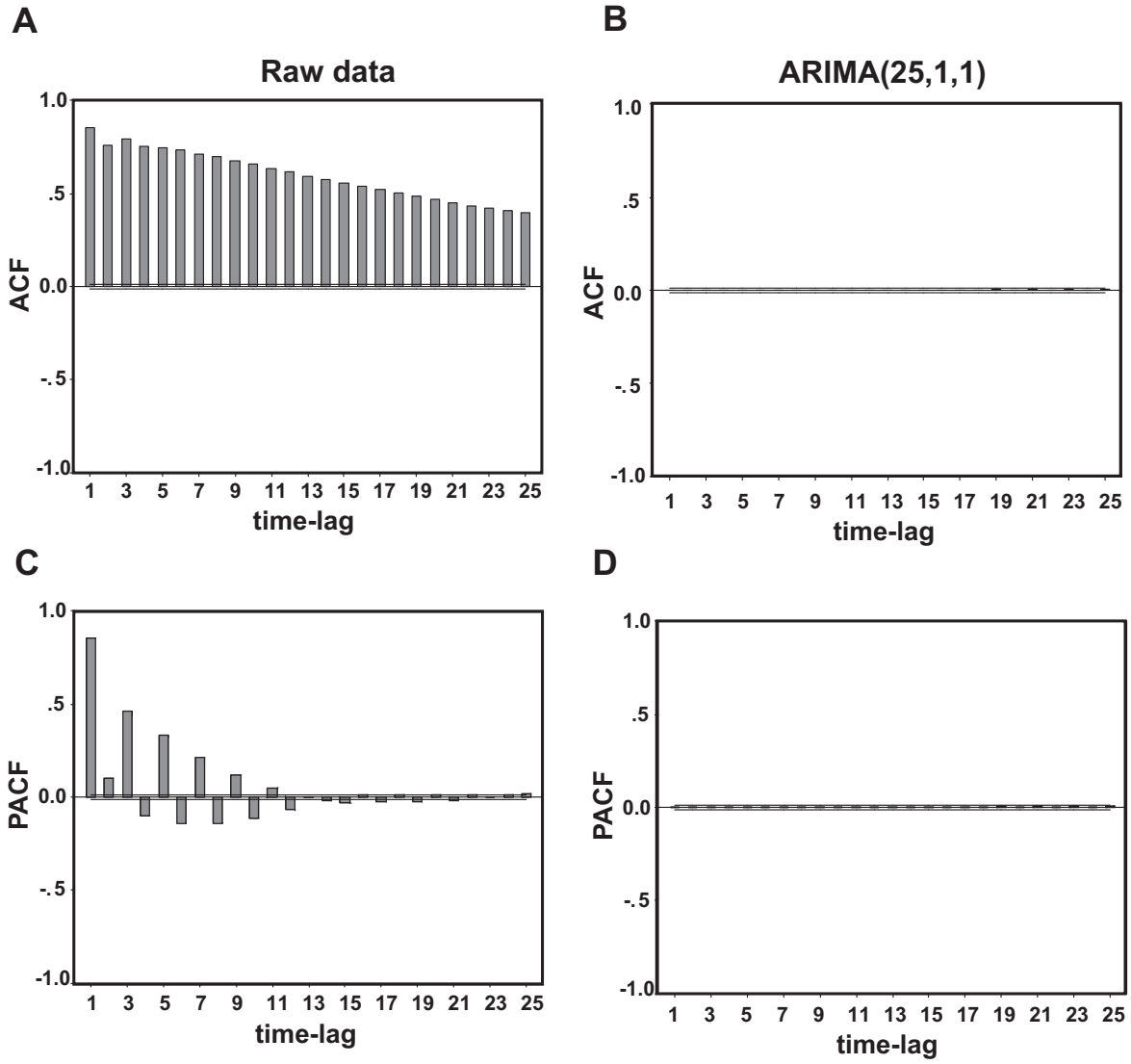

Figure 5.9: ACF structure of the MEG signal recorded from sensor 157 before (**A**) and after (**B**) applying an ARIMA(25,1,1) model. PACF structure of the MEG signals recorded from the same sensor before (**A**) and after (**B**) applying the model. The black lines that are close to the reference zero-line, denote 95 % statistical significance level from the ACF and PACF value. Notice that the strong autocorrelation and partial-autocorrelation structure on the raw data disappeared after applying ARIMA(25,1,1) modeling. That is, the ACFs and PACFs are flat.

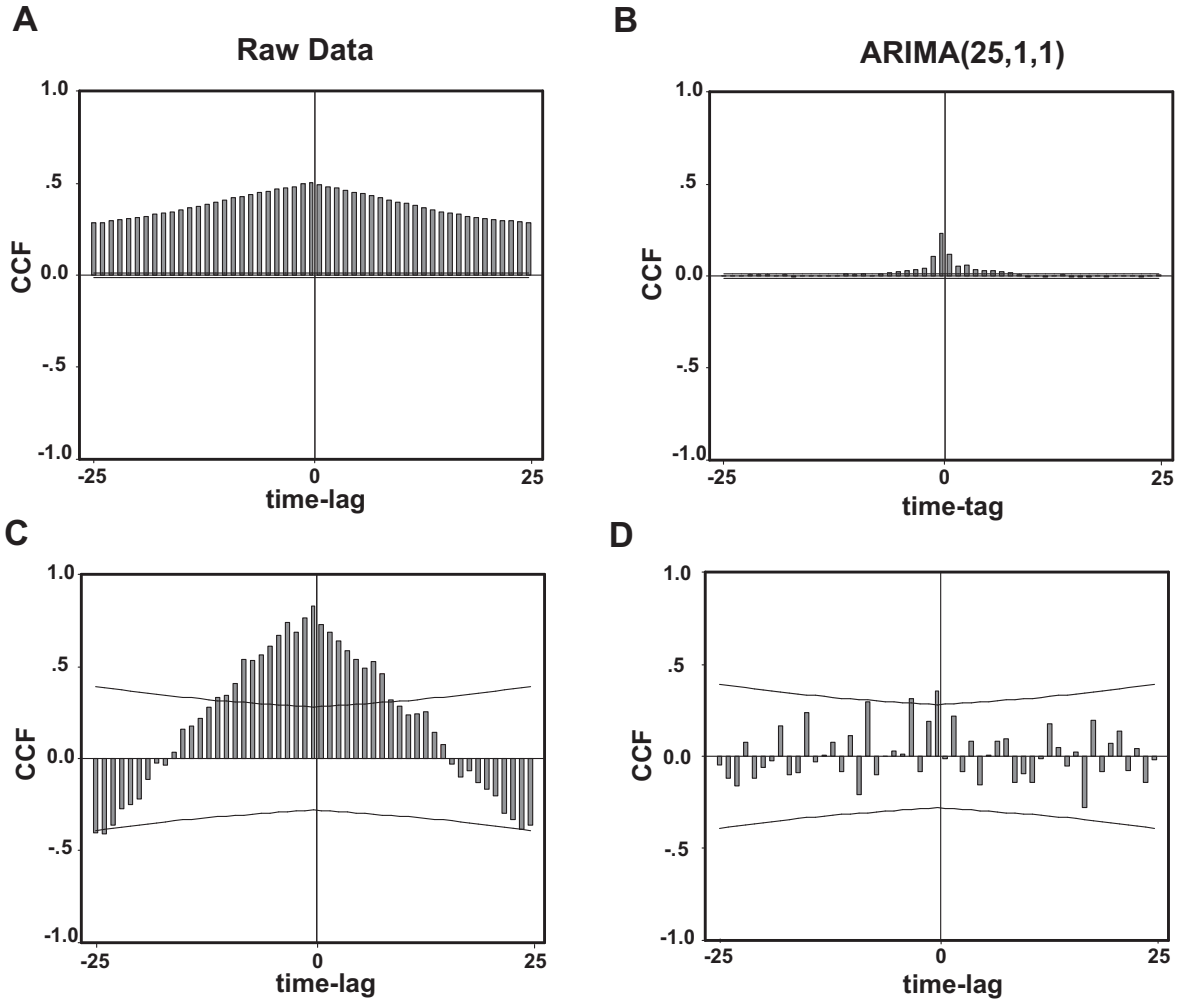

Figure 5.10: Cross-correlation function (CCF) between sensors 129 and 157 (**A**) before and (**B**) after applying ARIMA(25,1,1) modeling over ± 25 time-lags including zero-lag. Notice that raw data recorded from these two sensors are highly correlated across the whole span of 51 lags, which indicates that CCF is dominated by the autocorrelated structured of the individual time series. The actual CCF is more localized around $\pm$ 4 lags with lower, but still statistically significant, correlations. Panels (**C**) and (**D**) illustrate the CCF between the same sensors but for an arbitraty time-bin of 51 ms.

than negative (87,582,891 out of 178,111,539 total = 49.17%) values. Additionally, the average values of the positive and negative $z_{ij}(t_{max})$ were $0.3462 \pm 5.9034 \times 10^{-6}$ and $-0.3451 \pm 5.8525 \times 10^{-6}$ (mean $\pm$ SEM), respectively. The frequency distribution of the corresponding t_{max}, which is illustrated in Fig. 5.11B, is symmetric around the zero-lag. Finally, we found that 11,369,905 out of 178,111,539 (6.38%) $z_{ij}(t_{max})$ were at the zero-lag and the rest of them (93.62 %) were at non zero-lag. We summarize all these basic statistics for the individual subjects in Tables 5.1 and 5.2. Notice the similarity in the peak of the cross-correlation between MEG sensors and the time-lag at which it occurred across all subjects.

Next, we looked at how many of the peak cross-correlations are positive and how many are negative at any given time-lag t_{max} ($t_{max} = [-25, 25]$). The frequency distribution of the positive and negative peak cross-correlations for all t_{max} is shown in Fig. 5.11C. We also present the frequency distribution of the difference between the number of positive and negative peak cross-correlations for all t_{max}, Fig. 5.11D. We found that there were more positive than negative $z_{ij}(t_{max})$s around zero-lag (i.e., synchronous interactions), whereas there were slightly more negative than positive $z_{ij}(t_{max})$s for t_{max} greater than 5 or lower than -5 away from the zero-lag.

5.4.3 Behavioral data analysis

We divided the XY joystick movement trajectory in 51 ms time-bins and used two measures to characterize the straightness of the trajectory and the variability of movement direction within each time-bin. Specifically, we computed the index of linearity *I* and the circular standard deviation $\bar{S}$ of the movement direction for each 51 ms trajectory segment. The relative frequency distribution of *I* and $\bar{S}$ across all time-bins and subjects are presented in Figs. 5.12A and 5.12B, respectively. We also computed the log-transformation of both *I* and $\bar{S}$ to make the distributions symmetric. Table 5.3 summarizes some of the basic statistics of the log-transformed *I* and $\bar{S}$ across time-bins and subjects. Notice the variability in both *I* and $\bar{S}$ among subjects; although the basic statistics of neural interactions are very similar across subjects, the behavioral characteristics can vary significantly.

Additionally, we regressed the log-transformed *I* against the log-transformed $\bar{S}$ and found that these metrics are highly correlated (i.e., r = 0.7424, p $<$0.0001). However, for the rest of the

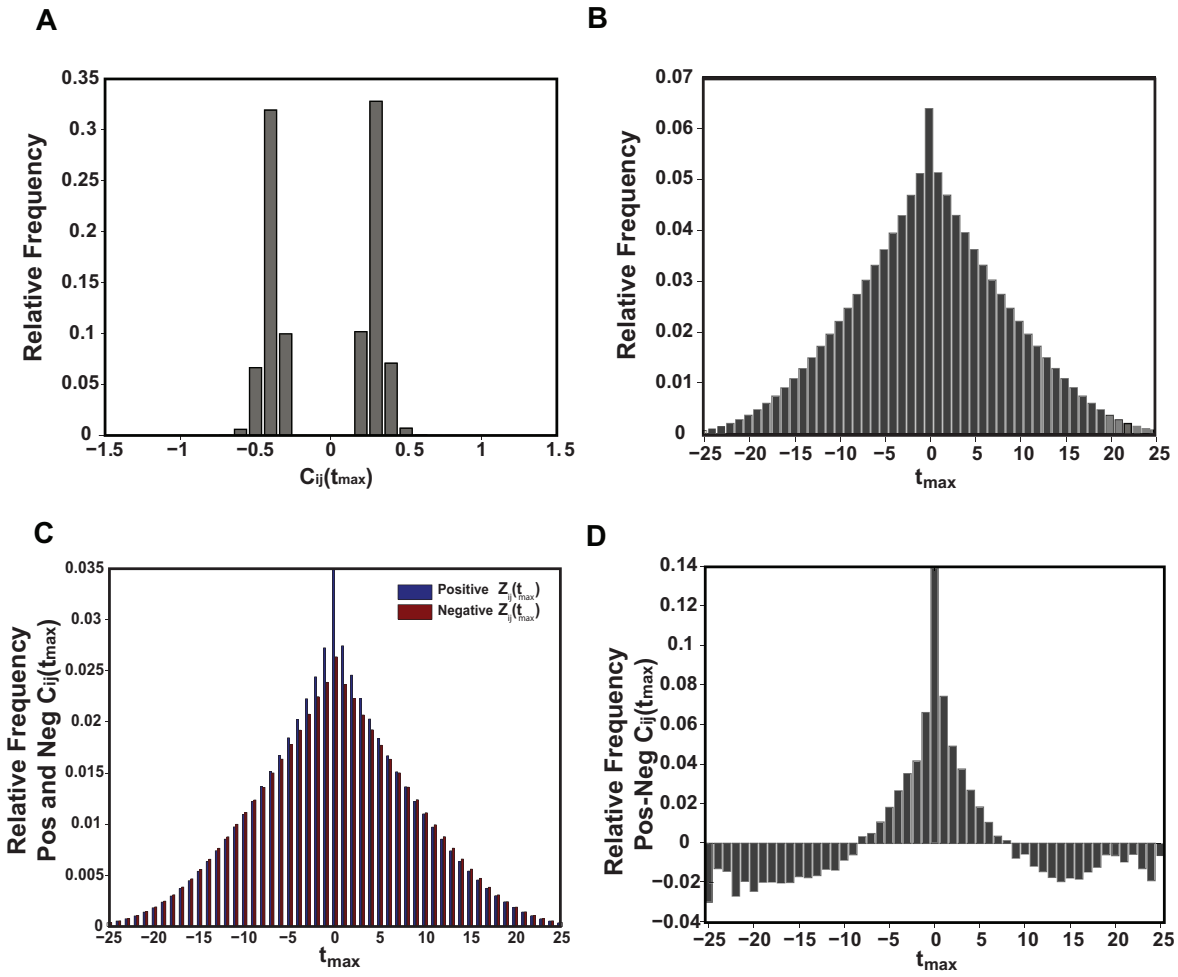

Figure 5.11: (**A**): Relative frequency distribution of the peak of cross-correlations. (**B**): Relative frequency distribution of the time-lags t_{max}s that peak of cross-correlations occurred. (**C**): Relative frequency distribution of the positive (blue bars) and negative (red bars) peak of cross-correlations at all t_{max}s. (**D**) Relative frequency distribution of the difference between the number of positive and negative peak of cross-correlations across all t_{max}s. The frequency distributions were computed across all pairs of MEG sensors, time-bins and subjects.

Table 5.1: Basic statistics summary of $z_{ij}(t_{max})$ and t_{max} for all subjects.

Subjects	$z_{ij}(t_{max})$ total	$z_{ij}(t_{max})$ $p < 0.05$ (%)	Positive (%) $z_{ij}(t_{max})$	Negative (%) $z_{ij}(t_{max})$	Asynch (%) t_{max}	Synch (%) t_{max}
1	26,217,568	18,045,076 (68.82)	50.57	49.43	93.19	6.81
2	26,217,568	17,999,385 (68.65)	50.56	49.44	93.54	6.46
3	26,217,568	18,078,719 (68.96)	50.74	49.26	92.51	7.49
4	26,217,568	17,958,898 (68.50)	51.17	48.83	93.83	6.17
5	26,217,568	17,989,091 (68.61)	50.83	49.17	93.39	6.61
6	25,053,704	17,180,962 (68.58)	50.80	49.20	93.95	6.05
7	26,003,172	17,812,316 (68.50)	51.00	49.00	94.11	5.89
8	25,788,776	17,677,959 (68.54)	50.91	49.09	93.96	6.03
9	25,666,264	17,649,929 (68.76)	50.54	49.46	93.83	6.17
10	25,819,404	17,719,204 (68.62)	51.71	48.83	93.88	6.12

Table 5.2: Mean, median and standard deviation of positive and negative $z_{ij}(t_{max})$

Subjects	Positive $z_{ij}(t_{max})$			Negative $z_{ij}(t_{max})$		
	Mean	Median	Std	Mean	Median	Std
1	0.3470	0.3386	1.8805 10^{-5}	-0.3453	-0.3376	1.8397 10^{-5}
2	0.3458	0.3378	1.8489 10^{-5}	-0.3448	-0.3371	1.8327 10^{-5}
3	0.3475	0.3388	1.9115 10^{-5}	-0.3454	-0.3376	1.8482 10^{-5}
4	0.3454	0.3375	1.8309 10^{-5}	-0.3445	-0.3368	1.8364 10^{-5}
5	0.3463	0.3380	1.8696 10^{-5}	-0.3448	-0.3371	1.8403 10^{-5}
6	0.3459	0.3379	1.8888 10^{-5}	-0.3451	-0.3374	1.8848 10^{-5}
7	0.3457	0.3378	1.8422 10^{-5}	-0.3450	-0.3373	1.8509 10^{-5}
8	0.3463	0.3382	1.8656 10^{-5}	-0.3454	-0.3377	1.8624 10^{-5}
9	0.3468	0.3387	1.8805 10^{-5}	-0.3457	-0.3379	1.8629 10^{-5}
10	0.3462	0.3382	1.8578 10^{-5}	-0.3452	-0.3376	1.8603 10^{-5}

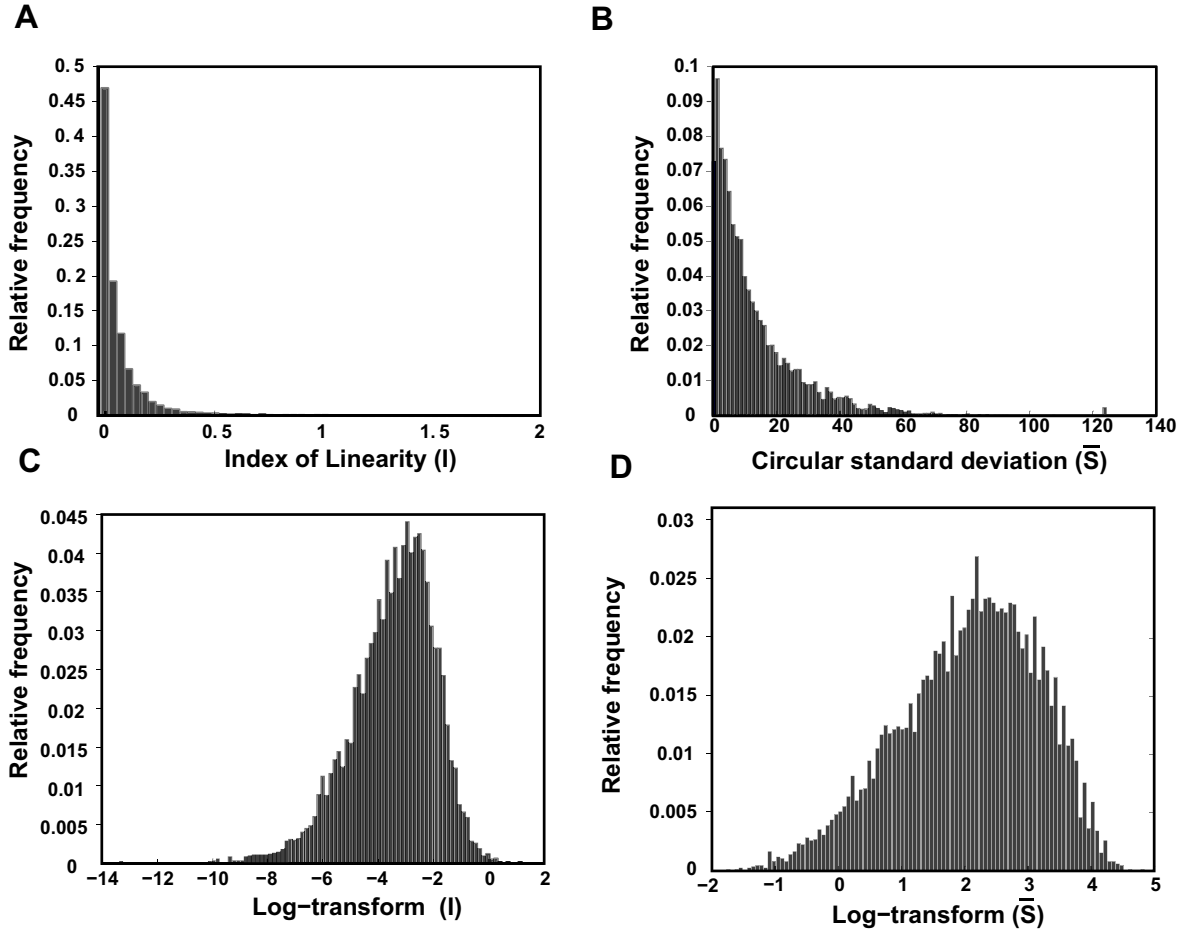

Figure 5.12: Relative frequency distribution of (**A**) index of linearity, *I*, and (**B**) the circular standard deviation, $\bar{S}$, of the movement direction for 51 ms segment of the trajectory across all time-bins and subjects. The panels (**C**) and (**D**) illustrate the frequency distribution of the log-transformed of *I* and $\bar{S}$.

Table 5.3: Mean, median and standard deviation of log-transformed *I* and $\bar{S}$ across time-bins for each subject.

Subjects	$\log I$			$\log \bar{S}$		
	Mean	Median	Std	Mean	Median	Std
1	-3.3058	-3.1460	1.4169	2.1209	2.1772	1.0370
2	-3.8992	-3.7517	1.5642	1.6257	1.6124	1.0683
3	-3.6651	-3.4251	1.5104	1.8106	1.8526	0.9157
4	-3.5181	-3.3316	1.4033	1.9329	2.0368	1.0179
5	-3.8829	-3.8134	1.4556	1.6111	1.5632	1.1733
6	-2.8606	-2.6365	1.3575	2.4753	2.6661	1.0592
7	-3.1405	-3.0227	1.3061	2.3828	2.4630	0.9841
8	-3.4589	-3.1276	1.7695	2.1789	2.3824	1.1941
9	-2.8636	-2.6156	1.4383	2.7188	2.7883	0.7596
10	-3.3380	-3.1301	1.5998	2.1271	2.3137	1.1726

analysis, we focus on $\bar{S}$, because it serves as a measure of the variability of movement direction as opposed to the straightness of the movement trajectory.

Next, we evaluated the stationarity of the log-transformed $\bar{S}$. Figs. 5.13A and 5.13C present the autocorrelation (ACF) and the partial autocorrelation (PACF) function of a typical log-transformed $\bar{S}$. The structure of both ACF and PACF indicate that the log-transformed $\bar{S}$ is not stationary. However, ACF and PACF became flat after applying ARIMA(10,1,0) model, indicating that the prewhitened data are stationary, Figs. 5.13B and 5.13D.

5.4.4 Analysis of the relation between neural interactions and variability of movement direction

To look at the relationship between neural interactions and variability of movement direction, we performed a cross-correlation analysis between $z_{ij}(t_{max})$ and prewhitened log-transformed $\bar{S}$ over ± 3 time-lags including zero-lag. Note that in this analysis 1 time-lag corresponds to ± 25 time-lags (i.e, $\sim$ [0, 51] ms) in the cross-correlation analysis of the MEG prewhitened time-series (since we are looking at $z_{ij}(t_{max})$).

Altogether, 306,280 (30,628 pairs of MEG sensors $\times$ 10 subjects) cross-correlograms were available for further analysis. We normalized the distribution of the cross-correlation values before

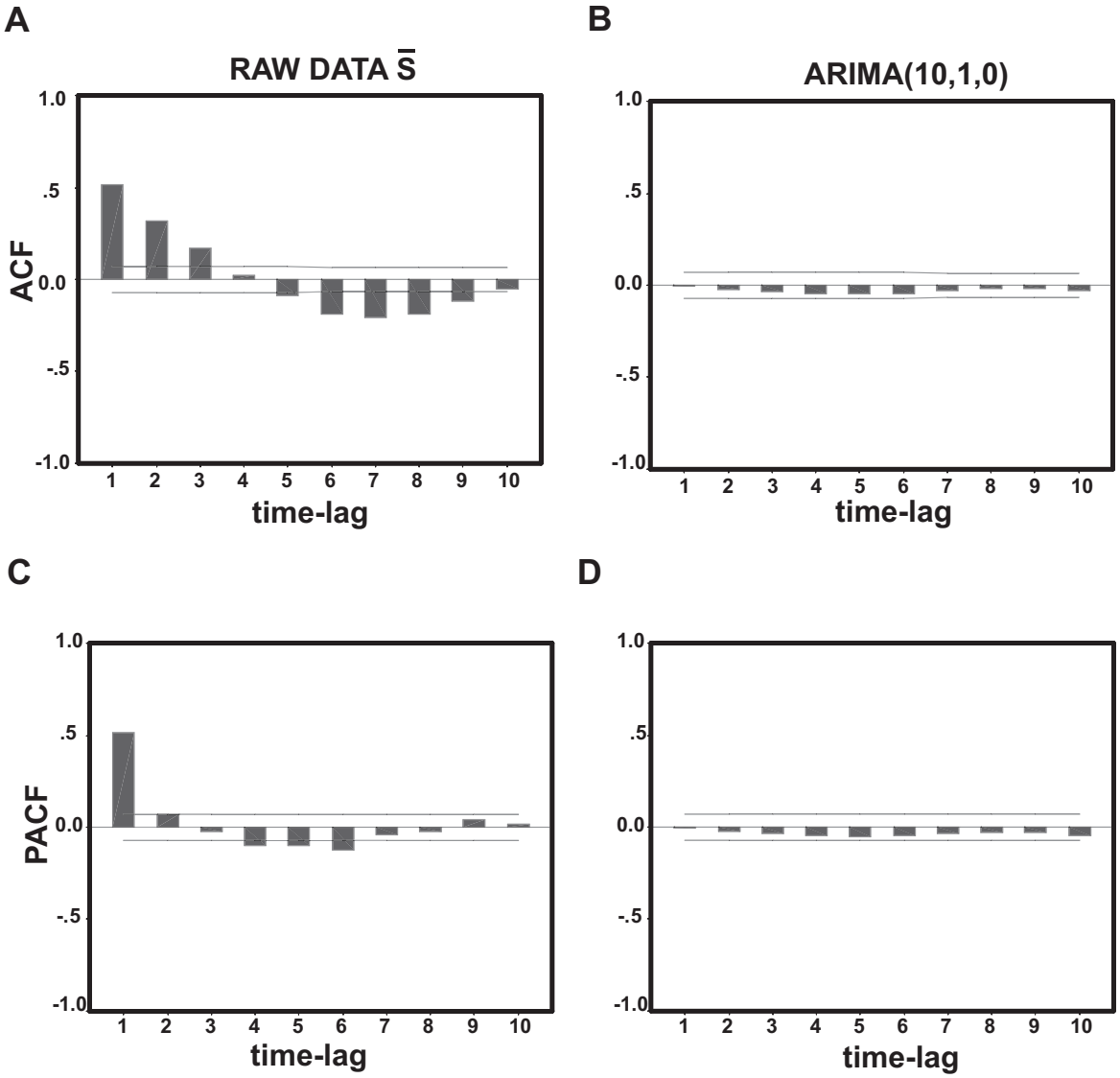

Figure 5.13: ACF structure of the log-transformed $\bar{S}$ before (**A**) and after (**B**) applying an ARIMA(10,1,0) model. PACF structure of the log-transformed $\bar{S}$ before (**C**) and after (**D**) applying the model. The black lines that are close to the reference zero-line, denote 95 % statistical significance level from the ACF and PACF value. Notice that the strong autocorrelation and partial-autocorrelation structure on the log-transformed $\bar{S}$ disappeared after applying ARIMA(10,1,0) modeling. That is, the ACFs and PACFs are flat.

averaging across subjects using Fisher's z-transformation, $z^{\bar{S}}_{i,j}(t)$. Similar to the cross-correlation analysis on the MEG time-series, we focused on the peak of cross-correlogram $z^{\bar{S}}_{i,j}(t^{'}_{max})$ and the corresponding $t^{'}_{max}$, the lag at which the peak occurred. We found that 84,948/306,280 (27.74 $\%$) $z^{\bar{S}}_{i,j}(t)$s had $p < 0.05$ and of those 42,754 (50.33 $\%$) were positive and 42,194 (49.67 $\%$) were negative. The average absolute value of $z^{\bar{S}}_{i,j}(t^{'}_{max})$s was 0.0826 $\pm 4.1176 \times 10^{-5}$ (mean $\pm$ SEM, $N = 84,948$). Additionally, the average positive and negative $z^{\bar{S}}_{i,j}(t^{'}_{max})$s were 0.0826 $\pm 5.7706 \times 10^{-5}$ ($N = 42,754$) and -0.0827 $\pm 5.8764 \times 10^{-5}$. The frequency distribution of the peak cross-correlations between the strength of neural interactions and the variability of movement direction across pairs of MEG sensors and subjects is illustrated in Fig. 5.14A.

Next, we focus on the time-lags $t^{'}_{max}$s, at which the peak cross-correlations $z^{\bar{S}}_{i,j}(t^{'}_{max})$s occurred. We found that 12,066 out of total 84,948 (14.21 $\%$) cross-correlograms had their peak at zero-lag, 36,719 (43.22 $\%$) at positive lag and 36,163 (42.57 $\%$) at negative lag. Note that zero-lag cross-correlation between neural interactions and variability of movement direction, indicates synchronous interactions between these time series of data. On the other hand, positive or negative lag corresponds to asynchronous interactions, in which one variable drives the other. Specifically, positive lag denotes that neural interactions precede changes in movement direction and vice-versa. In control theory context, positive and negative time-lags correspond to feedforward and feedback processes [64]. The frequency distribution of $t^{'}_{max}$s, which is presented in Fig. 5.14B, shows that $t^{'}_{max}$ is uniformly distributed between $\pm$ 3 lags. We interpret these results as evidence that neural interactions and variability of movement direction are integrated in a feedforward-feedback control scheme.

To look further on neural interactions that precede or follow changes in movement direction, we computed the number of positive and negative $t^{'}_{max}$s for any given pair of sensors (i, j) across the 10 subjects. Considering the 248 MEG sensors as a neural network that approximates the actual network of neuronal activity, we classified every pair of sensors in 2 MEG networks: 1) Positive Asynchronous network, if $t^{'}_{max}$ was positive for most subjects and 2) negative asynchronous network, if $t^{'}_{max}$ was negative for most subjects. Note that pairs of sensors with equal number of positive and negative $t^{'}_{max}$s across subjects were excluded from this analysis. We can visualize the spatial

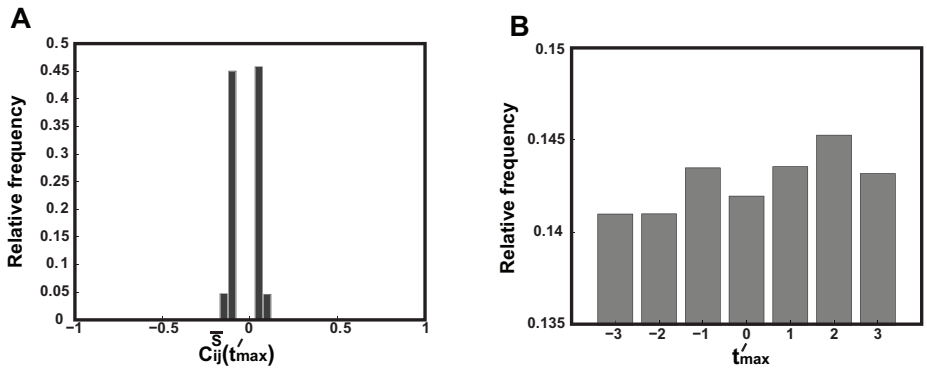

Figure 5.14: (**A**): Relative frequency distribution of the peak cross-correlations between the strength of neural interactions and the circular standard deviations. (**B**): Relative frequency distribution of $t^{'}_{max}$s, which corresponds to the time-lags that peak of cross-correlations occurred.

distribution of these two networks by connecting the MEG pairs of sensors with green (positive asynchronous) and red (negative asynchronous) lines. Fig. 5.15 shows a thresholded ($p < 0.0005$) view of these network. It can be seen that both networks are distributed around the whole MEG map and the interhemispheric interactions are very frequent.

Next, we focus the analysis on the individual 248 MEG sensors. That is, for any given sensor i, we computed how many pairs $(i, \star)$ ($\star$ corresponds to the other 247 MEG sensors) are part of the positive and negative asynchronous networks. Let's assume N_+ and N_-, the number of pairs of sensors $(i, \star)$ that have positive and negative $t^{'}_{max}$, respectively. If $N_+ - N_- > 0$, the sensor i was considered to be part of a network that is involved in feedforward processes. Otherwise, if $N_+ - N_- < 0$, the sensor i was considered to be part of network that is involved in feedback processes. Note that sensors, in which $N_+ - N_- = 0$, where excluded from this analysis. Fig. 5.16 illustrates the spatial frequency distribution of "feedforward" and "feedback" sensors as a color map, where blue indicates near zero (i.e., $N_+ - N_- \sim 0$) and red indicates high frequency regions (i.e., absolute value of $(N_+ - N_-)$ is very high). Similarly, Fig.5.17 shows the spatial frequency distribution of the feedforward and feedback sensors in a 3D space color map.

There are several interesting features in these networks, which follow: There is a strong focus of feedforward sensors in the left - contralateral to moving hand - frontal cortex and in the cerebellum. The frontal cortex is involved in organization, regulation, motor planning and motor execution. The

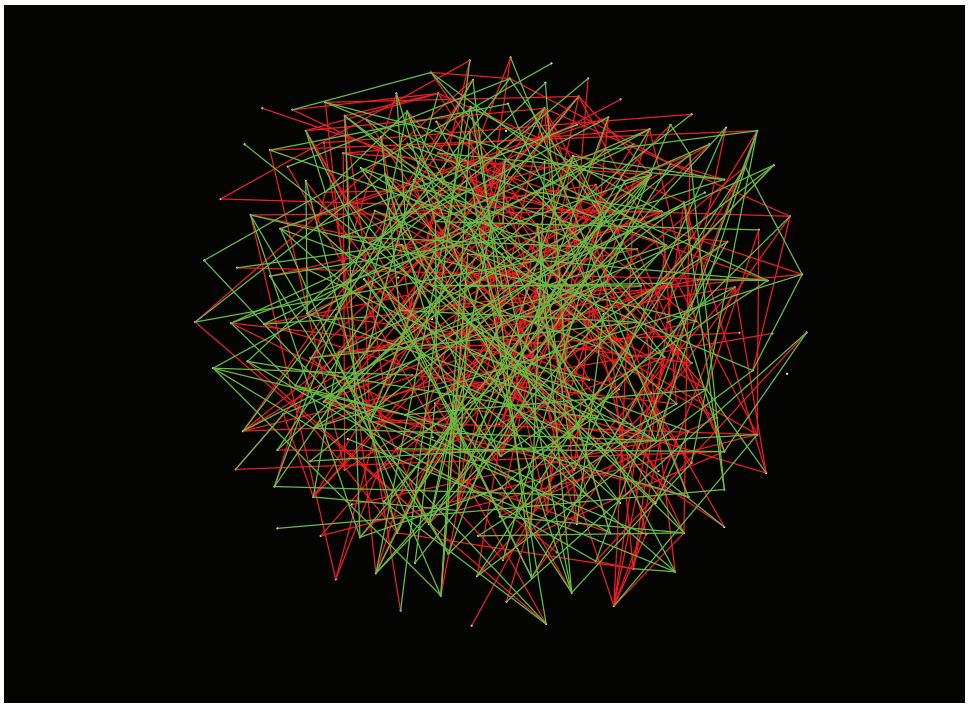

Figure 5.15: Massively interconnected networks that show the spatial distribution of MEG pairs of sensors, in which t'_{max} was either positive (green lines) for most subjects or negative (red lines) for most subjects. For visualization reasons, we present only these pairs of sensors with $p < 0.0005$.

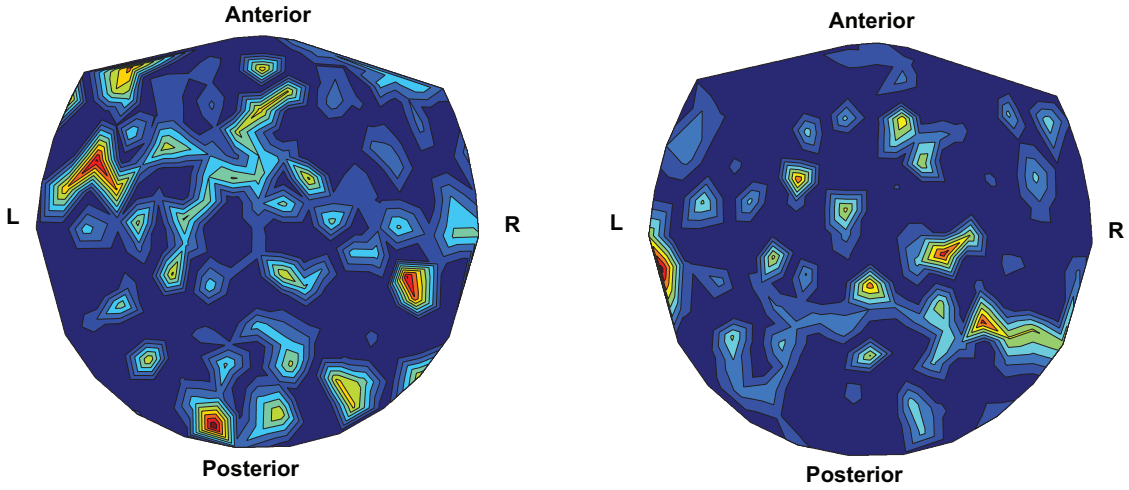

Figure 5.16: Spatial frequency distribution (2D) of the MEG sensors that are involved in (**Left**) feedforward and (**right**) feedback processes in continuous and sequential movements.

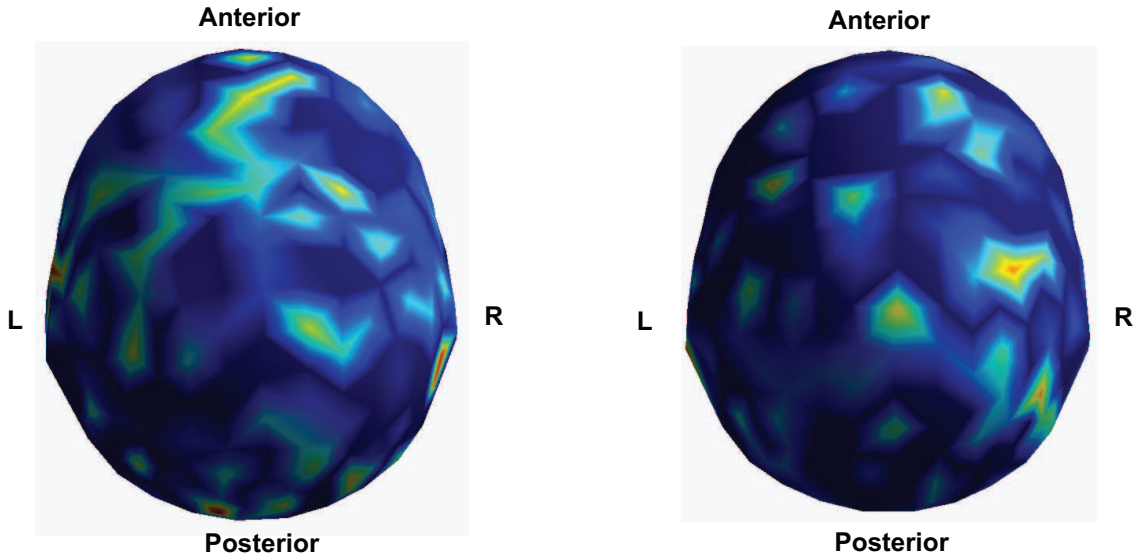

Figure 5.17: Similar to Fig. 5.16, but in a 3D space.

cerebellum is primarily a movement control center and although it does not initiate movements, it is involved in precision, coordination and prediction of movements. In addition, there is a strong focus of feedback sensors in the right parietal cortex and the left temporal cortex. Parietal cortex is involved in sensory integration and plays an important role in producing planned movements. The temporal cortex is highly associated with memory skills and sorting new information. We interpret these results as evidence that neural interactions among distinct brain regions implement the feedforward-feedback control scheme. Especially, frontal cortex and cerebellum are involved in feedforward processes, whereas right parietal cortex and left temporal cortex are related to feedback processes in continuous and sequential movements.

5.4.5 MEG cross-correlation analysis for time-bins with low and high circular standard deviation of movement direction

Next, we focus on exploring the neural interactions associated with trajectory segments with low and high variability of movement direction. We used the circular standard deviation $\bar{S}$ as a measure to assess the variability of movement direction within a given time interval. Particularly, low $\bar{S}$

corresponds to low variability of movement direction, which is associated with more straight movements (i.e., pentagon sides); high $\bar{S}$ corresponds to high variability of movement direction, which is associated with changes in movement direction (i.e., pentagon edges). An interesting question that we addressed in this study was how neural interactions are related to changes in movement direction. To examine this, we classified the time-bins into two groups: 1) time-bins with low $\bar{S}$ and 2) time-bins with high $\bar{S}$. The time-bins were classified after identifying the histogram mean of $\bar{S}$ for each subject. A time-bin was placed in the low variability category (group 1) if its $\bar{S}$ was less than 20% of the histogram mean; all others were put in the high variability of movement direction category (group 2) (see Methods section). The relative frequency distributions of the log-transformed $\bar{S}$ and *I* for both categories are presented in Fig. 5.18.

In the analysis that follows, we focus on the strength of the peak cross-correlation $z_{ij}(t_{max})$ and the corresponding lag t_{max}, in which the peak occurred. For time-bins that belong to group 1, we found that $35,491,190$ out of total $259,419,160$ (13.68 $\%$) $z_{ij}(t_{max})$s had a p-value less than 0.05, and of those $18,035,108/35,491,190$ (50.82$\%$) were positive and $17,456,082/35,491,190$ (49.18%) were negative. In high $\bar{S}$ category, we found $142,620,349$ out of total $259,419,160$ (54.98 $\%$) $z_{ij}(t_{max})$s with p-value less than 0.05, and of those, $72,493,540/142,620,349$ (50.83$\%$) were positive and $70,126,809/142,620,349$ (49.17%) were negative. Figs. 5.19A and 5.19B illustrate the relative frequency distributions of the peak cross-correlations across all pairs of sensors for time-bins that belong to group 1 and 2, respectively (only $z_{ij}(t_{max})$s with $p < 0.05$ are included in the distribution). We ran a two-sample Kolmogorov-Smirnov test and found that these distributions do not differ significantly ($p = 0.3860$). Figs. 5.19C and 5.19D show the relative frequency distributions of the time-lags t_{max}s, at which the peak cross-correlations occurred. It is clear that there is no any significant differences between these two distributions.

To look further on neural mechanisms associated with changes in movement direction, we explored whether there are pairs of sensors, whose interactions differ significantly between time-bins with low and high directional variability. To accomplish this, we averaged the peak of cross-correlations for any given pair of sensors (i, j) across time-bins that belong to group 1 (low directional variability) and group 2 (high directional variability) Next, we performed a t-test for each

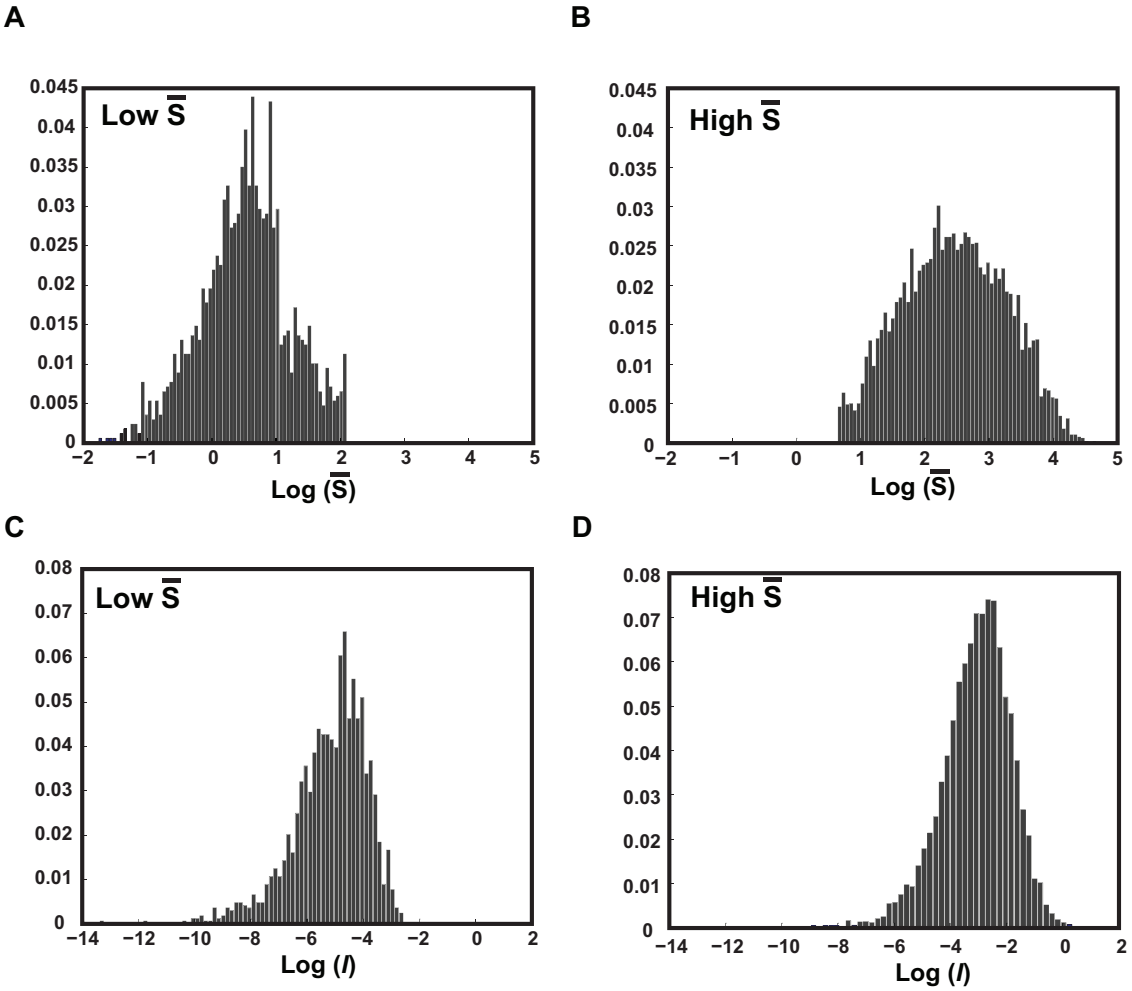

Figure 5.18: Relative frequency distribution of the log-transformed $\bar{S}$ for time-bins with (**A**) "low" $\bar{S}$ (1,694 time-bins) and (**B**) "high" $\bar{S}$ (6,776 time-bins) across all subjects. From the histogram of $\bar{S}$, we classified a time-bin into "low variability of movement direction" group, if its $\bar{S}$ was less than 20% the histogram mean. Otherwise, the time-bin was categorized in the "high variability of movement direction" group. The overlap between the two relative distributions in A and B is due to different histogram mean of $\bar{S}$s among subjects. The frequency distributions of the log-transformed *I* for group 1 and group 2 time-bins are presented in panel **C** and **D**, respectively.

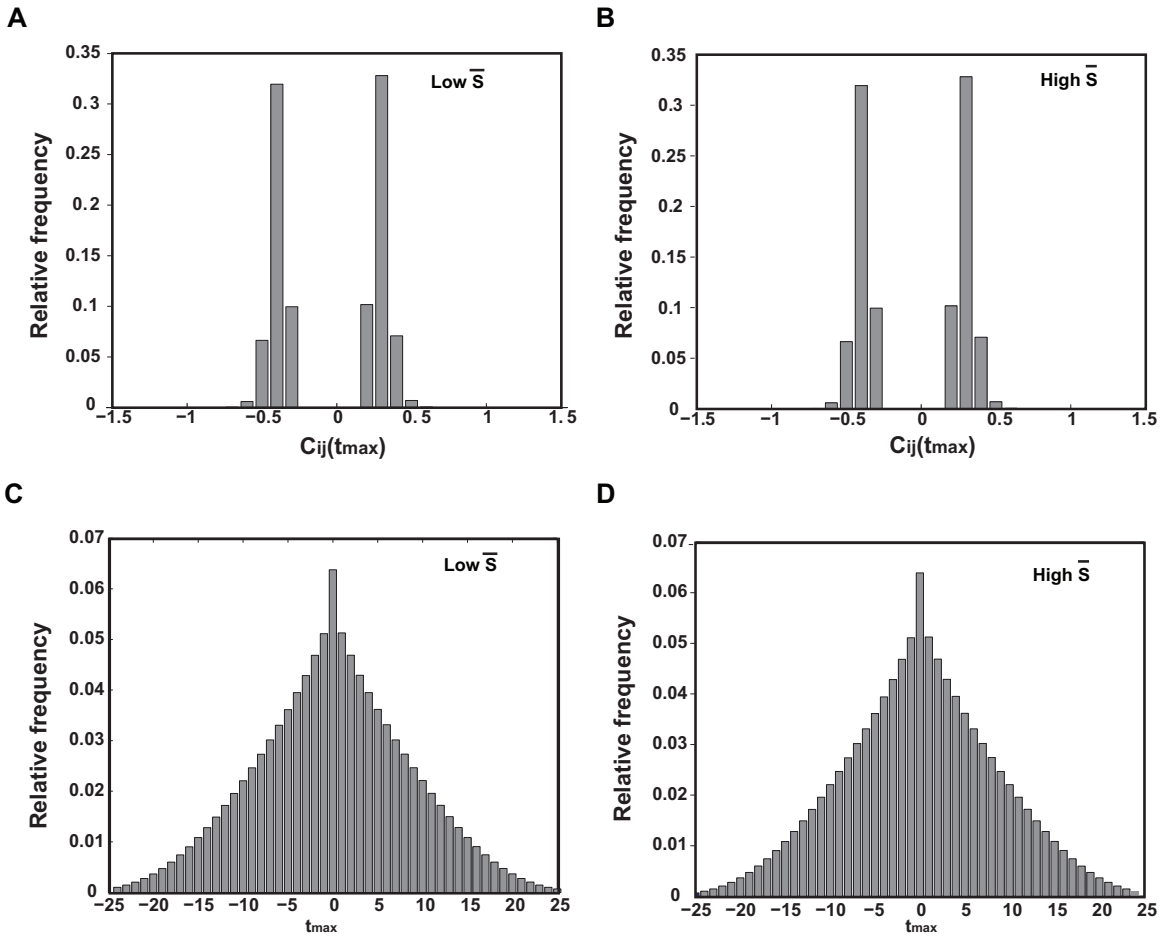

Figure 5.19: (**A**): Relative frequency distribution of the peak cross-correlations across time-bins with low $\bar{S}$. (**B**): Relative frequency distribution of the peak cross-correlations across time-bins with high $\bar{S}$. A two-sample Kolmogorov-Smirnov test showed that the difference between these two distributions is not statistically significant ($p = 0.3860$). (**C**): Relative frequency distribution of t_{max}s across time-bins with low $\bar{S}$ (**D**): Relative frequency distribution of t_{max}s across time-bins with high $\bar{S}$.

pair of sensor, to assess whether the average values of $z_{ij}(t_{max})$s of the two groups were statistically different from each other. Interestingly, we found 1,600 pairs of MEG sensors (5.22 $\%$), whose average value of $z_{ij}(t_{max})$ between the two groups differed significantly ($p < 0.05$). From those, 799 (49.93 $\%$) had stronger interactions in group 1 than group 2, and 801 (50.07 $\%$) had stronger interactions in group 2 than group 1. Fig. 5.20 illustrates a thresholded ($p < 0.005$) spatial distribution of these MEG pairs of sensors. Green and red lines denote stronger and weaker pair wise cross-correlations, respectively, in group 1 than group 2.

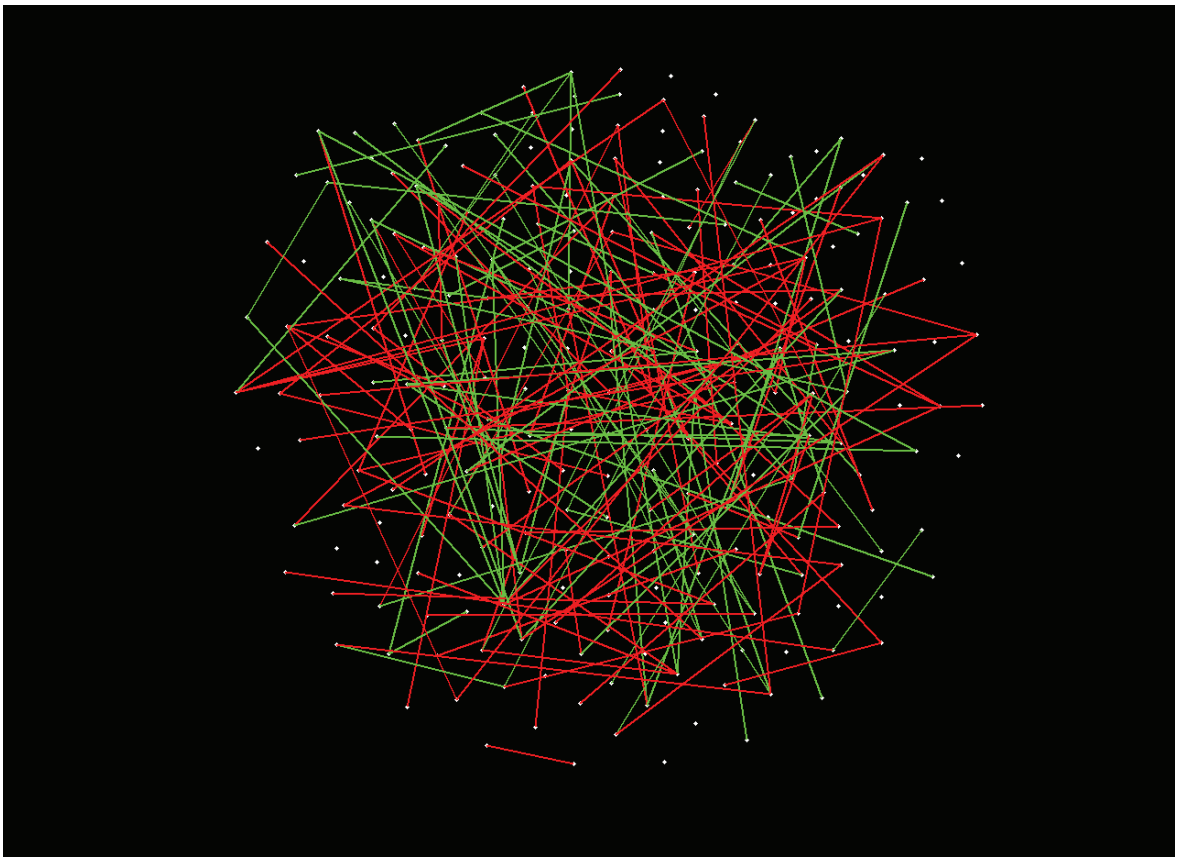

Figure 5.20: Massively interconnected network that illustrate the spatial distribution of MEG signals interactions that differ significantly between group 1 (low variability in movement direction) and group 2 (high variability in movement direction) ($p < 0.005$). The green lines denote pairs of sensors with stronger coupling in group 1 than group 2, and red lines denote pairs of sensors with stronger coupling in group 2 than group 1.

In the next analysis, we focus on the individual 248 MEG sensors. Particularly, for any given sensor i, we counted the M_{low} number of pairs $(i, \star)$ ($\star$ corresponds to the other 247 MEG sensors)

that had stronger coupling in group 1 than group 2 and the M_{high} number of pairs that had stronger coupling in group 2 than group 1 . If $M_{low} - M_{high} > 0$, the sensor i had stronger coupling with other sensors, for trajectory segments of group 1 (low directional variability) than group 2 (high directional variability) - called these sensors "low directional variability sensors". Similarly, if $M_{low} - M_{high} < 0$, the sensor i had stronger coupling with other sensors, for trajectory segments of group 2 than group 1 - called these sensors "high directional variability sensors". Sensors, in which $M_{low} - M_{high} = 0$ were excluded from further analysis. We can visualize the spatial frequency distribution of such sensors as a color map, where blue indicates near zero (i.e., $M_{low} - M_{high} \sim 0$) and red indicates high frequency regions (i.e., the absolute value of $M_{low} - M_{high}$ is very high). The 2D and 3D spatial frequency distributions of these two sensors are presented in Fig. 5.21 and 5.22 ($p < 0.05$).

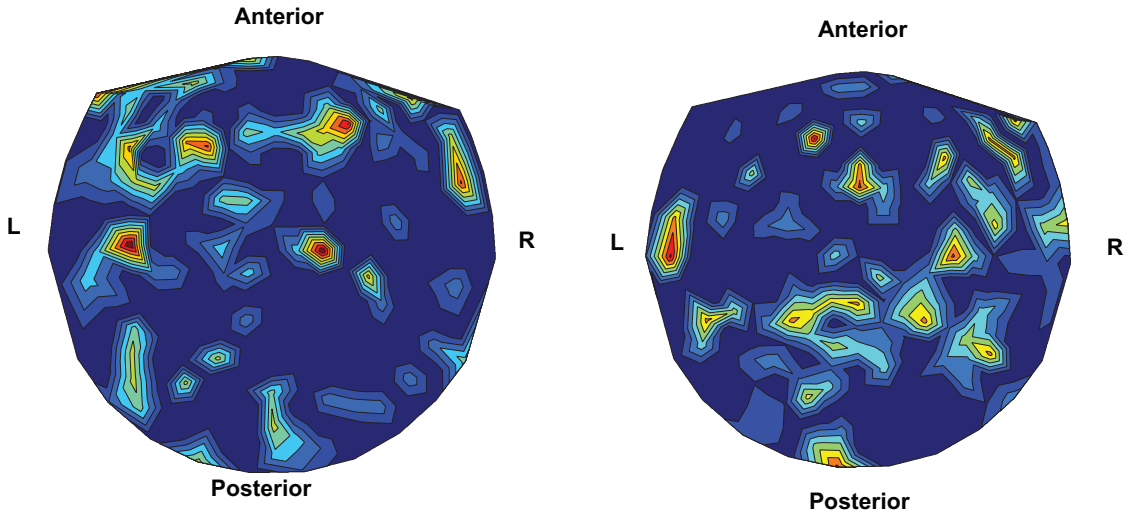

Figure 5.21: **Left**: Spatial frequency distribution (2D) of MEG sensors, which exhibit stronger interactions with other MEG sensors for trajectory segments that belong to group 1 (low directional variability of movement) than group 2 (high directional variability of movement). **Right**: Spatial frequency distribution (2D) of MEG sensors, which exhibit stronger interactions with other MEG sensors for trajectory segments that belong to group 2 than group 1.

The results show that "low directional variability sensors" are distributed around the frontal area of the brain. On the other hand, "high directional variability sensors" are more distributed along the right parietal area, the right frontal area and the cerebellum.

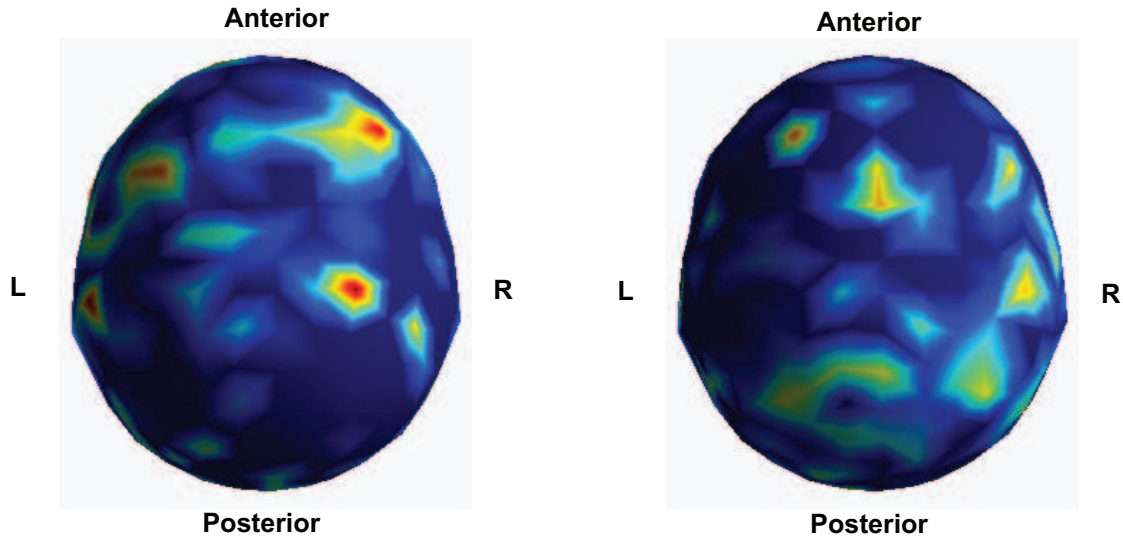

Figure 5.22: Similar to Fig. 5.21, but in a 3D space.

5.5 Discussion

We used Box-Jenkins [64, 66] time series analysis techniques to account for dynamic coupling between MEG stationary time-series and changes in movement direction, in a continuous sequential movement task (copying a pentagon). Most previous EEG and MEG studies, often related to Brain Computer Interface (BCI), have explored the association of neural activity with actual and imagined movements and found patterns of neural activity related to movements of different body extremities (e.g., left hand, right hand, tongue, foot) [19, 20, 61, 115, 157] or same extremity but different parts of it [82]. However, there are only a few MEG studies, which have investigated the association of neural activity with movement kinematics and suggest that MEG signals carry significant information related to movement position [15] and velocity [84]. But almost nose of these studies have explored the dynamic coupling between neural activity and movements in a spatiomotor task, with few exceptions such as [10]. Leuthold and his colleagues (2005) used Box-Jenkins time-series modeling to analyze MEG data acquired during three tasks (i.e., fixation on a central spot, fixation on a central spot surrounding by a pentagon and copying of the pentagon). They found a rich and consistent pattern of interactions between MEG sensors with respect to positive and negative pair wise cross-correlations. Interestingly, the overall prevalence of these patterns was preserved across the three tasks. However, this study did not address the question of how neural interactions are associated with behavioral parameters of the continuous and sequential movements used to copy the pentagon.

In the current study, we used the MEG data from the 3^{rd} task (copying the pentagon) of Leuthold study, in which 10 subjects were instructed to copy a pentagonal shape continuously, via an XY joystick, without visual feedback, while MEG data was collected using a 248-channel axial gradiometer system [10] (see Methods section). We tested the hypothesis that neural interactions carry information related to variability of movement direction. The first step in our analysis was to model the MEG time series using ARIMA modeling to derive stationary residuals (prewhitened data). Based on previous studies [10, 59], ARIMA(25,1,1) was adequate to produce quasi-stationary residuals with respect to mean, and autocorrelation. Subsequently, we divided the time-series in time-bins of 51 ms and computed the cross-correlation between time series in pairs of sensors $c_{ij}(t)$ (i.e., neural

interactions) over ± 25 time lags ($\sim$ 25 ms) in each time-bin. We normalized the distribution of the pair wise cross-correlations using Fisher's z-transformation, $z_{ij}(t)$. From this data, we computed the strength of peak of cross-correlation $z_{ij}(t_{max})$ and the corresponding time-lag t_{max} at which the peak occurred. In addition, we estimated the variability of movement direction during the 51 ms trajectory segment of each time-bin. To estimate that variability, we computed the instantaneous direction θ_t at any given time t of the trajectory segment and estimated the circular standard deviation of the movement direction $\bar{S}$.

To explore the relationship between neural interactions and variability of movement direction, we performed a cross-correlation analysis between $z_{ij}(t_{max})$s and the prewhitened circular standard deviations $\bar{S}$ss across all time-bins over $\pm$ 3 time-lags, including zero-lag. We characterized the obtained cross-correlograms, $z_{ij}^{\bar{S}}(t^{'})$, by determining the strength of the peak of cross-correlation $z_{ij}^{\bar{S}}(t_{max}^{'})$ and the time-lag $t_{max}^{'}$ at which the peak occurred. We found that the time-lag $t_{max}^{'}$ was almost uniformly distributed between time-lags -3 and 3. We can interpret this finding within the feedforward - feedback control scheme [64]. That is, neural interactions and variability of movement direction are integrated in a feedforward (positive $t_{max}^{'}$) - feedback (negative $t_{max}^{'}$) control scheme to plan, perform and correct movements.

Since the pioneering work of Woodworth (1899), there has been an ongoing debate on the contribution of feedforward and feedback processes to generate movements. Supporters of the feedforward view dominated the field early, arguing that the sensorimotor system does not use sensory feedback in reaching movements. Rather, a sequence of actions is defined in advance of movements, since humans are able to produce accurate movements in absence of visual feedback information [108]. The feedback processes have limited influence and only at the very end of the trajectories. Supporters of the feedback view responded to this claim by pointing out that vision is not the only source of sensory information, and accurate movements could be guided by proprioceptive feedback. To support this idea, they provided evidence that monkeys with deafferented limb were only able to produce erratic movements [12]. Next, supporters of the feedforward view fought back claiming that brain is not able to process information quickly enough to make use of sensory feedback in real-time [89]. Particularly, if the processing of sensory information is slower than the

hand motion in fast reaching movements, then the hand position will have changed by the time the sensory feedback is ready to influence it.

After a century of arguing against feedforward and feedback processes in volitional movements, it seems that the current view is somewhere between the two extreme views. Recent studies in non-human primates and patients with neurological disorders or brain damage suggest that distinct areas of the brain, such as the cerebellum, the primary and premotor motor cortices, the parietal cortex and the basal ganglia are involved in feedforward-feedback control processes to plan, perform and correct volitional movements [133, 141]. Particularly, cerebellum appears to be required for predicting sensory outcomes of actions and compensating for the consequences of ongoing motor commands [37, 133]. Additionally, studies in patients with damage in parietal cortex suggest that this brain area is involved in online error correction of movements. That is, patients with damage in parietal cortex could not adjust their hand movements in response to sudden changes in target locations [67, 117]. Ashe and Georgopoulos (1994) studied the time course of the ongoing cell activity in relation to evolving motor parameters, recorded in the arm area of motor cortex and in the arm area of posterior parietal cortex (area 5). They found that the timing of highest correlation (highest R^2) between firing rates and ongoing movement trajectories in motor cortex and the posterior parietal cortex was -90 ms and $+30$ ms, respectively [73].

Despite the significant knowledge that we have acquired from these studies, there is an information blackout on how feedforward and feedback processes are implemented on the brain. One of the novelties of our study is that we provide evidence that neural interactions are integrated with the variability of movement direction in a feedforward-feedback control scheme in continuous and sequential movements. We found that MEG sensors related to feedforward processes are distributed around the left frontal lobe and the cerebellum. On the other hand, MEG sensors related to feedback processes are more localized around the right parietal cortex and the left temporal cortex.

An interesting question that we addressed in this study was whether there are any differences in neural interactions between trajectories with low and high variability of movement direction. We used the circular standard deviation to categorize each time-bins into two categories, based on the histogram mean of $\bar{S}$: 1) "low variability of movement direction", if $\bar{S}$ was less than 20% of the

histogram mean and 2) "high variability of movement direction", if $\bar{S}$ was equal to or greater than 20% of the histogram mean. We found no significant differences on both peak of cross-correlations $z_{ij}(t_{max})$s and time-lags t_{max}s at which the peak occurred between the two categories of time-bins. These findings could indicate that either there is no difference in strength and time-lag of neural coupling associated with straight and curved movements or there is a subset of MEG sensors, whose interactions differ significantly between trajectories with low and high directional variability of movement. We explored this hypothesis by averaging the peak of the pair wise cross-correlations $z_{ij}(t_{max})$s for any given pair of sensors across group 1 (low directional variability) and group 2 (low directional variability) time-bins and performed a t-test to find pairs of sensors with significant differences on the average $z_{ij}(t_{max})$ between the two groups. Interestingly, we found pairs of sensors with stronger coupling in group 1 than group 2 and other pairs of sensors with stronger coupling in group 2 than group 1. Next, we focused on the individual 248 MEG sensors and looked for sensors that either exhibited stronger coupling with other sensors in group 1 than group 2 - named them "low directional variability sensors" - or exhibited stronger coupling with other sensors in group 2 than group 1 - named them "high directional variability sensors". We found that "low directional variability sensors" were more distributed around the frontal area of the brain, whereas "high directional variability sensors" were more distributed around the right parietal cortex, the right frontal area and the cerebellum.

Chapter 6

General Discussion

6.1 Summary

Recently, several research communities - such as neuroscience, psychology, and computer science - have recognized the importance of uncertainty in organizing human behavior. Despite many years of research, understanding how people anticipate and control sensory information to reduce uncertainty remains a challenging problem, mainly due to difficulty in making normative predictions. Additionally, little is known about how distinct cortical areas interact to plan and control movements. The primary goals of this thesis are to study aspects of human compensation strategy in purposive movement tasks, using grasping as a paradigm and to assess the spatiotemporal interactions of cortical areas associated with the planning and control of continuous and sequential movements.

We found that people compensate for object position uncertainty when making grasping movements by approaching the object along the direction of maximal position uncertainty and by opening their fingers wider to ensure their fingers don't collide with or miss the object. We interpret these results as evidence supporting the idea that the visuomotor system plans for uncertainty even in complex purposive movements. One of the novelties of this study is that we used normative predictions to evaluate the benefits of uncertainty compensation, adopting principles from statistical decision theory and using time efficiency as a natural cost function - people attempt to minimize overall the grasp time. We found that compensation strategies increase the chance to achieve a stable

grasp at first contact without requiring post-contact adjustments, and they decrease the probability of "inefficient movements" - movements that produce unstable grasp contacts.

To compute human achievable predictions, we modeled the grasping task within the optimal feedback control framework. Modeling the human hand as a 2D 1-link planar gripper and building a mix of task-dependent criteria that encode the minimum requirements needed to accomplish the task, we found that the optimal control framework was able to interpret many characteristics of human compensation strategies. In particular, the controller compensates for object position uncertainty by aligning the approach of the gripper with the orientation of the cylinder position distribution and by opening the fingers wider, only when the benefits in terms of making stable grasp outperform the control costs.

In addition, we studied the spatiotemporal neural interactions associated with planning and controlling continuous and sequential movements. For this study, we took data from an experiment, in which subjects had to copy a pentagonal shape continuously using an XY joystick, while neuromagnetic fluxes were recorded from their head using a whole-head MEG device. We found a rich and consistent pattern of neural interactions around the whole MEG map. One of the novelties of this study is that we found that neural interactions and variability of movement direction are integrated in a feedforward-feedback control scheme. In particular, we identified sparse sensors interactions that either precede (feedforward) or follow (feedback) changes of movement direction. We interpret these results as evidence that the perceptual-motor system acts as a feedforward-feedback control system to plan and control movements. Additionally, we identified MEG sensors, which are related to low directional variability trajectories (i.e., straight movements) and other sensors that are related to high directional variability trajectories (i.e., curved movements).

6.2 Broader impacts

The results of these studies will help to better understand how people gather information from the environment and manage uncertainty and how the perceptual-motor system plans and controls goal-directed movements. These results are important from the standpoint of both engineering innovation and the organization of the human brain. Such results will help illuminate how human

observers compensate for uncertainty in natural purposive tasks. They could also inspire engineers to improve robotic systems, such as humanoids and industrial robots used in manufacturing in a variety of tasks, such as welding, assembly, packaging and picking and placing items. Additionally, the extended optimal feedback control framework could be prove useful in opening new engineering applications, such as modern Brain Computer Interfaces (BCI) by building models that integrate forward predictions with sensory feedback provided to subjects through sensors to improve their estimate about the consequences of ongoing actions and to correct their movements. Finally, the proposed methodology on the MEG study could be extended to explore potential changes in neural connectivity due to mental illnesses, neurological disorders and brain damage.

References

[1] Bicchi A and Kumar V. An overview of dexterous manipulation. In *Proceedings of the IEEE International Conference on Robotics and Automation*, volume 1, pages 255–262, San Francisco, CA, Apr. 2000.

[2] Bicchi A and Kumar V. Robotic grasping and contact: a review. In *Proceedings of the IEEE International Conference on Robotics and Automation*, volume 1, pages 348–353, San Francisco, CA, Apr. 2000.

[3] Blake A. Computational modelling of hand-eye coordination. *Philosophical Transactions: biological Sciences*, 337(1281):351–360, 1992.

[4] Blake A and Isard M. *Active Contours*. Springer-Verlag, 1st edition, 1998.

[5] Mahajan A and Teneketzis D. *Foundations and Applications of Sensor Management*, chapter Multi-armed Bandit Problems, pages 121–303. Springer-Verlag, 2007.

[6] Morales A, Sanz PJ, and del Pobil AP. Vision-based computation of three-ginger grasps on unknown planar objects. In *Proceedings of the IEEE/RSJ International Conference on Intelligent Robots and System*, volume 2, pages 1711–1716, Washington, DC, May 2002.

[7] Schwartz AB, Kettner RE, and Georgopoulos AP. Primate motor cortex and free arm movements to visual targets in three-dimensional space. I. Relations between single cell discharge and direction of movement. *J. Neurosci.*, 8(8):2913–2927, 1988.

[8] Schwartz AB, Kettner RE, and Georgopoulos AP. Primate motor cortex and free arm movements to visual targets in three-dimensional space. II. Coding of the direction of movement by a neuronal population. *J. Neurosci.*, 8(8):2928–2937, 1988.

[9] Leuthold AC. Subtraction of heart artifact from MEG data: the matched filter revisited. In *Soc Neurosci Abstracts*, New Orleans, LA, Nov. 2003.

[10] Leuthold AC, Langheim FJ, Lewis SM, and Georgopoulos AP. Time series analysis of magnetoencephalographic data during copying. *Exp Brain Res.*, 164(4):411–422, 2005.

[11] Brouwer AM and Knill DC. The role of memory in visually guided reaching. *J Vis.*, 7(5):1–12, 2007.

[12] Lassek AM. Inactivation of voluntary motor function following rhizotomy. *J Neuropathol Exp Neurol.*, 12(1):83–87, 1953.

[13] Wing AM, Turton A, and Fraser C. Grasp size and accuracy of approach in reaching. *J Mot Behav.*, 18(3):245–260, 1986.

[14] Georgopoulos AP, Schwartz AB, and Kettner RE. Neuronal population coding of movement direction. *Science*, 233:1416–1419, 1986.

[15] Georgopoulos AP, Langheim FJ, Leuthold AC, and Merkle AN. Magnetoencephalographic signals predict movement trajectory in space. *Exp Brain Res.*, 167(1):132–135, 2005.

[16] Georgopoulos AP, Kalaska JF, Caminiti R, and Massey JT. On the relations between the direction of two-dimensional arm movements and cell discharge in primate motor cortex. *J. Neurosci.*, 2:1527–1537, 1982.

[17] Georgopoulos AP, Caminiti R, Kalaska JF, and Massey JT. Spatial coding of movement: a hypothesis concerning the coding of movement direction by motor cortical populations. *Exp. Brain Res. Suppl.*, 7:327–336, 1983.

[18] Gevins AS, Schaffer RE, Doyle JC, Cutillo BA, Tannehill RS, and Bressler S. Shadows of thought: shifting lateralization of human brain electrical patterns during brief visuomotor task. *Science*, 220(4592):97–99, 1983.

[19] Blankertz B, Dornhege G, Schafer C, Krepki R, Kohlmorgen J, Muller KR, Kunzmann V, Losch F, and Curio G. Boosting bit rates and error detection for the classification of fast-paced motor commands based on single-trial EEG analysis. *IEEE Trans Neural Syst Rehabil Eng.*, 11(2):127–131, 2003.

[20] Obermaier B, Neuper C, Guger C, and Pfurtscheller G. Information transfer rate in a five-classes Brain Computer Interface. *IEEE Trans Neural Syst Rehabil Eng.*, 9:283–288, 2001.

[21] Sivak B and MacKenzie CL. Integration of visual information and motor output in reaching and grasping: the contributions of peripheral and central vision. *Neuropsychologia*, 28(10):1095–1116, 1990.

[22] Averbeck BB, Crowe DA, Chafee MV, and Georgopoulos AP. Neural activity in prefrontal cortex during copying geometrical shapes. I. Single cells encode shape, sequence and metric parameters. *Exp Brain Res.*, 150(2):127–141, 2003.

[23] Averbeck BB, Crowe DA, Chafee MV, and Georgopoulos AP. Neural activity in prefrontal cortex during copying geometrical shapes. II. Decoding shape segments from neural ensembles. *Exp Brain Res.*, 150(2):142–153, 2003.

[24] Averbeck BB, Crowe DA, Chafee MV, and Georgopoulos AP. Differential contribution of superior parietal and dorsal-lateral prefrontal cortices in copying. *Cortex*, 45(3):432–441, 2009.

[25] Averbeck BB, Chafee MV, Crowe DA, and Georgopoulos AP. Parallel processing of serial movements. *Proc Natl Acad Sci U S A*, 99(20):13172–13177, 2002.

[26] Horn BKP. *Robot Vision*. MIT press, 1st edition, 1986.

[27] Atkeson C and Hollerbach J. Kinematic features of unrestrained vertical arm movements. *J Neurosci.*, 5:2318–2330, 1985.

[28] Gerloff C, Richard J, Hadley J, Schulman AE, Honda M, and Hallett M. Functional coupling and regional activation of human cortical motor areas during simple, internally paced and externally paced finger movements. *Brain*, 121:1513–1531, 1998.

[29] Buneo CA and Andersen RA. The posterior parietal cortex: sensorimotor interface for the planning and online control of visually guided movements. *Neuropsychologia*, 44(13):2594–2606, 2006.

[30] Rothkopf CA, Ballard DH, and Hayhoe MM. Task and context determine where you look. *J Vis.*, 7(14):1–20, 2007.

[31] Harris CM and Wolpert DM. Signal-dependent noise determines motor planning. *Nature*, 394(6695):780–784, 1998.

[32] Cheyne D and Weinberg H. Neuromagnetic fields accompanying unilateral finger movements: pre-movement and movement-evoked fields. *Exp Brain Res.*, 78(3):604–612, 1989.

[33] Cheyne D, Bakhtazad L, and Gaetz W. Spatiotemporal mapping of cortical activity accompanying voluntary movements using an event-related beamforming approach. *Hum Brain Mapp.*, 27(3):213–229, 2006.

[34] Liu D and Todorov E. Evidence for the flexible sensorimotor strategies predicted by optimal feedback control. *J Neurosci.*, 27(35):9354–9368, 2007.

[35] Moran D and Schwartz AB. Motor cortical representation of speed and direction during reaching. *J Neurophysiol.*, 82(5):2676–2692, 1999.

[36] Blackwell DA and Girshick MA. *Theory of Games and Statistical Decisions*. Wiley, 1954.

[37] Nowak DA, Timmann D, and Hermsdörfer J. Dexterity in cerebellar agenesis. *Neuropsychologia*, 45(4):696–703, 2007.

[38] Robinson DA. *Basic Mechanisms of Ocular Motility and Their Clinical Implications*, chapter Oculomotor Control Signals, pages 337–374. Oxford: Pergamon Press, 1975.

[39] Goldberg DE. *Genetic Algorithms in Search, Optimization, and Machine Learning*. Addison Wesley, 2007.

[40] Kirk DE. *Optimal Control Theory, An Introduction*. Prentice Hall, 1970.

[41] Jacobson DH and Mayne DQ. *Differential Dynamic Programming. Optimal Control.* Elsevier Publishing Company, New York, 1970.

[42] Wolpert DM, Ghahramani Z, and Flanagan JR. Perspectives and problems in motor learning. *Trends Cogn Sci.*, 5(11):487–494, 2001.

[43] Wolpert DM, Ghahramani Z, and Jordan MI. An internal model for sensorimotor integration. *Science*, 269(5232):1880–1882, 1995.

[44] Bertsekas DP. *Dynamic Programming and Optimal Control*, volume 1. Athena Scientific, 2nd edition, 2000.

[45] Bertsekas DP. *Dynamic Programming and Optimal Control*, volume 2. Athena Scientific, 2nd edition, 2000.

[46] Moran DW and Schwartz AB. Motor cortical activity during drawing movements: population representation during lemniscate tracing. *J Neurophysiol.*, 82(5):2705–2718, 1999.

[47] Moran DW and Schwartz AB. Motor cortical activity during drawing movements: population representation during spiral tracing. *J Neurophysiol.*, 82(5):2693–2704, 1999.

[48] Todorov E. *Studies of goal directed movements*. PhD thesis, Massachussetts Institute of Technology, Boston, Sept. 1998.

[49] Todorov E. Optimality principles in sensorimotor control. *Nat Neurosci.*, 7(9):907–915, 2004.

[50] Todorov E. Stochastic optimal control and estimation methods adapted to the noise characteristics of the sensorimotor system. *Neural Comput.*, 17:1084–1108, 2005.

[51] Todorov E and Jordan M. Optimal feedback control as a theory of motor coordination. *Nat Neurosci.*, 5(11):1226–1235, 2002.

[52] Todorov E and Jordan M. A minimal intervention principle for coordinated movement. In Becker et al, editor, *Advances in Neural Information Processing Systems*, volume 15, pages 27–34. MIT Press, 2003.

[53] Todorov E and Li W. A generalized iterative LQG method for locally-optimal feedback control of constrained nonlinear stochastic systems. In *Proceedings of the American Control Conference*, pages 300–306, 2005.

[54] Todorov E, Li W, and Pan X. From task parameters to motor synergies: a hierarchical framework for approximately-optimal control of redundant manipulators. *J Robot Syst.*, 22(11):691–710, 2005.

[55] Schlicht EJ and Schrater PR. Effects of visual uncertainty on grasping movements. *Exp Brain Res.*, 182(1):47–57, 2007.

[56] Anderson FC and Pandy MG. A dynamic optimization solution for vertical jumping in three dimensions. *Comput Methods Biomech Biomed Engin.*, 2(3):201–231, 1999.

[57] Anderson FC and Pandy MG. Dynamic optimization of human walking. *J Biomech Eng.*, 123(5):381–390, 2001.

[58] Andres FG, Mima T, Schulman AE, Dichgans J, Hallett M, and Gerloff C. Functional coupling of human cortical sensorimotor areas during bimanual skill acquisition. *Brain*, 122(855–870), 1999.

[59] Langheim FJ, Leuthold AC, and Georgopoulos AP. Synchronous dynamic brain networks revealed by magnetoencephalography. *Proc Natl Acad Sci U S A*, 103(2):455–459, 2006.

[60] Bebis G, Georgiopoulos M, Lobo NV, and Shah M. Learning affine transformations. *Pattern Recognition*, 32(10):1799–1999, 1999.

[61] Pfurtscheller G, Flotzinger D, and Kalcher J. Brain Computer Interface - a new communication device for handicapped persons. *Journal of Microcomputer Applications*, 16(3):293–299, 1993.

[62] Rotman G, Troje NF, and Johansson RS amd Flanagan JR. Eye movements when observing predictable and unpredictable actions. *J Neurophysiol.*, 96(3):1358–1369, 2006.

[63] Simmons G and Demiris Y. Object grasping using the minimum variance model. *Biological Cybernetics*, 94(5):393–407, 2006.

[64] Box GEP, Jenkins GM, and Reinsel GC. *Time series analysis: forecasting and control*. HoldenDay, 4th edition, 2008.

[65] Bone GM and Du Y. Multi-metric comparison of optimal 2d grasp planning algorithms. In *Proceedings of the IEEE International Conference on Robotics and Automation*, volume 3, pages 3061–3066, Seoul, Korea, May 2001.

[66] Jenkins GM and Watts DG. *Spectral Analysis and Its Applications*. HoldenDay, 1968.

[67] Gréa H, Pisella L, Rossetti Y, Desmurget M, Tilikete C, Grafton S, Prablanc C, and Vighetto A. A lesion of the posterior parietal cortex disrupts on-line adjustments during aiming movements. *Neuropsychologia*, 40(13):2471–2480, 2002.

[68] Mushiake H, Inase M, and Tanji J. Selective coding of motor sequence in the supplementary motor area of the monkey cerebral cortex. *Exp Brain Res.*, 82(1):208–210, 1990.

[69] Mushiake H and Strick PL. Pallidal neuron activity during sequential arm movements. *J Neurophysiol.*, 74(6):2754–2758, 1995.

[70] Tassinari H, Hudson TE, and Landy MS. Combining priors and noisy visual cues in a rapid pointing task. *J Neurosci.*, 26(40):10154–10163, 2006.

[71] Salimi I, Hollender I, Frazier W, and Gordon AM. Specificity of internal representations underlying grasping. *J Neurophysiol.*, 84(5):2390–2397, 2000.

[72] Stevenson IH, Fernandes HL, Vilares I, Wei K, and Körding KP. Bayesian integration and non-linear feedback control in a full-body motor task. *PLoS Comput Biol.*, 5(12), 2009.

[73] Ashe J and Georgopoulos AP. Movement parameters and neural activity in motor cortex and area 5. *Cereb Cortex.*, 4(6):590–600, 1994.

[74] Diedrichsen J, Shadmehr R, and Ivry RB. The coordination of movement: optimal feedback control and beyond. *Trends Cogn Sci.*, 14(1):31–39, 2010.

[75] Lukos J, Ansuini C, and Santello M. Choice of contact points during multidigit grasping: effect of predictability of object center of mass location. *J Neurosci.*, 27(14):3894–3903, 2007.

[76] Lukos J, Ansuini C, and Santello M. Anticipatory control of grasping: independence of sensorimotor memories for kinematics and kinetics. *J Neurosci.*, 28(48):12765–12774, 2008.

[77] Trommershäuser J, Maloney LT, and Landy MS. Statistical decision theory and the selection of rapid, goal-directed movements. *J Opt Soc Am A Opt Image Sci Vis.*, 20(7):1419–1433, 2003.

[78] Trommershäuser J, Maloney LT, and Landy MS. Statistical decision theory and trade-offs in the control of motor response. *Spat Vis.*, 16(3–4):255–275, 2003.

[79] Trommershäuser J, Maloney LT, and Landy MS. Decision making, movement planning and statistical decision theory. *Trends Cogn Sci.*, 12(8):291–297, 2008.

[80] Trommershäuser J, Maloney LT, and Landy MS. *Neuroeconomics*, chapter The Expected Utility of Movement, pages 95–111. New York: Academic Press, 2008.

[81] Trommershäuser J, Gepshtein S, Maloney LT, Landy MS, and Banks MS. Optimal compensation for changes in task-relevant movement variability. *J Neurosci.*, 25(31):7169–7178, 2005.

[82] Zhou J, Yao J, Deng J, and Dewaldbcd JPA. EEG-based classification for elbow versus shoulder torque intentions involving stroke subjects. *Comput Biol Med.*, 39(5):443–452, 2009.

[83] Coelho JA and Grupen RA. A control basis for learning multifingered grasps. *Journal of Robotic Systems*, 14(7):545–557, 1997.

[84] Kelso JA, Fuchs A, Lancaster R, Holroyd T, Cheyne D, and Weinberg H. Dynamic cortical activity in the human brain reveals motor equivalence. *Nature*, 392(6678):814–818, 1998.

[85] Saunders JA and Knill DC. Visual feedback control of hand movements. *J Neurosci.*, 24(13):3223–3234, 2004.

[86] Smeets JB and Brenner E. A new view on grasping. In *Motor Control*, volume 3, pages 237–271, 1999.

[87] Soechting JF, Buneo CA, Herrmann U, and Flanders M. Moving effortlessly in three dimensions: Does Donders' law apply to arm movement? *J Neurosci.*, 15(9):6271–6280, 1995.

[88] Soechting JF and Lacquaniti F. Invariant characteristics of a pointing movement in man. *J Neurosci.*, 1(7):710–720, 1981.

[89] Hollerbach JM. Computers, brains, and the control of movement. *Trends Neurosci.*, 5:189–192, 1982.

[90] Wolfe JM, Kluender KR, Levi DM, Bartoshuk LM, Herz RS, Klatzky RL, Lederman SJ, and Merfeld DM. *Sensation and Perception*. Sinauer Associates, Inc, 2009.

[91] Sanes JN, Dimitrov B, and Hallett M. Motor learning in patients with cerebellar dysfunction. *Brain*, 113:103–120, 1990.

[92] Kerr JR and Roth B. Analysis of multifingered hands. *International Journal of Robotics Research*, 4(4):3–17, 1986.

[93] Baizer JS, Kralj-Hans I, and Glickstein M. Cerebellar lesions and prism adaptation in macaque monkeys. *J Neurophysiol.*, 81(4):1960–1965, 1999.

[94] Aloimonos JY. Perspective approximations. *Image and Vision Computing*, 8(3):179–192, 1990.

[95] Toma K, Mima T, Matsuoka T, Gerloff C, Ohnishi T, Koshy B, Andres F, and Hallett M. Movement rate effect on activation and functional coupling of motor cortical areas. *J Neurophysiol.*, 88(6):3377–3385, 2002.

[96] O'Craven KM, Rosen BR, Kwong KK, Treisman A, and Savoy RL. Voluntary attention modulates fMRI activity in human MT-MST. *Neuron*, 18(4):591–598, 1997.

[97] Körding KP and Wolpert DM. Bayesian integration in sensorimotor learning. *Nature*, 427(6971):244–247, 2004.

[98] Körding KP and Wolpert DM. Bayesian decision theory in sensorimotor control. *Trends Cogn Sci.*, 10(7):319–326, 2006.

[99] Goldberg KY and Mason MT. Bayesian grasping. In *Proceedings of the IEEE International Conference on Robotics and Automation*, volume 2, pages 1264–1269, Cincinnati, OH, May 1990.

[100] Astolfi L, Cincotti F, Mattia D, Babiloni C, Carducci F, Basilisco A, Rossini PM, Salinari S, Ding L, Ni Y, He B, and Babiloni F. Assessing cortical functional connectivity by linear inverse estimation and directed transfer function: simulations and application to real data. *Clin Neurophysiol.*, 116(4):920–932, 2005.

[101] Laboratory for Engineering Man/ Machine Systems, Brown University. *2D planar database*.

[102] Brown LE, Halpert BA, and Goodale MA. Peripheral vision for perception and action. *Exp Brain Res.*, 165(1):97–106, 2005.

[103] Bear M, Connors B, and Paradiso M. *Neuroscience: exploring the Brain*. Williams and Wilkins, 1st edition, 1996.

[104] Biegstraaten M, Smeets JB, and Brenner E. The influence of obstacles on the speed of grasping. *Exp Brain Res.*, 149(4):530–534, 2003.

[105] Cutkosky M. On grasp choice, grasp models, and the design of hands for manufacturing tasks. In *Proceedings of the IEEE Transactions on Robotics and Automation*, volume 5, pages 269–279, Jun. 1989.

[106] Desmurget M, Epstein CM, Turner RS, Prablanc C, Alexander GE, and Grafton ST. Role of the posterior parietal cortex in updating reaching movements to a visual target. *Nat Neurosci.*, 2(6):563–567, 1999.

[107] Desmurget M and Grafton S. Forward modeling allows feedback control for fast reaching movements. *Trends Cogn Sci.*, 4(11):423–431, 2000.

[108] Desmurget M and Grafton ST. *Taking action: cognitive neuroscience perspectives on intentional acts*, chapter Feedback or Feedforward Control: End of a Dichotomy, pages 289–338. MIT Press, 2003.

[109] Dornay M, Uno Y, Kawato M, and Suzuki R. Minimum muscle-tension change trajectories predicted by using a 17-muscle model of the monkey's arm. *J Mot Behav.*, 28(2):83–100, 1996.

[110] Hämäläinen M, Hari R, Ilmoniemi RJ, Knuutila J, and Lounasmaa OV. Magnetoencephalographytheory, instrumentation, and applications to noninvasive studies of the working human brain. *Rev. Mod. Phys.*, 65:413–497, 1993.

[111] Kawato M. Internal models for motor control and trajectory planning. *Curr Opin Neurobiol.*, 9(6):718–727, 1999.

[112] Kawato M and Wolpert D. Internal models for motor control. *Novartis Found Symp.*, 218:291–304, 1998.

[113] Maschke M, Gomez CM, Ebner TJ, and Konczak J. Hereditary cerebellar ataxia progressively impairs force adaptation during goal-directed arm movements. *J Neurophysiol.*, 91(1):230–238, 2004.

[114] Mon-Williams M, Tresilian JR, Coppard VL, and Carson RG. The effect of obstacle position on reach-to-grasp movements. *Exp Brain Res.*, 137(3–4):497–501, 2001.

[115] Naeem M, Brunner C, Leeb R, Graimann B, and Pfurtscheller G. Seperability of four-class motor imagery data using independent components analysis. *J Neural Eng.*, 3(3):208–216, 2006.

[116] Weiner M, Hallett M, and Funkenstein HH. Adaptation to lateral displacement of vision in patients with lesions of the central nervous system. *Neurology*, 33:766–772, 1983.

[117] Rushworth MF, Johansen-Berg H, Göbel SM, and Devlin JT. The left parietal and premotor cortices: motor attention and selection. *Neuroimage.*, 20:S89–100, 2003.

[118] Pandy MG, Zajac FE, Sim E, and Levine WS. An optimal control model for maximum-height human jumping. *J Biomech.*, 23(12):1185–1198, 1990.

[119] Tana MG, Montin E, Cerutti S, and Bianchi AM. Exploring cortical attentional system by using fMRI during a continuous perfomance test. *Comput Intell Neurosci.*, 2010, 2010.

[120] Rearick MP and Santello M. Force synergies for multifingered grasping: effect of predictability in object center of mass and handedness. *Exp Brain Res.*, 144(1):38–49, 2002.

[121] Mason MT and Salisbury JK. *Robot hands and the mechanics of manipulation*. MIT press, May 1985.

[122] Lounasmaa OV, Hämäläinen M, Hari R, and Salmelin R. Information processing in the human brain: magnetoencephalographic approach. *Proc Natl Acad Sci U S A*, 93(17):8809–8815, 1996.

[123] Jenmalm P and Johansson RS. Visual and somatosensory information about object shape control manipulative fingertip forces. *J Neurosci.*, 17(11):4486–4499, 1997.

[124] Mazzoni P, Hristova A, and Krakauer JW. Why don't we move faster? Parkinson's disease, movement vigor, and implicit motivation. *J Neurosci.*, 27(27):7105–7116, 2007.

[125] Poupart P, Vlassis N, Hoey J, and Regan K. An analytic solution to discrete Bayesian reinforcement learning. In *Proceedings of the 23rd international conference on Machine learning*, pages 697–704, Pittsburgh, PA, Jun. 25–29 2006.

[126] Nunez PL. *Neocortical Dynamics and Human EEG Rhythms*. Oxford University Press, New York, 1995.

[127] Bays PM and Wolpert DM. Computational principles of sensorimotor control that minimize uncertainty and variability. *J Physiol.*, 578:387–396, 2007.

[128] Fitts PM. The information capacity of the human motor system in controlling the amplitude of movement. *J Exp Psychol Gen.*, 121(3):262–269, 1954.

[129] Sabes PN and Jordan MI. Obstacle avoidance and a perturbation sensitivity model for motor planning. *J Neurosci.*, 17(18):7119–7128, 1997.

[130] Battaglia PW and Schrater PR. Humans trade off viewing time and movement duration to improve visuomotor accuracy in a fast reaching task. *J Neurosci.*, 27(26):6984–6994, 2007.

[131] Schmidt R and Lee T. *Motor control and learning: a behavioral emphasis*. Human Kinetics, 4th edition, 2005.

[132] Shadmehr R. *Encyclopedia of Neuroscience*, volume 3, chapter Computational Approaches to Motor Control, pages 9–17. In: LR Squire, 2009.

[133] Shadmehr R and Krakauer JW. A computational neuroanatomy for motor control. *Exp Brain Res.*, 185(3):359–381, 2008.

[134] Shadmehr R and Krakauer JW. *The Cognitive Neurosciences*, chapter Computational Neuroanatomy of Voluntary Motor Control, pages 587–597. The MIT press, 2009.

[135] Wise RA. Addictive drugs and brain stimulation reward. *Annu Rev Neurosci.*, 19:319–340, 1996.

[136] Wise RA and Hoffman DC. Localization of drug reward mechanisms by intracranial injection. *Synapse*, 10(3):247–263, 1992.

[137] Wise RA, Spindler J, deWit H, and Gerberg GJ. Neuroleptic-induced "anhedonia" in rats: pimozide blocks reward quality of food. *Science*, 201(4352):262–264, 1978.

[138] Wise RA, Spindler J, and Legault L. Major attenuation of food reward with performance sparing doses of pimozide in the rat. *Can J Psychol.*, 32(2):77–85, 1978.

[139] Brost RC. Planning robot grasping motions in the presence of uncertainty. Technical Report CMU-RI-TR-85-12, The Robotic Institute, Carnegie-Mellon, Pittsburgh, PA, Jul. 1985.

[140] Gonzalez RC and Woods RE. *Digital Image Processing*. Pearson Education, 2nd edition, 2002.

[141] Seidler RD, Noll DC, and Thiers G. Feedforward and feedback processes in motor control. *Neuroimage.*, 22(4):1775–1783, 2004.

[142] Bellman RE. *Dynamic programming*. Princeton university press, 1957.

[143] Kettner RE, Schwartz AB, and Georgopoulos AP. Primate motor cortex and free arm movements to visual targets in three-dimensional space. III. Positional gradients and population coding of movement direction from various movement origins. *J Neurosci.*, 8(8):2938–2947, 1988.

[144] Cuijpers RH, Smeets JB, and Brenner E. On the relation between object shape and grasping kinematics. *J Neurophysiol.*, 91(6):2598–2606, 2004.

[145] Alexander RM. A minimum energy cost hypothesis for human arm trajectories. *Biol Cybern.*, 76(2):97–105, 1997.

[146] Johansson RS and Westling G. Roles of glabrous skin receptors and sensorimotor memory in automatic control of precision grip when lifting rougher or more slippery objects. *Exp Brain Res.*, 56(3):550–564, 1984.

[147] Johansson RS and Westling G. Coordinated isometric muscle commands adequately and erroneously programmed for the weight during lifting task with precision grip. *Exp Brain Res.*, 71(1):59–71, 1988.

[148] Dosen S and Popovic DB. *11th Mediterranean Conference on Medical and Biomedical Engineering and Computing 2007*, volume 16, chapter Optimal Control of Walking with Functional Electrical Stimulation: Inclusion of Physiological Constraints, pages 661–664. Springer Berlin Heidelberg, 2007.

[149] Gepshtein S, Seydell A, and Trommershäuser J. Optimality of human movement under natural variations of visual-motor uncertainty. *J Vis.*, 7(5):1–18, 2007.

[150] Ullman S and Basri R. Recognition by linear combinations of models. *IEEE Transactions on Pattern Analysis and Machine Intelligence*, 13(10):992–1006, 1991.

[151] Kim SG, Richter W, and Uğurbil K. Limitations of temporal resolution in functional MRI. *Magn Reson Med.*, 37(4):631–636, 1997.

[152] Scott SH. Optimal feedback control and the neural basis of volitional motor control. *Nat Neurosci.*, 5:534–546, 2004.

[153] Sober SJ and Sabes PN. Multisensory integration during motor planning. *J Neurosci.*, 23(18):6982–6992, 2003.

[154] Lewis SM, Jerde TA, Tzagarakis C, Georgopoulos MA, Tsekos N, Amirikian B, Kim S-G, Ugurbil K, and Georgopoulos AP. Cerebellar activation during copying geometrical shapes. *J Neurophysiol.*, 90:3874–3887, 2003.

[155] Venkataraman ST and Iberall T, editors. *Dextrous robot hands*. Springer-Verlag, 1990.

[156] Flash T and Hogan N. The coordination of arm movements: an experimentally confirmed mathematical model. *J Neurosci.*, 5(7):1688–1703, 1985.

[157] Geng T, Gan JQ, Dyson M, Tsui CSL, and Sepulveda F. A novel design of 4-class BCI using two binary classifiers and parallel mental tasks. *Comput Intell Neurosci.*, 2008, 2008.

[158] Ljungberg T, Apicella P, and Schultz W. Responses of monkey dopamine neurons during learning of behavioral reactions. *J Neurophysiol.*, 67(1):145–163, 1992.

[159] Poggio T and Bizzi E. Generalization in vision and motor control. *Nature*, 431(7010):768–774, 2004.

[160] Kimberley TJ and Lewis SM. Understanding neuroimaging. *Phys Ther.*, 87(6):670–683, 2007.

[161] Halsband U, Matsuzaka Y, and Tanji J. Neuronal activity in the primate supplementary, pre-supplementary and premotor cortex during externally and internally instructed sequential movements. *Neurosci Res.*, 20(2):149–155, 1994.

[162] Van Beers RJ, Sittig AC, and Gon JJ. Integration of proprioceptive and visual position-information: an experimentally supported model. *J Neurophysiol.*, 81(3):1355–1364, 1999.

[163] Van Beers RJ, Baraduc P, and Wolpert DM. Role of uncertainty in sensorimotor control. *Philos Trans R Soc Lond B Biol Sci.*, 357(1424):1137–1145, 2002.

[164] Van Mier H, Tempel LW, Perlmutter JS, Raichle ME, and Petersen SE. Changes in brain activity during motor learning measured with PET: effects of hand of performance and practice. *J Neurophysiol.*, 80(4):2177–2199, 1998.

[165] Nguyen VD. Constructing force-closure grasps. *The International Journal of Robotics Research*, 7(3):3–16, Jun. 1988.

[166] Gerdes VG and Happee R. The use of internal representation in fast gold-directed movements: a modeling approach. *Biol Cybern.*, 70(6):513–524, 1994.

[167] Christopoulos VN and Schrater PR. Handling shape and contact location uncertainty in grasping two-dimensional planar objects. In *IEEE/RSJ International Conference on Intelligent Robots and Systems*, pages 1557–1563, San Diegon, CA, Oct.29–Nov.2 2007.

[168] Christopoulos VN and Schrater PR. Grasping objects with environmentally induced position uncertainty. *PLoS Comput Biol.*, 5(10), 2009.

[169] Li W and Todorov E. Iterative linear-quadratic regulator design for nonlinear biological movement systems. In *Proceedings of the 1st International Conference on Informatics in Control, Automation and Robotics*, volume 1, pages 222–229, 2004.

[170] Nelson W. Physical principles for economies of skilled movements. *Biol Cybern.*, 46(2):135–147, 1983.

[171] Schultz W. Predictive reward signal of dopamine neurons. *J Neurophysiol.*, 80(1):1–27, 1998.

[172] Schultz W, Dayan P, and Montague PR. A neural substrate of prediction and reward. *Science*, 275(5306):1593–1599, 1997.

[173] Wu W, Gao Y, Bienenstock E, Donoghue JP, and Black MJ. Bayesian population decoding of motor cortical activity using a kalman filter. *Neural Comput.*, 18(1):80–118, 2006.

[174] Clower WT and Alexander GE. Movement sequence-related activity reflecting numerical order of components in supplementary and presupplementary motor areas. *J Neurophysiol.*, 80(3):1562–1566, 1998.

[175] Paulignan Y, Frak VG, Toni I, and Jeannerod M. Influence of object position and size on human prehension movements. *Exp Brain Res.*, 114(2):226–234, 1997.

[176] Uno Y, Kawato M, and Suzuki R. Formation and control of optimal trajectory in human multijoint arm movement. Minimum torque-change model. *Biol Cybern.*, 61(2):89–101, 1989.

[177] Zheng Y and Qian WH. Coping with the grasping uncertainties in force-closure analysis. *The International Journal of Robotics Research*, 24(4):311–327, Apr. 2004.

Appendix A

Bayesian decision theory for grasping objects with position uncertainty

In the methods section we outlined a Bayesian decision theoretic analysis of grasping under position uncertainty, which optimizes reach plans $\bar{S}$ over a function $R(C, S)$ that rewards trajectories with a high probability of achieving force-closure

$$\bar{s}^* = \arg\max_{\bar{s}} \left\{ G(\bar{s}) = \int_s \int_c R(c, s) P(c) p(s|\bar{s}) ds dc \right\} \tag{A.1}$$

In this section we show how to optimize the probability of force-closure for a trajectory $G(\bar{s})$ over reach plans. In particular, we prove that the approach that maximizes the probability of these contact conditions is aligned with the principal axis of the covariance of the cylinder distribution.

From the contact conditions described in the methods section, the contact indicator $R(C, S)$ has the form:

$$F = H\left(-\left(\mathbf{u}_{th}^{\perp}\right)^T \mathbf{u}_f^{\perp}\right) H\left(|w_f| - \epsilon\right) H\left(|w_{th}| - \epsilon\right) \delta\left(d_f - \rho\right) \delta\left(d_{th} - \rho\right) \tag{A.2}$$

Where H and δ denote Heaviside step function and the Delta Dirac, respectively.

To compute the probability that a trajectory will produce a force-closure grasp ($F = 1$), we need to compute the integral across C, which determines the fraction of possible cylinder locations that intersect the trajectory and satisfy the conditions above. Because the cylinder is in a cradle, the index finger and thumb can contact at different times and will not topple the cylinder. Thus, we can ignore the relative timing and focus on the spatial paths of the trajectories.

The integral $\int_c R(c,s)p(c)dc$ involves integrating a Gaussian distribution times a Dirac Delta over the contact coordinates that depend linearly on C, which results in another Gaussian distribution expressed in contact coordinates. It is easier to use the properties of Gaussian random variables under linear transformations to express this result. Thus we proceed by using the distribution of cylinder locations to induce a probability distribution on contact conditions. For convenience, we put the origin of trajectory space at the mean of the cylinder distribution. The density of cylinder locations is Gaussian with zero mean and covariance $\Sigma = V \begin{bmatrix} \sigma_{min}^2 & 0 \\ 0 & \sigma_{max}^2 \end{bmatrix} V^T$ where $V = \left[\mathbf{v}_m^{\perp} \mathbf{v}_m\right]$ is an orthonormal matrix composed of a unit vector $\mathbf{v}_m$ in the direction of maximal variance and its orthogonal complement. We assume that the maximal variance σ_{max}^2 is much larger than σ_{min}^2 making the covariance strongly oriented.

The integral $\int_c R(c,s)p(c)dc$ simplifies if we rewrite the contact coordinates of one finger in terms of the other. In particular $[w_{th}, d_{th}]$ is written in terms of $[w_f, d_f]$ as follows:

$$\begin{bmatrix} w_{th} \\ d_{th} \end{bmatrix} = \mathbf{U}_{th}^T \left(\mathbf{U}_f \begin{bmatrix} w_f \\ d_f \end{bmatrix} + \mathbf{r}_f - \mathbf{r}_{th} \right) \tag{A.3}$$

Because linear transformations of Gaussian random variables remain Gaussian, the distribution on cylinder locations $P(\vec{c}) = N(\vec{0}, \Sigma)$, induces a distribution on index finger contact coordinates, conditioned on index finger trajectory positions

$$P(w_f, d_f | \mathbf{r}_f) = N\left(-\mathbf{U}_f^T \mathbf{r}_f, \mathbf{U}_f \Sigma \mathbf{U}_f^T\right) \tag{A.4}$$

Given this induced distribution, it is relatively straightforward to compute the probability that the force-closure conditions hold. We must evaluate the cumulative probability that the contact conditions hold across a path $\{\mathbf{r}_f(t), \mathbf{r}_{th}(t)\}$. However, we need to compute the probability that $F = 1$ at $\{\mathbf{r}_f(t), \mathbf{r}_{th}(t)\}$, a single time point t in the trajectory:

$$P(F = 1|\mathbf{r}_f(t), \mathbf{r}_{th}(t)) = H\left(-\left(\mathbf{u}_{th}^{\perp}\right)^T \mathbf{u}_f^{\perp}\right) \int_{-\epsilon}^{\epsilon} P(w_f, d_f = \rho|\mathbf{r}_f(t)) P(w_{th}, d_{th} = \rho|\mathbf{r}_{th}(t), \mathbf{r}_f(t), w_f) dw_f \quad \text{(A.5)}$$

where $P(w_{th}, d_{th}|\mathbf{r}_{th}, \mathbf{r}_f, w_f) = \delta\left(\begin{bmatrix} w_{th} \\ d_{th} \end{bmatrix} - \mathbf{U}_{th}^T \left(\mathbf{U}_f \begin{bmatrix} w_f \\ d_f \end{bmatrix} + \mathbf{r}_f - \mathbf{r}_{th}\right)\right)$

The total probability of collision is the integral of $P(F = 1|\mathbf{r}_f(t), \mathbf{r}_{th}(t))$ over the trajectory. However, to compute the probability across a trajectory, we assume that if the index finger or thumb collides with the cylinder during the trajectory, it stops while the other finger continues on its same path. Although unrealistic for large movements, for our task the gap between the object and the non-contacting finger is never more than a few cm, making path changes due to propagation of the collision impulse through the hand less of an issue. This assumption allows us to decouple the trajectories of the index finger and the thumb and integrate them separately.

$$P(F = 1|S) = \int_{t_f} \int_{t_{th}} P\left(F = 1|\mathbf{r}_f(t_f)\mathbf{r}_{th}(t_t h)\right) dt_f dt_{th} \quad \text{(A.6)}$$

The trajectory that maximizes this expression is optimal in the sense that it has the best chance (on average) to achieve force-closure at contact. To maximize this expression, we take advantage of the following geometric argument. As the index finger and thumb sweep toward each other, they create an overlap area that represents the space of possible cylinders that can be intersected. The maximal overlap occurs when the finger contact surfaces are perpendicular to each other and the surface centroids move along a common path. Moreover, the best path is a straight line, because non-straight paths introduce spatial positions where the one finger might intersect a cylinder but

the other could miss it. In addition, when the fingers move toward each other along straight line path, any cylinder contacted will satisfy all the force-closure constraints. Thus, the problem reduces to find a straight line path that maximizes the integral above. We can parameterize the path as a straight line perpendicular to the contact surface $\mathbf{r} = \begin{bmatrix} 0 \\ \\ \tau \end{bmatrix}$. Here τ represents a path parameter that carries the finger through the origin of the space. The direction of this path through the cylinder distribution is determined by the finger surface normal since we define contact coordinates relative to the index finger/thumb orientation. Because along these paths the contact conditions are guaranteed to be satisfied, the probability of force-closure for a path reduces to a 2D integral over the cylinder distribution.

$$P\left(F=1|\mathbf{r}_f(t),\mathbf{r}_{th}(t)\right) = \int_{-T}^{T}\int_{-\epsilon}^{\epsilon} N\left(-\mathbf{U}_f^T \begin{bmatrix} 0 \\ \\ \tau \end{bmatrix}, \mathbf{U}_f V \begin{bmatrix} \sigma_{min}^2 & 0 \\ 0 & \sigma_{max}^2 \end{bmatrix} V^T \mathbf{U}_f^T\right) \quad \text{(A.7)}$$

where T is the maximum distance of the finger from the origin, and the integration is symmetric due to the exchangeability of index finger and thumb paths. Assuming that the maximum gripwidth $2T$ for the ideal agent is larger than the finger's contact surface width 2 , the integral is maximized when $\mathbf{U}_f = V^T$, which is when the longer integration region is parallel to the principle axis of the covariance matrix. Moreover, gripwidth should be made larger than fingerwidth - if biomechanically possible - because gripwidth is a controlled variable. In addition, the optimal strategy sets $p(S|\bar{S})$ equal to a Dirac Delta since any variability in path can only decrease this integral. In summary, the optimal strategy involves the index finger and thumb approaching the cylinder distribution center along a straight line path aligned with the principle axis of the cylinder distribution's covariance matrix.

Appendix B

Optimal control cost function for grasping objects with position uncertainty

In the method section of chapter 4, we outlined the cost function of the optimal feedback control framework for grasping a cylindrical object (see Eq. (4.8) of the main text). To model the effects of object position uncertainty in grasp plan, we take the expectation of this cost function with respect to the cylinder position distribution. In this section, we show analytically how to compute the expected values of the individual terms of the cost function.

The cost term f_1 is expressed mathematically as a sum of 3 Heaviside step functions H, whose values are zero once the cylinder is on the region defined by the fingers and the wrist. To simplify the calculations, we express the center of the cylinder position $\mathbf{p}^c = (x_c, y_c)$ with respect to the midpoint of the wrist, Eq. (B.1) and the base position of the stationary finger, Eq. (B.2) and the movable finger, Eq. (B.3).

$$\mathbf{C}_h = \mathbf{p}^c - \mathbf{p}^h \tag{B.1}$$

$$\mathbf{C}_{st} = \mathbf{C}_h + \frac{L_{st}}{2}\mathbf{u}_{st}^{\perp} \tag{B.2}$$

$$\mathbf{C}_{mv} \quad = \quad \mathbf{C}_h - \frac{L_{mv}}{2}\mathbf{u}_{st}^{\perp} \tag{B.3}$$

where L_{st} and L_{mv} are the length of the stationary and movable finger, respectively. Additionally, $\mathbf{u}_{st}^{\perp}$ is the direction perpendicular to the surface of the stationary finger. Note that the time dependence is suppressed inside the variables to make the notations less complex.

The expected f_1 with respect to the cylinder position distribution is given by Eq. (B.4).

$$E\Big\{ f_1 \Big\} = E\Big\{ H(\mathbf{C}_{mv}) + H(\mathbf{C}_{st}) + H(\mathbf{C}_h) \Big\} \tag{B.4}$$

We can define the mean and the variance of the cylinder position distribution with respect to the movable finger's frame of reference through Eq. (B.5). Additionally, the statistics of the cylinder position distribution on the stationary finger's and wrist's frame of reference are defined similarly, but with subscripts mv and h, respectively.

$$(\mu_{st}, \sigma_{st}) \quad = \quad \left[\mathbf{C}_{st}\mathbf{u}_{st}^{\perp}, \left(\mathbf{u}_{st}^{\perp}\right)^T \Sigma \mathbf{u}_{st}^{\perp} \right] \tag{B.5}$$

Based on these transformations, the expected value of $H(\mathbf{C}_{mv})$ with respect to the cylinder position distribution is given by Eq. (B.6).

$$g_{mv}(z) = \frac{1}{\sqrt{2\pi\sigma_{mv}}} \int_{-\infty}^{+\infty} H(z) e^{-\frac{1}{2}\frac{(z-\mu_{mv})^2}{\sigma_{mv}}} dz = \frac{1}{\sqrt{2\pi\sigma_{mv}}} \int_{-\infty}^{0} e^{-\frac{1}{2}\frac{(z-\mu_{mv})^2}{\sigma_{mv}}} dz \tag{B.6}$$

where z is the random variable of the cylinder position.

Notice that Eq. (B.6) is the cumulative Normal distribution function, which can be written in terms of the complimentary error function $erfc$ as follows:

$$g_{mv}(z) = e^{-\frac{\mu_{mv}^2}{2\sigma_{mv}}} - \sqrt{\frac{\pi}{2}}\,\mu_{mv}\,\sqrt{\sigma_{mv}}\,\mathrm{erfc}\left[\frac{\mu_{mv}}{\sqrt{2\sigma_{mv}}}\right] \tag{B.7}$$

Likewise, we compute the expected values of $H(\mathbf{C}_{st})$ and $H(\mathbf{C}_h)$. Hence, Eq. (B.4) is written as follows:

$$\begin{aligned} E\Big\{f_1\Big\} &= e^{-\frac{\mu_{mv}^2}{2\sigma_{mv}}} - \sqrt{\frac{\pi}{2}}\,\mu_{mv}\,\sqrt{\sigma_{mv}}\,\mathrm{erdf}\left[\frac{\mu_{mv}}{\sqrt{2}\sqrt{\sigma_{mv}}}\right] + e^{-\frac{\mu_{st}^2}{2\sigma_{st}}} - \sqrt{\frac{\pi}{2}}\,\mu_{st}\,\sqrt{\sigma_{st}}\,\mathrm{erdf}\left[\frac{\mu_{st}}{\sqrt{2}\sqrt{\sigma_{st}}}\right] \\ &+ e^{-\frac{\mu_h^2}{2\sigma_h}} - \sqrt{\frac{\pi}{2}}\,\mu_h\,\sqrt{\sigma_h}\,\mathrm{erdf}\left[\frac{\mu_h}{\sqrt{2}\sqrt{\sigma_h}}\right] \end{aligned} \tag{B.8}$$

The expected f_1 cannot be used directly to the LQG framework, because it is not quadratic with respect to the state variables. However, we are able to generate high quality approximations to the solution to this cost term using iterative quadratic approximation (see main text). To accomplish this, we approximate the expected value of f_1 with 2^{nd}-order Taylor series approximation around its minimum. We implemented an Evolutionary Algorithm (EA) to find the global minimum of the expected f_1 at each step of the reaching trajectory. We used 100 chromosomes in each generation consisting of 4 genes (i.e., the midpoint of the wrist (x_h, y_h), the orientation θ and the gripwidth gw). We applied both "crossover" and "mutation" operators with probability 0.8 and 0.2, respectively. Additionally, we used the "elitism" operator to ensure that the best chromosome of the population will survive to the next generation without being altered by the genetic operators. We found that 200 generations were adequate to converge to the optimal solution.

The cost term f_2 is expressed mathematically as the Euclidean distance between the midpoint of the wrist $\mathbf{p}^h$ and the center of the cylinder position $\mathbf{p}^c$. The expected value of f_2 with respect to the cylinder position distribution is given by Eq. (B.9).

$$E\Big\{ f_2 \Big\} = E\Big\{ \Big(||\mathbf{p}^h - \mathbf{p}^c||_2^2 - \delta^2 \Big)^2 \Big\} \tag{B.9}$$

where $\delta > 0$ corresponds to the desirable distance between the center of the cylinder and the position of the wrist at the end of the movement trajectory.

With few simple calculations, we can write Eq. (B.9) as follows:

$$\begin{aligned} E\Big\{ f_2 \Big\} &= x_h^4 + 4\left[-E(x_c)\right] x_h^3 + \left[6E(x_c^2) + 2E(y_c^2) - 2\delta^2\right] x_h^2 \\ &+ 4\left[-E(x_c^3) - E(x_c y_c^2) + \delta^2 E(x_c)\right] x_h + y_h^4 + 4\left[-E(y_c)\right] y_h^3 \\ &+ \left[6E(y_c^2) + 2E(x_c^2) - 2\delta^2\right] y_h^2 + 4\left[-E(y_c^3) - E(x_c^2 y_c) + \delta^2 E(y_c)\right] y_h \\ &+ 2x_h^2 y_h^2 + 4\left[-E(y_c)\right] x_h^2 y_h + 4\left[-E(x_c)\right] x_h y_h^2 + 8\left[E(x_c y_c)\right] x_h y_h \\ &+ \left[E(x_c^4) + E(y_c^4) + 2E(x_c^2 y_c^2) + \delta^4 - 2\delta^2 E(x_c^2) - 2\delta^2 E(y_c^2)\right] \end{aligned} \tag{B.10}$$

The expected f_2 is a 4^{th}-order polynomial and therefore cannot be used directly to the cost function of the LQG optimal control framework. Similar to the expected f_1, we construct a quadratic approximation of the expected f_2 at each step of the reaching trajectory (see main text for more details).

The expected f_3 and f_4 are quadratic functions with respect to the state variables and independent on the cylinder position. In addition, the expected value of the collision avoidance constraint term is given by Eq. (B.8) weighted by a scalar factor w_c. Finally, the expected value of the energy-like cost F_e is a quadratic function with respect to the controls and independent of the state variables and the position of the cylinder.

The expected cost function of the optimal control framework is given by summing the expected values of the individual terms described above.